DEVELOPMENT OF GLASS CATHODE MATERIALS FOR LI-ION BATTERIES USING LI-BORATE BASED GLASS MIXED WITH V_2O_5-Ni/Co VIA MELT QUENCHING METHOD

PUTTAMAWAN JUNTREE

A Thesis Submitted in Partial Fulfillment of the Requirements for the
Degree of Master in Applied Physics
Suranaree University of Technology
Academic Year 2024

การพัฒนาวัสดุแคโทดแก้วที่ใช้ลิเธียมบอเรตที่ผสมด้วย V_2O_5-Ni/Co สำหรับแบตเตอรีลิเธียมไอออนโดยวิธีหลอมเหลวทำให้เย็นตัวอย่างรวดเร็ว

นางสาวปัทมาวรรณ จันตรี

วิทยานิพนธ์นี้เป็นส่วนหนึ่งของการศึกษาตามหลักสูตรวิทยาศาสตรมหาบัณฑิต
สาขาวิชาฟิสิกส์ประยุกต์
มหาวิทยาลัยเทคโนโลยีสุรนารี
ปีการศึกษา 2567

DEVELOPMENT OF GLASS CATHODE MATERIALS FOR LI-ION BATTERIES USING LI-BORATE BASED GLASS MIXED WITH V_2O_5-Ni/Co VIA MELT QUENCHING METHOD

Suranaree University of Technology has approved this thesis submitted in partial fulfillment of the requirements for the Degree of Master in Applied Physics.

Thesis Examining Committee

(Assoc. Prof. Dr. Panomsak Meemon)
Chairperson

(Assoc. Prof. Dr. Prayoon Songsiriritthigul)
Member (Thesis Advisor)

(Dr. Pinit Kidkhunthod)
Member (Thesis Co-Advisor)

(Assoc. Prof. Dr. Prapun Manyum)
Member

(Dr. Wiwat Nuansing)
Member

(Assoc. Prof. Dr. Yupaporn Ruksakulpiwat)
Vice Rector for Academic Affairs
and Quality Assurance

(Prof. Dr. Santi Maensiri)
Dean of Institute of Science

ปัทมาวรรณ จันตรี : การพัฒนาวัสดุแคโทดแก้วที่ใช้ลิเธียมบอเรตที่ผสมด้วย V_2O_5-Ni/Co สำหรับแบตเตอรีลิเธียมไอออนโดยวิธีหลอมเหลวทำให้เย็นตัวอย่างรวดเร็ว (DEVELOPMENT OF GLASS CATHODE MATERIALS FOR LI-ION BATTERIES USING LI-BORATE BASED GLASS MIXED WITH V_2O_5-Ni/Co VIA MELT QUENCHING METHOD) อาจารย์ที่ปรึกษา : รองศาสตราจารย์ ดร.ประยูร ส่งสิริฤทธิกุล, 121 หน้า.

คำสำคัญ : แบตเตอรีลิเธียมไอออน (LIB_5), แบตเตอรีแก้ว, วาเนเดียมเพนทอกไซด์ (V_2O_5), ลิเธียมเฮกซะบอเรต ($Li_6B_4O_9$), คุณสมบัติทางเคมีไฟฟ้า, การดูดกลืนรังสีเอกซ์สเปกโทรสโกปี (XAS), In-situ X-ray Absorption Spectroscopy (In-situ XAS)

วิทยานิพนธ์นี้มุ่งเน้นการพัฒนาส่วนประกอบแก้วลิเธียมบอเรตเพื่อเพิ่มประสิทธิภาพของวัสดุแคโทดในแบตเตอรีลิเธียมไอออน โดยมีการเตรียมส่วนผสมที่มีอัตราส่วนนิกเกิลต่อโคบอลต์ (Ni-Co) 4:1 รวมถึงแคโทดแก้วที่มีโคบอลต์สูงในอัตราส่วน (Ni-Co) 1:1 จากนั้นมีการผสมวาเนเดียมเพนทอกไซด์ (V_2O_5) เพื่อเพิ่มความจุ การศึกษานี้ใช้แก้วที่มีส่วนประกอบเป็นลิเธียมบอเรต (LBO) เพื่อเพิ่มความเสถียร กระบวนการหลอมแก้วแบบง่ายถูกพัฒนาขึ้นเพื่อให้ได้ค่าความจุจำเพาะที่สูงสุด การทดลองประกอบด้วย 4 กระบวนการที่แตกต่างกัน ในกระบวนการแรกใช้ Ni-Co และ LBO จากนั้นจึงใช้วิธีการหลอมแก้วโดยการทำให้เย็นอย่างรวดเร็ว กระบวนการที่สองเริ่มด้วยการผสมผลิตภัณฑ์จากกระบวนการแรกกับ V_2O_5 ก่อนเข้าสู่การหลอมแก้วแบบเย็นเช่นเดียวกัน ในกระบวนการที่สาม LBO, NiO, Co_3O_4, และ V_2O_5 ถูกผสมรวมกันแล้วหลอมพร้อมกันโดยใช้วิธีการหลอมแก้วแบบเย็นตัวลงอย่างรวดเร็ว ส่วนในกระบวนการสุดท้ายเป็นการผสมแก้วจากกระบวนการแรกกับ V_2O_5 และกวนผสมต่อเนื่องเป็นเวลา 24 ชั่วโมงเพื่อทำให้กระบวนการเสร็จสมบูรณ์ ผลการวิเคราะห์ด้วยเทคนิคการเลี้ยวเบนรังสีเอกซ์ (XRD) เผยให้เห็นโครงสร้างของเซรามิกแก้วลิเธียมเฮกซาบอเรต ($Li_6B_4O_9$) ซึ่งบ่งบอกถึงการเปลี่ยนแปลงไปสู่โครงสร้างเซรามิกการทดสอบสมรรถนะของแบตเตอรีประกอบด้วยการวิเคราะห์การชาร์จ-คายประจุ, ไซคลิกโวลแทมเมทรี (CV), การวิเคราะห์ความต้านทานทางไฟฟ้าเคมี (EIS), และการวิเคราะห์การดูดกลืนรังสีเอกซ์ (XAS) ซึ่งครอบคลุมทั้งโครงสร้างใกล้ขอบการดูดกลืนรังสีเอกซ์ (XANES) และโครงสร้างละเอียดของการดูดกลืนรังสีเอกซ์ (EXAFS) พร้อมทั้งการวิเคราะห์ XAS แบบ in-situ ผลการทดลองชี้ให้เห็นว่าตัวอย่างที่มีการผสม V_2O_5 มีความจุและความเสถียรเพิ่มขึ้น ตัวอย่างที่มีประสิทธิภาพดีที่สุด $[NCV]_m$ แสดงค่าความจุจำเพาะที่ 111.42 mAh/g และ

ความหนาแน่นพลังงานที่ 306.26 mWh/g อีกทั้งยังมีความเสถียรในการใช้งานซ้ำที่ยอดเยี่ยม โดยสามารถคงค่าความจุเริ่มต้นไว้ได้ถึง 80.69% ตลอดการใช้งาน 100 รอบ

สาขาวิชาฟิสิกส์
ปีการศึกษา 2567

ลายมือชื่อนักศึกษา ปัทมาวรรณ จันตรี
ลายมือชื่ออาจารย์ที่ปรึกษา
ลายมือชื่ออาจารย์ที่ปรึกษาร่วม

PUTTAMAWAN JUNTREE : DEVELOPMENT OF GLASS CATHODE MATERIALS FOR LI-ION BATTERIES USING LI-BORATE BASED GLASS MIXED WITH V_2O_5-Ni/Co VIA MELT QUENCHING METHOD. THESIS ADVISOR : ASSOC. PROF. PRAYOON SONGSIRIRITTHIGUL, PhD. 121 PP.

Keyword: Lithium-ion batteries (LIBs), Glass electrode, Vanadium pentoxide (V_2O_5), Lithium Hexaborate ($Li_6B_4O_9$), Electrochemical properties, X-ray absorption spectroscopy (XAS), In-situ X-ray absorption spectroscopy (In-situ XAS).

This thesis focuses on the development of lithium borate glass components to enhance the performance of cathode materials in lithium-ion batteries. It involves preparing mixtures with a 4:1 nickel-to-cobalt (Ni-Co) ratio, as well as cobalt-rich glass cathodes with a 1:1 Ni-Co ratio. Subsequently, vanadium pentoxide (V_2O_5) is incorporated to further improve capacity. The study employs Li-borate-based glass (LBO) for enhanced stability. A simplified glass melting process is developed to achieve the highest specific capacity. The experiment involves four distinct processes. In the initial process, Ni-Co and LBO are mixed to form a homogeneous mixture, which is then subjected to the glass melt quenching method. The second process commenced by mixing the products of the first process with V_2O_5 before proceeding again to the glass melt quenching method. In the third process, LBO, NiO, Co_3O_4, and V_2O_5 were all combined and then simultaneously subjected to the glass melt quenching method. The final process involved mixing glass from the first process with V_2O_5 for 24 hours to complete the procedure. X-ray diffraction revealed the formation of a lithium hexaborate glass-ceramic structure of $Li_6B_4O_9$, suggesting a glass-ceramic transition. The performance testing of the battery included a charge-discharge analysis, cyclic voltammetry (CV), electrochemical impedance spectroscopy (EIS), and X-ray absorption spectroscopy (XAS), which encompasses both X-ray Absorption Near Edge Structure (XANES) and Extended X-ray Absorption Fine Structure (EXAFS), along with

an in-situ XAS analysis. The results indicated that the V_2O_5-mixed samples showed increased capacity and stability. The best-performing sample, $[NCV]_m$, exhibited a specific capacity of 111.42 mAh/g, energy density of 306.26 mWh/g, and demonstrated excellent cycling stability, maintaining an impressive 80.69% of its initial capacity over 100 cycles.

School of Physics
Academic Year 2024

Student's signature ปัทมาวรรณ จันทรี
Advisor's signature
Co-advisor's signature

ACKNOWLEDGEMENT

The successful completion of this thesis would not have been possible without the invaluable support and assistance of many individuals, to whom I extend my deepest gratitude for their unwavering commitment and encouragement.

I would like to express my gratitude to Assoc. Prof. Dr. Prayoon Songsiriritthigul for serving as my thesis adviser during my PhD study and research. I am deeply grateful for the unwavering support provided throughout my academic journey. I appreciate the insightful talks and the valuable knowledge shared, particularly in terms of guiding my research efforts towards presenting the research findings with the utmost clarity. I am deeply grateful and privileged to have the opportunity to work and study under your esteemed leadership. I express my appreciation to my co-advisor, Dr. Pinit Kidkhunthod, for continually providing me with possibilities for novel collaborations that have yielded exceptional achievements. Whenever I encountered a state of perplexity, he provided guidance in the form of a robust strategy aimed at identifying a single solution to address the situation at hand. I express my gratitude to Assoc. Prof. Dr. Panomsak Meemon, Assoc. Prof. Dr. Prapun Manyum and Dr. Wiwat Nuansing for their perceptive inquiries and constructive feedback on my thesis.

I would like to extend my sincere gratitude to the staff members of the Novel Glass Laboratory, including Dr. Jintara Padchasri, Sumeth Siriroj, and Mr. Amorntep, for their invaluable guidance and instruction throughout the manufacturing process of lithium borate ($LiBO_3$ or LBO) using the Melt-Quenching Technique. Their support and insights were instrumental during challenging moments, offering clarity and aiding in the exploration of effective solutions. Additionally, their assistance was greatly appreciated in the manuscript revision process.

I wish to extend my heartfelt gratitude to the entire faculty and staff of the School of Physics for their instrumental role in supporting my academic development. Their instructive lectures, comprehensive resources, and thoughtful discussions in seminars have significantly deepened my understanding of the subject.

I am equally grateful to my peers at the Institute of Science for their unwavering companionship and collaboration. Finally, I offer my deepest appreciation to my parents, whose constant support has been invaluable to both my personal and academic growth.

Puttamawan Juntree

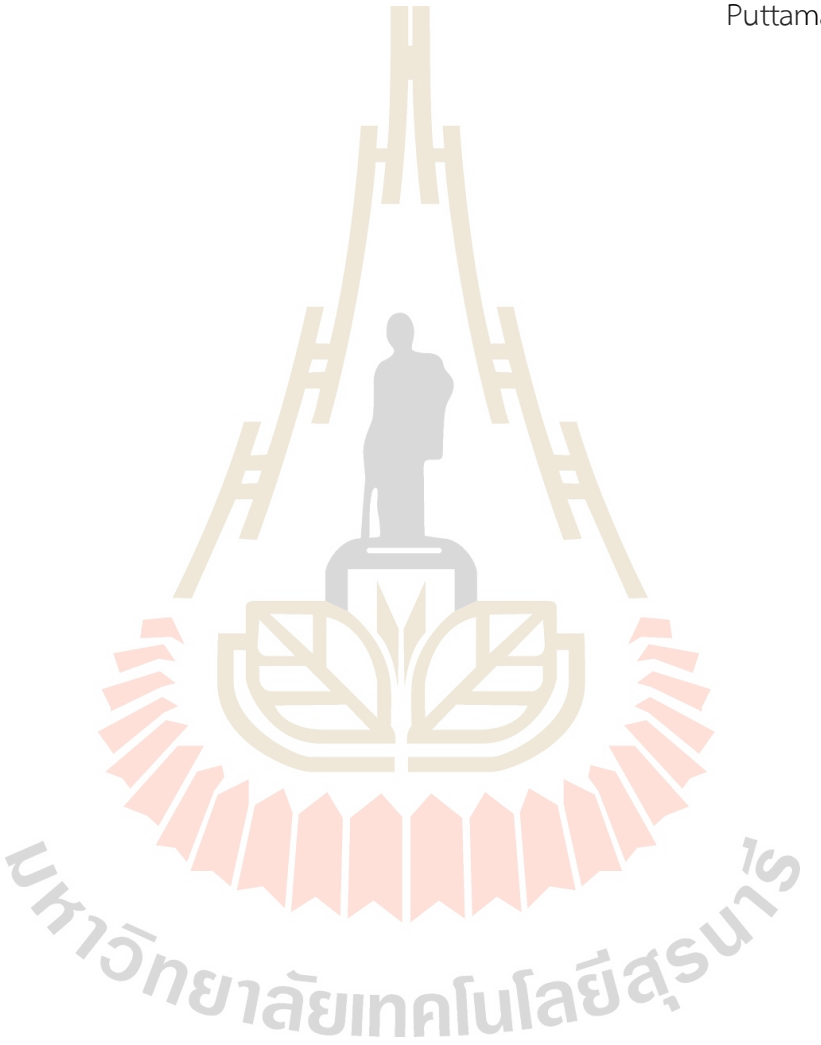

CONTENTS

CONTENTS (Continued)

CONTENTS (Continued)

CONTENTS (Continued)

LIST OF FIGURES

LIST OF FIGURES (Continued)

LIST OF FIGURES (Continued)

LIST OF FIGURES (Continued)

LIST OF FIGURES (Continued)

LIST OF ABBREVIATIONS

LIBs	Lithium-ion batteries
EVs	Electric vehicles
Li-ion	Lithium-ion
$LiFePO_4$	Lithium iron phosphate
$LiMBO_3$	Lithium-metal borate
NMC	Lithium nickel manganese cobalt oxide
Li_2O	Lithium oxide
B_2O_3	Boron trioxide
ESD	Energy Storage Devices
EES	Electrochemical Energy Storage
ESS	Energy Storage Systems
FCs	Fuel Cells
LBO	Lithium-borate-based Glass
V_2O_5	Vanadium Pentoxide
Ni-Co	Nickel-Cobalt
Na-ion	Sodium-ion Batteries
K-ion	Potassium-ion Batteries
Ni-Cd	Nickel-Cadmium Batteries
Ni-MH	Nickel-Metal Hydride Batteries
XAS	X-ray Absorption Spectroscopy
In-situ XAS	In-situ X-ray Absorption Spectroscopy
EXAFS	Extended X-ray Absorption Fine Structure
EIS	Electrochemical Impedance Spectroscopy
SEI	Solid Electrolyte Interface
SSE	Solid-State Electrolyte
PVD	Physical Vapor Deposition
CVD	Chemical Vapor Deposition

LIST OF ABBREVIATIONS (Continued)

Pt	Platinum
ODS	Oxide-Dispersion Strengthened
XRD	X-ray Diffraction
CV	Cyclic Voltammetry
SOC	State of Charge
AC	Alternating Current
Ip	Peak Current
NaCl	Sodium Chloride
RC	Resistor-Capacitor
Li_2CO_3	Lithium Carbonate
H_3BO_3	Boric Acid
NiO	Nickel (II) Oxide
Co_3O_4	Cobalt (II, III) Oxide
XANES	X-ray Absorption Near Edge Structure
PP	Polypropylene
$LiPF_6$	Lithium Hexafluorophosphate
EC	Ethylene Carbonate
DMC	Dimethyl Carbonate
$LiBO_3$	Lithium Borate
RT	Room Temperature
CB	Carbon Black
PVDF	Polyvinylidene Fluoride
MW	Molecular Weight
ECCCM	Electric Coin Cell Crimping Machine
BTS	Battery Testing System
CBO	Cross-Beam Optics
SLRI	Synchrotron Light Research Institute
$Li_2B_4O_7$	Lithium Tetraborate

LIST OF ABBREVIATIONS (Continued)

$Li_6B_4O_9$	Lithium Hexaborate
$LiBO_2$	Lithium Metaborate
B_2O_3	Boron Trioxide
ICE	Initial Coulombic Efficiency
mAh/g	Milliampere-hour per gram
mWh/g	Milliwatt-hour per gram
αV_2O_5	Alpha-phase Vanadium Pentoxide
δ-LiV_2O_5	Delta-phase Lithium Vanadium Pentoxide
γ-$Li_2V_2O_5$	Gamma-phase Lithium Vanadium Pentoxide
Li_2CoNiO_4	Lithium Cobalt Nickel Oxide
Li_2CoO_2	Lithium Cobalt Oxide
ΔE	Energy difference at the absorption edge
K-edge	Absorption edge related to the K-shell
CoO	Cobalt (II) Oxide
Co_3O_4	Cobalt (II, III) Oxide
VO_2	Vanadium (IV) Oxide
S_0^2	Scattering amplitude reduction factor
σ^2	Debye-Waller factor
ΔE^0	Energy shift at the absorption edge
N	Coordination number
TM-XAS	Transition Metal X-ray Absorption Spectroscopy
Li^+	lithium ions
ΔEp	The redox peak separation
$Li_6B_4O_9$	Lithium Hexaborate

CHAPTER I
INTRODUCTION

Meeting our expanding energy demands with sustainability in mind is imperative. in today's fast-paced world. While the Earth's crust still holds abundant coal reserves, overexploitation of this finite resource poses a severe threat to our climate. Furthermore, the production of crude oil has peaked, leading to a growing global need for cleaner, renewable energy sources (Yamada et al., 2010; Zeng et al., 2020). In this context, lithium-ion (Li-ion) batteries stand out as one of the most advanced and enduring energy storage solutions available. Renowned for their high energy density and portability, Li-ion batteries have become a staple in consumer electronics (Swiderska-Mocek and Naparstek, 2016).

Currently, lithium-ion batteries (LIBs) are crucial for portable devices, electric vehicles, and energy storage. However, their flammable liquid electrolytes pose safety risks in the event of damage. Additionally, increasing energy density within existing designs remains a challenge, especially in electric vehicles (EVs) (Xiao, Miara, Wang, and Ceder, 2019). Enhancing the performance of lithium-ion batteries (LIBs) can be achieved by improving the quality of cathode materials, which play a pivotal role in determining the energy storage capacity of LIBs at their maximum potential. Traditionally, lithium-ion battery electrodes have predominantly utilized crystalline materials. However, progress in cathode material development has been impeded due to the cost and complexity associated with high-capacity crystalline solids. These materials, while offering substantial capacity, are both expensive and challenging to manufacture, rendering the creation of crystalline cathode materials a complex endeavor (Afyon, Krumeich, Mensing, Borgschulte, and Nesper, 2014; Wei et al., 2018). The electrochemical properties of amorphous electrode materials often outperform their crystalline counterparts. Amorphous electrodes exhibit a short-range ordered structure, a substantial surface area, and free volume, allowing for lattice distortions without causing significant macroscopic phase transitions, ultimately enhancing kinetics.

Lithium borate-based glass has gained attention as a potential electrode material for rechargeable batteries due to its unique electronic and electrochemical properties. These borates are known for their high capacity and conductivity (Zeng et al., 2020). Borates have higher theoretical capacities than other types of inorganic salts (Yang, Xue, and Guo, 2021). Lithium-metal borate ($LiMBO_3$) offers a higher specific capacity of 200 mAh/g, outperforming the well-known lithium iron phosphate ($LiFePO_4$), which provides 170 mAh/g (Yamada et al., 2010). To enhance these capacities, various elements have been introduced into lithium borate glass, including transition metal oxides like cobalt, nickel, and manganese oxides. These metals are key in lithium-ion batteries and offer promising specific capacities. Transforming lithium nickel manganese cobalt oxide cathode material ($Li_xNi_yMn_zCo_{1-y-z}O_2$, $0 < x,y,z < 1$, abbreviated NMC) (high specific capacity of over 160 mAh/g) into an amorphous material using Li_2O-B_2O_3 glass as a base offers the potential for novel cathode materials for lithium-ion batteries. However, detailed information about lithium-borate-based glasses doped with Ni-rich $LiNi_xMn_yCo_zO_2$ (NMC) ($x > y, z$) materials is still limited and unclear (Liu et al., 2016).

This study is primarily focused on conducting a comprehensive, systematic examination of the physical and structural properties of samples derived from sample preparation melt quenching method, each of which involves distinct production procedures. The aim is to identify the most efficient and simple procedure for achieving optimal performance.

CHAPTER II

BACKGROUND

This section serves as a summary of the literature review, focusing on topics relevant to the research. It begins with the classification of electrochemical energy storage sources. The subsequent part delves into lithium-ion batteries, with a particular emphasis on glass batteries, followed by an exploration of their distinctive characteristics. The chapter concludes with a clear elucidation of the covered objectives and the research efforts undertaken within the scope of this academic thesis. sources

2.1 Classification of electrochemical energy storage

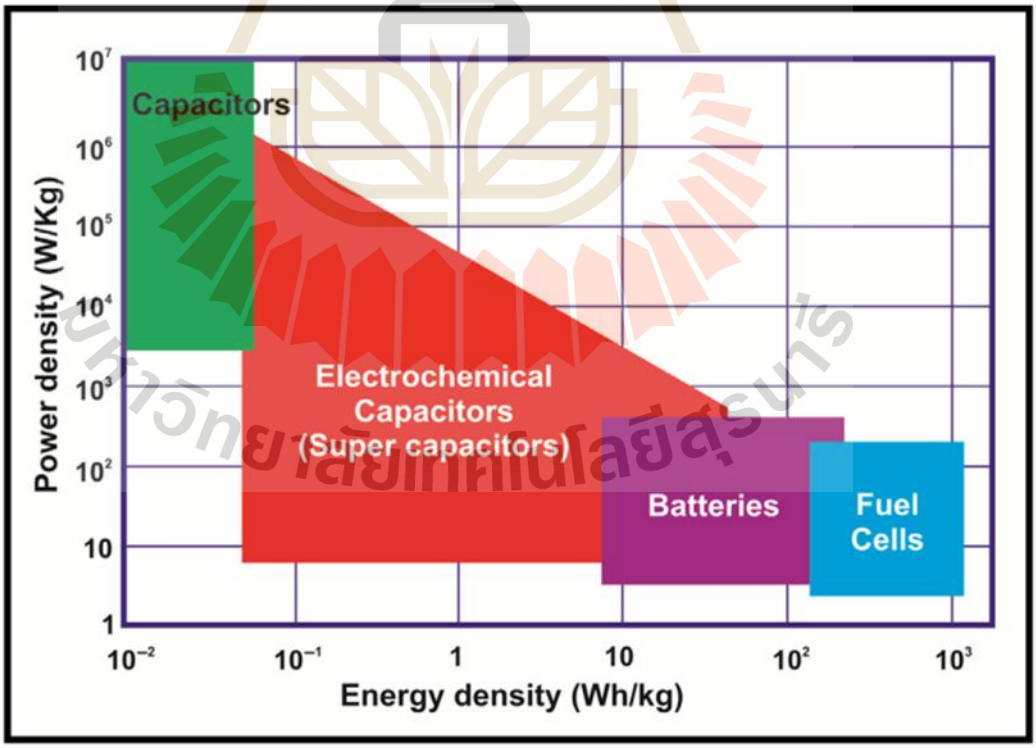

Figure 2.1 Ragone plot of various energy storage devices power and energy density (Sagadevan et al., 2021).

Energy storage devices (ESD) is characterized by their energy and power density. The Ragone plot, depicted in Figure 2.1, has long served as a standard reference in the battery research community (Christen and Carlen, 2000). Electrochemical Energy Storage (EES) is widely utilized for power generation and is now an integral part of portable electronics. It also finds applications in electrifying the transportation sector through batteries. The classification of ESS can be categorized as follows.

2.1.1 Fuel cells (FCs)

Fuel cells are energy conversion devices that directly convert the chemical energy from various fuels, into electrical energy with significantly higher efficiency compared to conventional power generation sources, both theoretically and in practice (Abdelkareem et al., 2021). Fuel cells have high energy density content but exhibit low power density due to their slower kinetic reactions (Sagadevan et al., 2021).

2.1.2 Batteries

Batteries are critical components in modern technology, enabling the seamless operation of electronic devices, from smartphones to electric vehicles. Their development has advanced significantly, with innovations focusing on higher energy density, and enhanced safety. In addition to their technological benefits, batteries contribute to reducing carbon emissions by supporting the integration of renewable energy systems like solar and wind power. As research continues, next-generation batteries are expected to become more efficient, cost-effective, and sustainable, further revolutionizing energy storage solutions. (Weber et al., 2011).

2.1.3 Supercapacitors

Supercapacitors are unique energy storage devices characterized by their electrostatic charge separation mechanism, setting them apart from traditional capacitors and batteries. They excel in delivering rapid bursts of power, boasting durability and high efficiency in charge-discharge cycles. However, supercapacitors are sensitive to temperature fluctuations, which can adversely affect their performance and lifespan. Additionally, their lower energy density compared to batteries makes them less suitable for long-term energy storage applications without frequent recharging (González, Goikolea, Barrena, and Mysyk, 2016; Hannan, Hoque, Mohamed, and Ayob, 2017; Sagadevan et al., 2021).

2.1.4 Capacitors

Capacitors store electrical energy at the interface between an electrolyte and a solid electrode. Capacitors have the highest power density because of their rapid charge and discharge capabilities, but they store the lowest amount of total energy per unit weight. Due to their low capacitance values, electrostatic capacitors are limited to low-power applications, or at most, they are used for short-term memory backup supplies (Sharma and Bhatti, 2010).

The Ragone plot of capacitors exhibits a decreasing slope due to the nature of energy storage in capacitors. Generally, energy storage in capacitors occurs through the accumulation of positive charges within the capacitor, resulting in electrostatic energy. This form of energy is less stable and can be stored in smaller quantities compared to the energy stored in batteries or supercapacitors. When a capacitor is discharged to provide energy in the form of an electrical current, the accumulation of electric charge within the capacitor decreases. Consequently, the electrostatic energy within the capacitor decreases as well. Typically, the rate at which the electrostatic energy decreases results in a decreasing slope in the Ragone plot, reflecting the gradual reduction in stored energy as the capacitor is used.

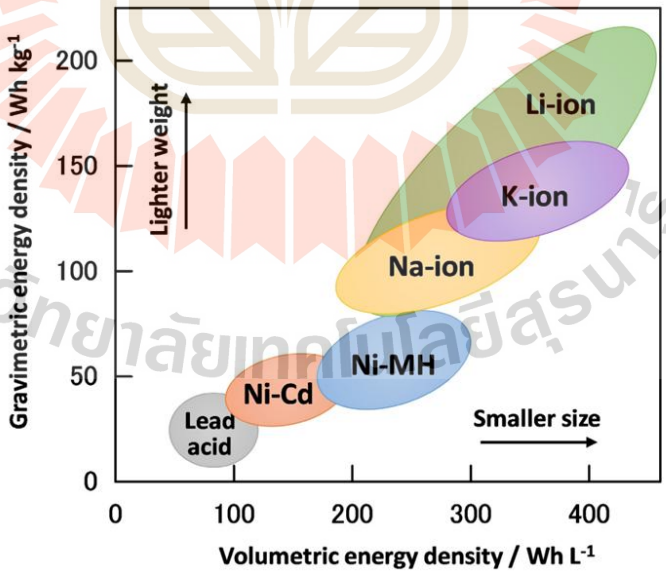

Figure 2.2 Volumetric and gravimetric energy densities of commercial batteries (lead-acid, Ni-Cd), Ni-MH, Na-ion, K-ion, and Li-ion batteries) (Kubota, Dahbi, Hosaka, Kumakura, and Komaba, 2018).

2.2 Batteries

There are various types of batteries, each with distinct features and applications, ranging from everyday devices to those commonly found in smartphones and laptops. These battery types include lead-acid, nickel-cadmium (Ni-Cd), nickel-metal hydride (Ni-MH), sodium-ion (Na-ion or NIBs), potassium-ion (K-ion), and lithium-ion batteries (Figure 2.2). This diversity of battery types enables us to efficiently meet various energy storage needs. Each type has specific advantages and limitations in terms of energy density, cost, cycle life, and environmental impact, making them suitable for different applications.

2.2.1 Lead acid batteries

Lead Acid Batteries are a well-established and widely used energy storage technology known for their reliability and low cost. These batteries operate through a chemical reaction between lead dioxide and sponge lead, producing electrical energy. They find applications in various fields, from automotive vehicles to uninterruptible power supplies, owing to their ability to deliver high current and provide a dependable source of energy (Christen and Carlen, 2000). While newer battery technologies have emerged, lead-acid batteries continue to play a significant role in the energy storage landscape, particularly in applications that prioritize cost-effectiveness and robustness.

2.2.2 Nickel-Cadmium (Ni-Cd) batteries

Nickel-Cadmium Batteries, also known as NiCad batteries, have been a prominent energy storage solution for several decades. These rechargeable batteries use nickel oxyhydroxide (NiOOH) as the cathode and cadmium metal (Cd) as the anode, typically delivering an on-line voltage of 1.2V. In industrial applications, Ni-Cd batteries are a close second to lead-acid batteries, primarily due to their exceptional performance in low-temperature conditions, flat discharge voltage, long lifespan, low maintenance requirements, and overall reliability (Christen and Carlen, 2000). However, a notable drawback is their capacity loss when partially discharged and recharged. To maintain their efficiency, Ni-Cd cells should be fully discharged to zero volts before recharging. Over time, environmental concerns have led to a decline in Ni-Cd battery usage due to the cadmium content, with many users transitioning to more environmentally friendly battery technologies (Kubota et al., 2018).

2.2.3 Nickel-Metal Hydride (Ni-MH) batteries

Nickel-Metal Hydride Batteries have gained prominence in the realm of rechargeable power sources. Their appeal lies in the higher energy density they offer in comparison to traditional nickel-cadmium (Ni-Cd) batteries. This increased energy storage capacity has made Ni-MH batteries a preferred choice for various applications, ranging from portable electronic devices to hybrid electric vehicles. Notably, Ni-MH batteries are celebrated for their eco-friendliness, extended cycle life, and reduced susceptibility to memory effects, making them a reliable and versatile power solution in a world increasingly driven by portable electronics and clean energy technologies (Christen and Carlen, 2000).

2.2.4 Potassium-ion batteries

Potassium-ion batteries, are gaining attention as a potential alternative to lithium-ion batteries for energy storage. These batteries use potassium ions for charge and discharge processes. Unlike lithium, potassium is abundant and cost-effective, which makes K-ion batteries an attractive option for large-scale energy storage applications. While they are still in the development stages and face certain technical challenges, such as electrode materials and overall performance, their potential for addressing the growing demand for energy storage in renewable energy systems and electric vehicles makes them a subject of increasing research.

2.2.5 Lithium-ion batteries

Lithium-Ion Batteries often abbreviated as Li-ion batteries, have revolutionized the world of portable electronics and electric vehicles. They are known for their high energy density, lightweight design, and ability to provide reliable, long-lasting power. The fundamental chemistry of Li-ion batteries involves the movement of lithium ions between the positive and negative electrodes during charge and discharge cycles. These batteries have become the preferred choice for a wide range of applications, from smartphones and laptops to electric cars and renewable energy storage systems, due to their efficiency and adaptability (Christen and Carlen, 2000).

Having high Volumetric and Gravimetric energy densities means that the battery has a greater capacity to store energy. It is lightweight and small. One important reason

why batteries are small and lightweight is a good thing is that they allow for efficient use and high power in tight spaces.

2.3 Glass Batteries

This section serves as a summary of the literature review, focusing on topics relevant to the current research. It covers aspects of glass batteries, including their history, definitions, and structure. Additionally, the use of lithium glass as the cathode material in the batteries under study is discussed. Finally, the section concludes with an overview of glass production techniques.

2.3.1 History of glass batteries

The battery was created by John B. Goodenough, a 97-year-old materials scientist, solid-state physicist, and professor of mechanical engineering and materials science at the University of Texas at Austin (well-known for creating the lithium-ion battery). Batteries comprise three basic components: an anode, a cathode, and an electrolyte. Most batteries have a liquid separator (electrolyte), but glass batteries are entirely solid, making them less dangerous and posing a lower risk of catching fire. These "glass batteries" (the electrolyte was based on a glass powder) have a two-times greater energy density than conventional lithium-ion batteries.

Although it has great and versatile features, this battery technology still faces many challenges to develop and improve its performance. For example, there are not enough suitable solid-state electrolytes (SSEs), and there is also a large interfacial resistance with insufficient interfacial ion/electron transport kinetics. One of the alternatives for improving SSBs' performance is improving cathode materials, as the total achievable capacity of SSBs is determined by the cathode materials.

Recent research focuses on overcoming these limitations by exploring different solid-state electrolyte materials, such as sulfides, oxides, and phosphates, which exhibit improved ionic conductivity. Additionally, there is ongoing work to address interfacial stability, including the development of coatings for cathodes to reduce resistance at the interface. The search for more stable, high-capacity materials like lithium-rich layered oxides, spinel-based cathodes, and even the use of lithium metal

as an anode are seen as crucial steps toward enhancing the energy density, cycle life, and overall safety of solid-state batteries. If these challenges are successfully addressed, glass batteries could revolutionize the energy storage industry, offering safer, more durable, and higher-performance alternatives to traditional lithium-ion batteries (Zhao et al., 2019).

2.3.2 Definition of glass

Glass, with its unique properties including optical transparency, structural strength, and durability, has been a part of human civilization for millennia. Its versatility has led to diverse applications, ranging from advanced technologies like laser glass, optical fibers, and solar glass to everyday items such as glass water containers, bottles, and decorative glass clocks. Additionally, glass plays a role in cutting-edge fields like renewable energy and electronics, where it is used as an electrode in batteries (Karmakar, 2017). It is imperative to know the relationships between different types of glasses.

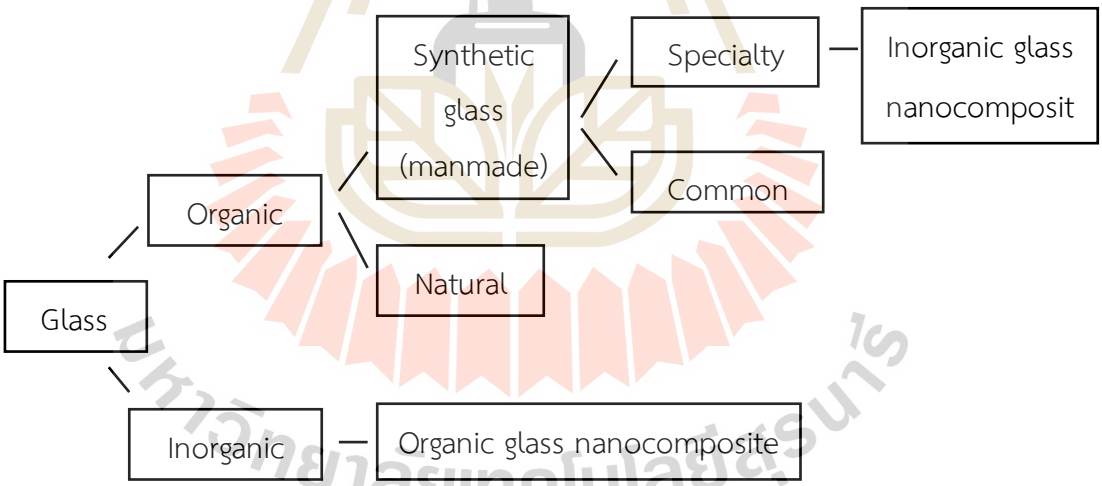

Figure 2.3 The relationships of different types of glasses (Karmakar, 2017).

Figure 2.3 illustrates the classification of glass based on its chemical composition, resulting in two primary categories: inorganic and organic glasses. Inorganic glasses can further be categorized into natural glasses, like obsidian or pechsteins, found in volcanic rocks, and synthetic glasses, which are human-made through the melting of

raw materials and manufacturing processes. Synthetic glasses, in turn, can be divided into two subcategories: common and specialty glasses. Common glass, which includes items like windows, tumblers, bottles, lamps, spectacles, mirrors, and more, serves every day, general purposes (Karmakar, 2017).

2.3.3 Structure of glass

Numerous structural theories have been proposed to explain glass formation. These theories include Goldschmidt's radius ratio criterion and Zachariasen's random network theory, which focus on coordination numbers. Smekal's mixed bonding rule and Stanworth's electronegativity rule, on the other hand, are based on bond type. Sun's single bond strength criterion is rooted in bond strength, while Dietzel's field strength criterion and Phillips' topological constraint model are other relevant models. It's worth noting that some of these theories are now primarily of historical significance and are discussed in detail by Rawson.

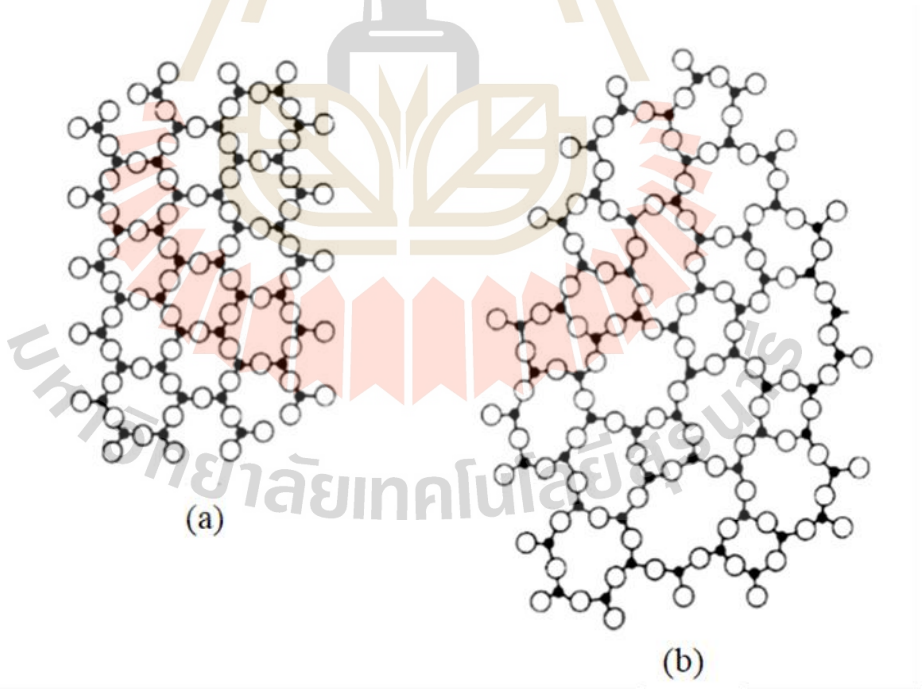

Figure 2.4 Atomic structural representation of (a) A_2O_3 crystal (b) A_2O_3 glass.

In our discussion, we will concentrate on Zachariasen's theory and the latter three models. In a seminal paper that significantly influenced the field of glass science,

Zachariasen put forth a compelling argument. He contended that because the mechanical properties of glasses closely resemble those of their crystalline counterparts, the atomic forces in both materials must be of a similar magnitude. The broad diffuseness observed in x-ray diffraction spectra for glasses strongly implied that glass possesses an extraordinarily large unit cell, forming a three-dimensional random network. Consequently, this randomness leads to glass having higher internal energy compared to crystals. Zachariasen believed that the disparity in internal energy between glass and crystals must be minimal; otherwise, there would be a substantial driving force towards crystallization. Additionally, he suggested that this slight energy difference necessitates an open and flexible atomic structure for glass.

In ionic crystals, it's common for the cation polyhedra to share corners. This is especially the case when dealing with cations that have a small radius but a high charge. Zachariasen proposed that sharing corners is a fundamental requirement for achieving a structure that is both open and random. So, if we imagine a hypothetical compound like A_2O_3 crystallizing in two dimensions, the atomic arrangements in both the crystalline and glassy forms should resemble what's depicted in Figure 2.4. In both cases, you'll see triangles made up of AO_3 units connecting at their corners (Varshneya, 2013). However, in the glassy form, there's an element of disorder due to variations in the A-O-A bond angles (referred to as bond angles) and slight changes in the A-O bond lengths. It may also be noted that the triangles or the O-A-O angles themselves need not be deformed much (Varshneya, 2013).

2.3.4 Glass on battery electrode

The preference for using lithium-ion batteries over silica as glass on battery electrode is due to several reasons. Lithium-ion batteries offer higher energy storage capacity, lighter weight, better efficiency in energy storage and release, and greater durability in various environmental conditions. They also provide better control and dissipation of heat, reducing the risk of fire and other hazardous incidents. Additionally, lithium-ion batteries have a longer lifespan and lower energy loss during operation, making them more advantageous for applications requiring safety, efficiency, and lightweight properties.

Crystalline materials have been widely utilized as cathode materials for lithium-ion batteries (LIBs), but they face limitations related to factors like symmetry, phase transitions, crystal orientation, and cost. The development of high-capacity crystalline materials is often constrained. Amorphous electrode materials, on the other hand, show promise with their short-range ordered structure, high surface area, and free volume, allowing for lattice distortion without macroscopic phase transitions and thus improving kinetics. Several studies indicate that amorphous electrodes exhibit enhanced cyclic performance and higher capacity compared to crystalline electrodes (Wei et al., 2018).

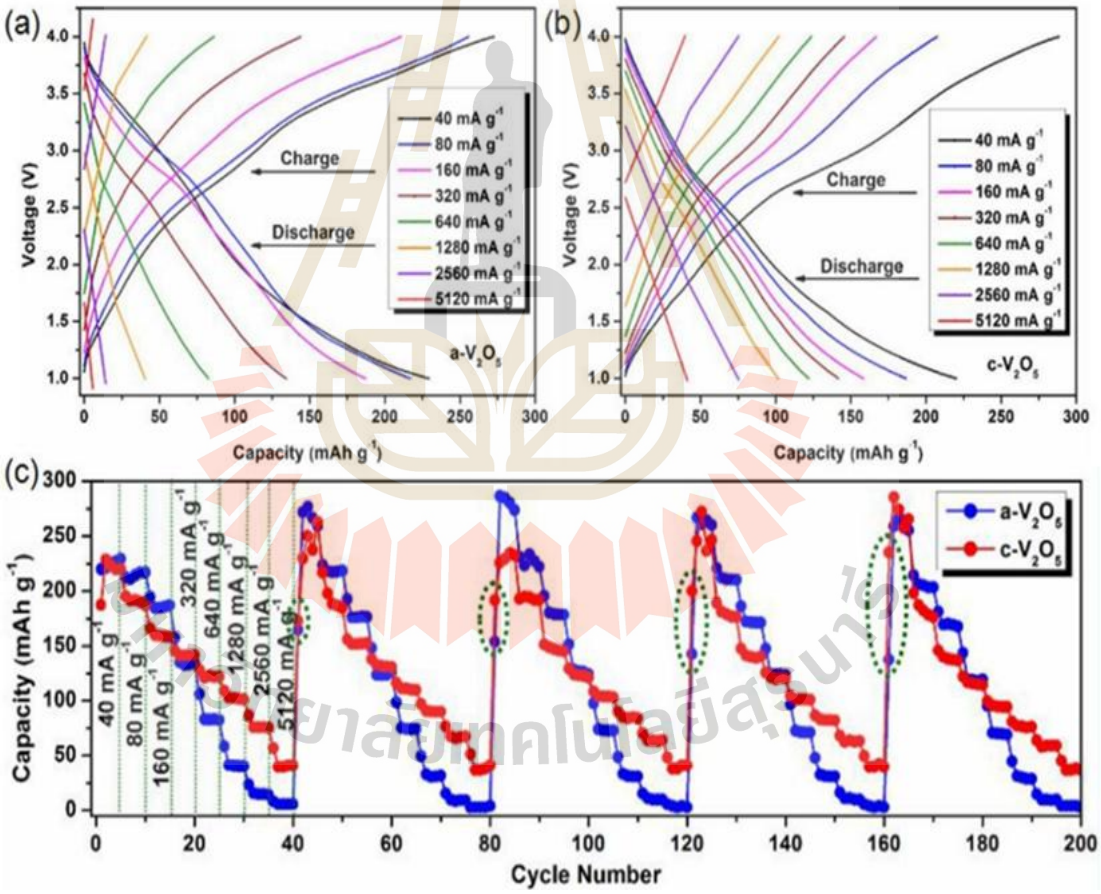

Figure 2.5 The galvanostatic discharge/charge curves for two types of V_2O_5 cathodes, a) amorphous (a-V_2O_5) and b) crystalline (c-V_2O_5), were recorded at different current densities within the voltage range of 1.0 to 4.0 V. Additionally, c) comparison of the rate performance between these two cathodes (Liu et al., 2016).

In the following section, we will review various research works that have successfully employed glass materials for use in the electrodes of batteries. These studies have significantly contributed to enhancing the performance and efficiency of electrochemical energy storage systems. By exploring the latest advancements in glass battery technology, we can gain insights into the promising innovations that may shape the future of energy storage solutions.

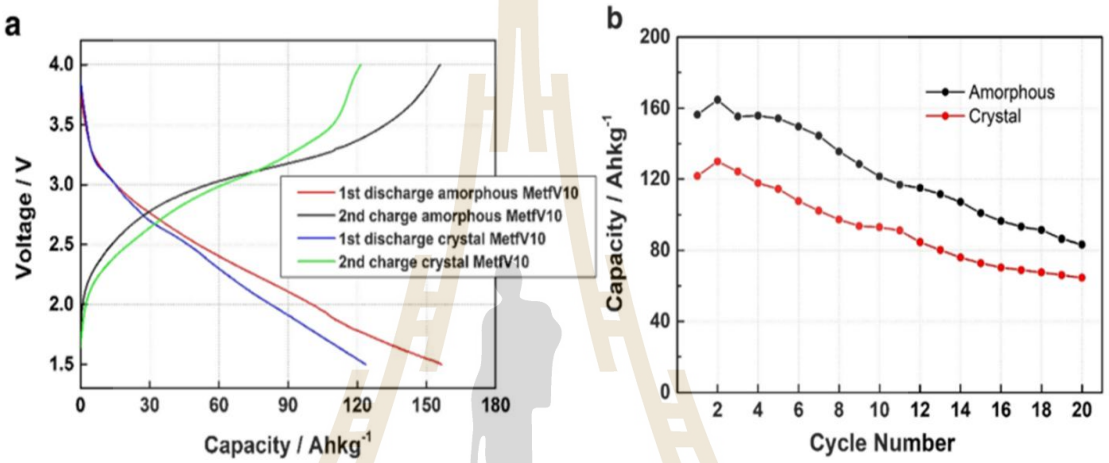

Figure 2.6 a) First discharge and second charge curves of LIBs using amorphous and crystal MetfV10 cathodes. b) Cycle performance of LIBs using amorphous and crystal cathodes (Wang, Isobe, Matsumura, and Yoshikawa, 2018).

In 2014, Shikun Liu and a team conducted a comparative analysis of amorphous and crystalline V_2O_5 cathodes in sodium-ion batteries. They created amorphous V_2O_5 (a-V_2O_5) cathodes by subjecting V_2O_5 samples to drying at 120°C for 10 hours in a vacuum chamber. Subsequently, they annealed these cathodes at 350°C for 4 hours in an air environment to form crystalline V_2O_5 (c- V_2O_5) cathodes. The results showed that a-V_2O_5 cathodes exhibited higher reversible capacities at low current densities (217.1 and 186.9 mAh/g at 80 and 160 mAh/g, respectively) compared to c-V_2O_5 cathodes (186.6 and 158.3 mAh/g), as depicted in Figure 2.5c. In contrast, the cathode composed of c-V_2O_5 exhibits superior specific capacities compared to the cathode composed of a-V_2O_5 under conditions of high current densities. The electrochemical findings presented in this study demonstrate that amorphous materials possess

notable characteristics that make them a compelling choice for utilization as cathode materials, particularly under conditions of low current densities (Liu et al., 2016).

Moreover, in 2018, Heng Wang and his group reported on the properties of amorphous and crystalline cathode materials for lithium-ion batteries. In Figure 2.6, the electrochemical performance of the amorphous and crystalline MetfV10 cathodes was systematically investigated. The galvanostatic discharge and charge curves of the two different (Figure 2.6a) cathodes showed that the discharge capacities of the amorphous and crystalline MetfV10 cathodes in the first discharge were 156 and 122 mAh/g, respectively. Moreover, Figure 2.6b shows the cycle dependence of the discharge capacities for the two cathodes. It can be clearly seen that the amorphous cathode maintains a capacity greater than the crystalline cathode (approximately 100 mAh/g after 20 cycles). The disordered structure of the amorphous cathode may help Li ions more easily intercalate into the materials, resulting in a decrease in resistance. These results show that amorphous materials are a good candidate to replace or develop cathode materials (Wang et al., 2018).

2.3.5 Glass production

Currently, there are a range of techniques for creating glass, such as melt-quenching, sol-gel, chemical vapor deposition, sputtering, and others. The melt-quenching method is widely used because of its simplicity, ease of use, and suitability for producing various types of glass in small-scale laboratory settings. In light of the information presented above, the following discussion will proceed as follows:

2.3.5.1 Melt-quenching technique

The melt-quenching technique, a widely employed method in materials science and glass manufacturing, involves the melting of raw materials or glass precursors. Once molten, the glass is rapidly cooled to solidify, resulting in a transparent and non-crystalline material. This technique is valued for its simplicity and adaptability to small-scale production, making it a pivotal process for crafting various glass compositions and shapes, particularly in research and laboratory settings.

The Melt-Quenching Technique has been extensively investigated for the production of lithium borate glass, and it is the primary method employed in

creating most types of glass today. This process involves heating the raw material mixture, or batch, to temperatures ranging from 1100 to 1600°C, followed by controlled melting for a specific duration. After casting, any residual thermal stresses are eliminated through an annealing process conducted near the glass transition temperature of the respective glasses, resulting in what are known as "as-prepared glasses." To prepare these as-prepared glass samples for various characterization methods, they are typically sawed, ground, and polished.

The initial steps involve selecting suitable raw materials and then preparing the batch through chemical calculations, weighing, and thorough mixing. The uniformity of the glass melt is maintained by periodically stirring it with a platinum or silica glass rod. Glass melting crucibles can be crafted from a range of materials, including fused silica (SiO_2), alumina (Al_2O_3), pure platinum (Pt), oxide-dispersed-strengthened (ODS) platinum, platinum-gold (Pt-5% Au), platinum-rhodium (Pt-10% Rh), or platinum-iridium (Pt-10% Ir). To prevent contamination, it is advisable to use pure platinum (Pt) or ODS platinum crucibles. Appropriate caps can be employed to slow the rate of evaporation loss.

2.3.5.2 Sol-Gel Method

The sol-gel method has gained increasing official recognition as a primary technique for glass fabrication. This wet-chemical approach utilizes liquid sources to synthesize both inorganic materials and organic-inorganic hybrids, making it a preferred method in various research and industrial settings. Silicate systems, particularly, have been extensively explored within the sol-gel synthesis framework due to the availability of molecular silicon sources like tetra alkoxysilanes, which offer moderate reactivity. By undergoing hydrolysis and polycondensation reactions, these compounds yield silica gels, which can be converted into silica glasses at relatively low temperatures (around 1000–1500°C) without melting. This process, devoid of melting, is gaining official recognition due to its numerous advantages over conventional methods. It allows for enhanced dopant concentration, broader compositional range, and tailored photo- and magnetoactive centers within the glass

structure. Despite challenges, such as the tendency of sol-gel-derived wet gels to fracture during drying, efforts to refine techniques and overcome obstacles are steadily improving. Consequently, the sol-gel method is becoming increasingly institutionalized as a pivotal approach in the fabrication of monolithic silica glasses and specialized functional glass compositions (Kajihara, 2013).

2.3.5.3 Chemical Vapor Deposition

The Chemical Vapor Deposition (CVD) technique for glass is an official and established method used to deposit thin films or coatings onto glass substrates. It involves the chemical reaction of gaseous precursors to form a solid material on the surface of the glass. The CVD process typically requires precise control over temperature, pressure, and gas flow rates to achieve the desired deposition characteristics. This method is commonly employed in industries requiring high precision and performance, such as optical coatings, semiconductor manufacturing, and electronics. CVD offers advantages like uniform thickness distribution, excellent adhesion, and the ability to deposit complex materials with tailored properties. As a result, it has become an increasingly institutionalized approach in the fabrication of advanced glass products for various applications (McCurdy, 1999).

2.3.5.4 Sputtering Method

The Sputtering method, employed for glass applications, involves the deposition of thin films or coatings onto glass surfaces through a process known as physical vapor deposition (PVD). This technique utilizes high-energy ions to dislodge atoms from a target material, which then deposit onto the glass substrate, forming a thin film. Taking advantage of a vacuum environment, the sputtering process allows for precise control over film thickness, composition, and structure. Widely utilized across various industries, including electronics, optics, and automotive, sputtering enables the creation of functional coatings such as transparent conductive layers and anti-reflective coatings. Its versatility and capability to enhance the properties of glass

make sputtering a pivotal method in modern glass fabrication and technological advancements (Stan et al., 2023).

2.4 Characterization techniques

In this section, we will delve into the characterization techniques employed in this study. Specifically, one of the key techniques utilized for measurement and analysis is XRD.

2.4.1 X-ray diffraction (XRD)

X-ray diffraction is a crucial technique for studying the atomic and molecular structure of materials. It is widely used in scientific fields like chemistry, physics, and materials science to reveal the arrangement of atoms in crystal lattices. XRD helps determine the crystallographic properties of various substances by measuring X-ray scattering angles and intensities, providing valuable insights into material structures. This technique has been pivotal in uncovering the structures of many compounds, enhancing our understanding of matter's properties.

The present chapter first presents a condensed overview of the generation of X-rays as well as the theory of diffraction of X-rays by crystals. Subsequently, the methods for analyzing X-ray patterns of both amorphous and crystalline materials are presented.

During the war years, extensive research was conducted to quantify radiation dosage, with a particular focus on X-ray spectra. In 1912, the x-ray diffraction experiment, which revealed x-rays as electromagnetic waves, garnered significant attention in the scientific community. Max von Laue, a Nobel Prize laureate, presented a compelling synthesis of evidence supporting both the electromagnetic radiation model and the particle-like explanation. The Bragg father-and-son duo, using x-rays as a crystallographic tool, confirmed that x-rays are electromagnetic waves capable of interfering with lattices, providing atomic-scale information about crystal structures inaccessible to visible light. This pioneering technique led to the first images enabling the inference of atomic structures in solids (Kitaigorodsky, 2012), which was established

in the early 20th century. The Braggs demonstrated a remarkable ability to precisely characterize fundamental structures, including that of common substances like rock salt (NaCl) (Borisov and Podberezskaya, 2012). The examination of X-ray intensities reflected by crystals further substantiated Niels Bohr's atomic model and the concept of chemical bonding (Sheldrick, 1998).

In the past few decades up to the present day, X-ray analysis techniques have been employed to accurately determine the distances between atoms and their arrangement in various substances. These techniques have found applications in numerous scientific disciplines.

2.4.1.1 Principle of X-ray diffraction

In this section, we will provide an overview of the fundamental principles of X-ray diffraction (XRD) techniques.

X-rays, characterized by wavelengths between 10^{-3} and 10^{1} nanometers (Spieß, Behnken, Genzel, Schwarzer, and Teichert, 2009), are typically produced using sealed tubes and rotating anodes. In this process, electrons are generated by heating a tungsten filament within a vacuum. These electrons are subsequently accelerated through a high electric potential field and focused on a target material, resulting in the emission of X-rays. Incident electrons generate X-rays through two mechanisms: first, the deceleration of electrons results in the emission of X-ray photons, producing a continuous spectrum known as Bremsstrahlung (Schwartz and Cohen, 2013). Second, when atoms are ionized by incoming electrons, inner-shell electrons are ejected, and outer-shell electrons fill the resulting gaps. The energy difference between these electron transitions leads to the emission of characteristic X-rays with energy levels specific to the material (Epp, 2016).

The methods are fundamentally founded on the diffraction of X-rays by regularly spaced atomic planes and the detection of the diffracted signal in terms of either angle or energy. The geometric interpretation of X-ray diffraction, based on constructive interferences, was initially expounded by W.L. Bragg in 1913 (Bragg and Thomson, 1914). Bragg's solution to X-ray diffraction views it as the reflection of X-rays

from the atomic planes of a crystal, following the laws of reflection. A crystal with Miller indices [hkl] is considered a series of parallel atomic planes separated by a distance d. Figure 2.7 details the geometric conditions for diffraction and the derivation of Bragg's law (Equation 2.1).

$$n\lambda = 2d_{hkl}\sin(\theta) \qquad \text{Equation 2.1}$$

In Equation 2.1, 'n' represents the order of diffraction, 'λ' denotes the wavelength of the incident beam in nanometers (nm), 'd_{hkl}' signifies the lattice spacing in nanometers, and 'θ' corresponds to the angle of the diffracted beam in degrees.

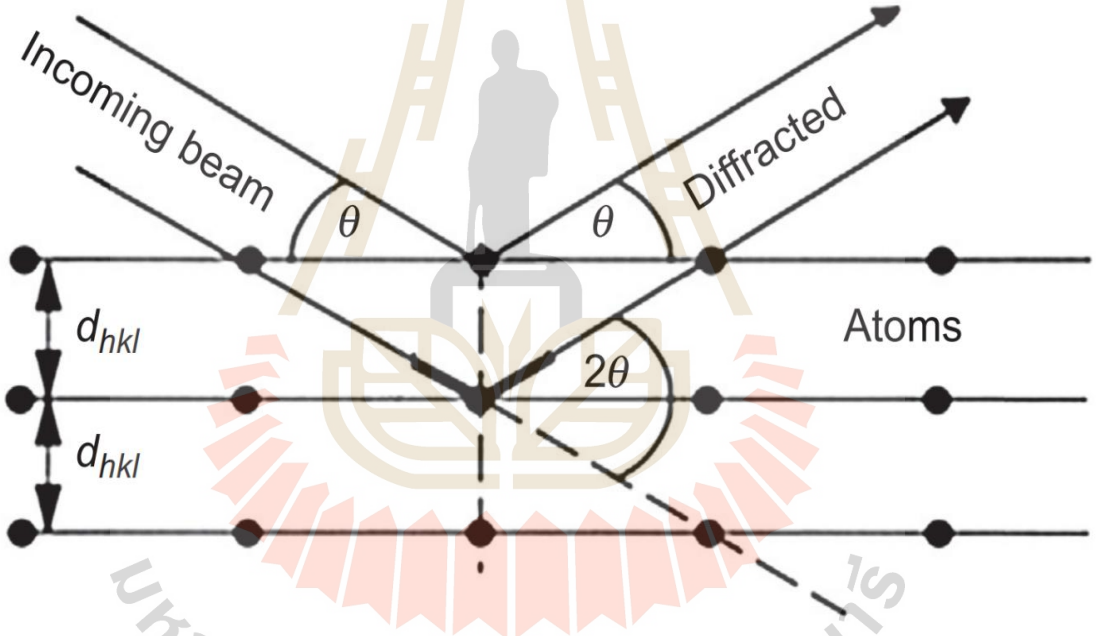

Figure 2.7 A simplified model of the Bragg equation (Epp, 2016).

Crystals are ordered arrangements of atoms, and X-rays can be thought of as electromagnetic radiation waves. When X-rays hit a crystal, the atoms scatter them, mostly because the rays interact with the atoms' electrons. Elastic scattering is the name given to this process, in which the electron plays the role of the "scatterer." When scatterers are arranged regularly, the resulting spherical waves also behave

predictably. In most directions, these waves cancel each other out through destructive interference, but in a few, as determined by Bragg's law (Equation 2.1).

For this expression, the wavelength is denoted by lambda, the distance separating atomic planes by d, and the angle of incidence of the X-ray beams by theta, where n is an integer (1, 2, 3,...n). Because it "reflects" off an adjacent atomic plane, an X-ray beam travels in a more circuitous (but still parallel) path. It is necessary for the incident X-ray beams to have a path length difference of exactly 1 for constructive interference to occur and a strengthened diffracted beam to be produced (Epp, 2016).

2.4.1.2 Phase identification of X-ray diffraction

The building blocks of a crystal are repeated patterns (Figure 2.8d) that are ordered in three dimensions. However, atoms in amorphous materials are scattered randomly throughout three dimensions (Figure 2.8b), so they lack periodicity. This scenario calls for attention to X-ray scattering by atoms. X-rays will scatter in only certain directions when they hit the lattice planes due to the periodic arrangement of the atoms (formed by atoms). Extremely bright peaks will result from this (the width of the peaks depends on other variables). In the amorphous state, X-rays scatter in many directions, producing a broad, uneven peak (2 theta) rather than concentrated high-intensity peaks. If there is enough amorphous phase to give a peak, then you will get the peaks of the relevant phase, but they will not be sharp, because an XRD pattern is composed of the sum of the contributions of all constituent phases. It's possible that a higher proportion of the amorphous phase will appear in the diffraction pattern if the experiment is conducted at a low angle. A sharp peak of the crystalline phase's preferred orientation and a fuzzy peak of the amorphous phase's strongest peak will be visible if both phases have peaks. As a result, the amorphous phase will only show its strongest peak once. The second peak, if present, may be discernible if its intensity is sufficiently high, but the contrast between them will be low (Figure 2.8a,c) (Epp, 2016; Nunes, Mahendrasingam, and Suryanarayanan, 2005).

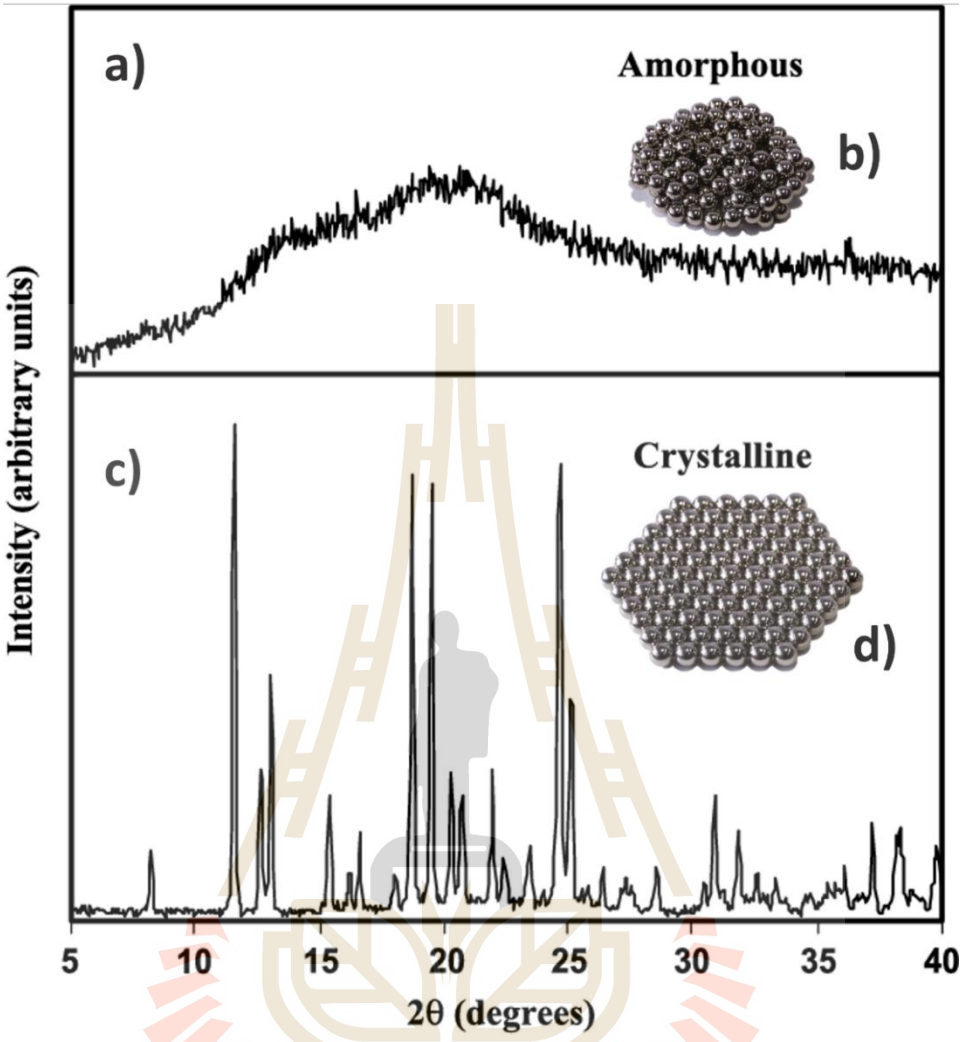

Figure 2.8 The XRD patterns of a) amorphous and c) crystalline forms, along with the crystal structure diagrams of b) amorphous and d) crystalline forms, are presented and summarized (Nunes et al., 2005).

2.4.2 The cyclic voltammetry (CV)

Cyclic voltammetry (CV) is used to examine the energy generated in batteries or other energy storage devices by measuring the current flowing through the energy-setting component (electrode) in the device being tested. The key feature of CV is its ability to measure energy in various forms over time. Applying a square wave voltage, allows observation of changes in current over time, aiding in the assessment of energy occurring in the device during specific operational periods. CV measurements help improve the understanding of the behavior of energy storage devices.

2.4.2.1 Principles of cyclic voltammetry

Cyclic voltammetry is a cornerstone technique in electrochemistry, utilized to investigate the fluctuations in electrical current passing through a resistor as the potential of an electrode varies at a designated temperature and pressure. This analytical method is frequently employed to study the electroactivity of substances undergoing chemical transformations during an electric current. Widely utilized in research and development, especially in the realms of organic chemistry, materials science, and biotechnology, cyclic voltammetry offers insights into the electrochemical behavior of various substances on an atomic scale. By systematically altering the potential within predefined limits, and oscillating between positive and negative values, cyclic voltammetry generates data that reveal the electrochemical properties of the substance under scrutiny. Analyzing the resulting cyclic voltammogram enables the prediction of the electrode's capacitive attributes and identification of redox peaks corresponding to reduction and oxidation processes. Through this method, the substance's oxidation and reduction potentials can be determined with precision and accuracy (Choudhary, Jothi, and Nageswaran, 2017).

Cyclic voltammetry is rooted in the principle of linear sweep voltammetry, a method that tracks current while linearly sweeping potential over time. The rate of voltage change, known as the scan rate (m s-1), characterizes this technique. Linear sweep voltammetry yields diverse outcomes influenced by factors such as the rate of electron transfer, electrochemical reactivity of materials, and the chosen scan rate. Results typically manifest as either anodic or cathodic peaks, depicted in Figure 2.9a. While similar to linear sweep voltammetry, cyclic voltammetry diverges by not concluding with a single sweep within a fixed voltage range. Instead, it cyclically returns from E2 to E1 after reaching the endpoint. This cyclical behavior gives rise to the term "cyclic," with the resulting current versus voltage plot termed a 'cyclic voltammogram', as illustrated in Figure 2.9b. In cyclic voltammetry, the scan rate (v) is a pivotal parameter. Voltage sweeps from E1 to E2, representing the slope of a linear voltage change during measurement. Repeating multiple cycles under consistent conditions provides additional insights into voltage, reversibility, and cyclability of

redox reactions. Furthermore, adjusting the scan rate allows for the investigation of electrochemical redox reaction kinetics.

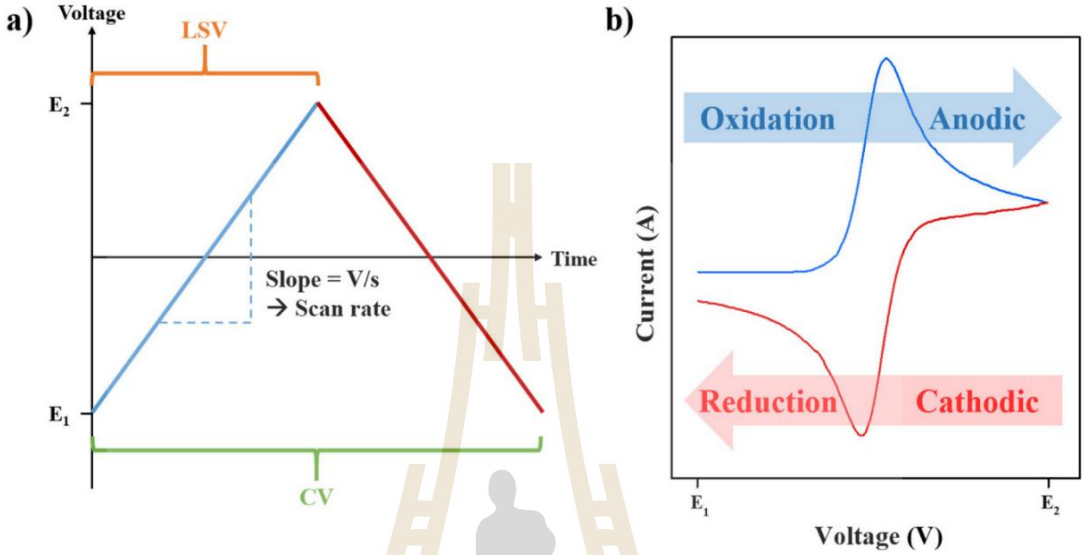

Figure 2.9 a) The voltage versus time profile distinguishes between linear sweep and cyclic voltammetry. b) A standard cyclic voltammogram illustrates both cathodic and anodic peaks (Kim et al., 2020).

For the differential capacity (dQ/dV) plot, it is recorded based on a similar principle as the cyclic voltammogram. Although it provides useful information on the redox reactions of electrochemical systems, the difference between the cyclic voltammogram and the dQ/dV plot should be recognized, as the cyclic voltammogram contains rate information. In general, the current (I) is plotted on the y-axis versus the voltage (V) on the x-axis in the cyclic voltammogram, and it can be transformed into a dQ/dV plot. For the transformation of a cyclic voltammogram to a dQ/dV plot, the I and V can be expressed as.

$$V = vt \qquad \text{Equation 2.2}$$

$$dt = \frac{dV}{v} \qquad \text{Equation 2.3}$$

$$I = \frac{dQ}{dt} \qquad \text{Equation 2.4}$$

where v is scanning rate (Vs^{-1}), V is the voltage (or potential, V), I is the current (A), Q is charge stored (Ah), and t is time (s). And the formula 2.5 which indicate the y-axis of dQ/dV plot was obtained by combining the equation 2.3 and 2.4

$$\frac{I}{v} = \frac{dQ}{dV} \qquad \text{Equation 2.5}$$

Moreover, it is necessary to understand the different experimental conditions between galvanostatic cycling (charge-discharge) and CV in terms of a driving force for electrochemical reactions; the potential increases linearly with time in CV, whereas the current is maintained during galvanostatic cycling. Regardless of state of charge (SOC) of the working electrode, these forced changes in potential increase.

The current beyond the operating limits of the cell. Thus, it would be difficult to make a comparison of accessible capacity. In addition, the IR drop of the cell remains consistent during the constant current scan, which depends on the CV sweep, so the peak position and shape can be changed as shown in Figure 2.10. Therefore, before using dQ/dV plot, it is necessary to understand the commonalities and differences between CV and dQ/dV (Kim et al., 2020).

The CV experiment can be performed with a single cycle or with numerous cycles of varying voltage. The scan rate is defined as the slope of the ramp signal in volts per unit time. This scan rate can vary from a few hundredths of a millivolt per second to tens of thousands of volts per second. To better understand the cell's electrochemistry, the scan rate can be adjusted. Therefore, the test sample's voltametric behavior is highly dependent on the scan rate. It is reasonable to anticipate that the oxidation and reduction peak currents and peak potentials will vary with the scan rate. A good rate capability and improved pseudocapacitive behavior of the electrode material are both indicated by an increase in the peak current (faradaic current) with an increase in the scan rate. The presence of the electroactive species at the surface of the electrode (the working electrode) causes a greater number of redox reactions as the scan rate increases. However, if the scan rate is too slow, the products of the reduction or oxidation can take part in a chemical process whose products may not be electroactive, and the peak (either the forward or reverse scan peak) would be

missed. It is possible to determine this peak current in the CV by utilizing the Randlese-Sevcik equation:

$$I_p = 2.69 \times 10^5 \, n^{\frac{3}{2}} AC\sqrt{vD} \qquad \text{Equation 2.6}$$

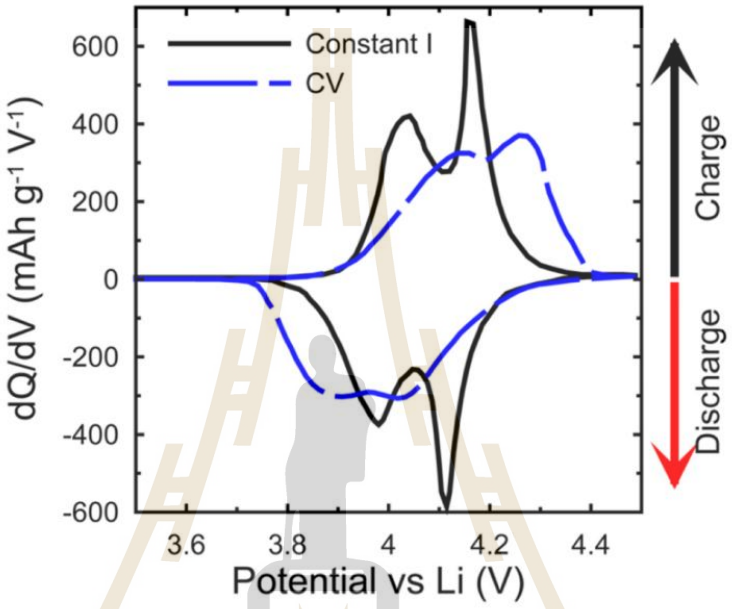

Figure 2.10 CV and dQ/dV curve of $Li_xMn_2O_{4+}\delta$ vs Li metal with constant current experiment as C/8 = 0.33 mA/cm^2 and CV: 0.04 mV/S (sweeps up and down in 6.9 h). Reprinted with permission (Potyrailo and Maier, 2006).

where I_p denotes the peak current, n refers to the number of electrons in the redox reaction, A indicates the area of the working electrode, C signifies the concentration of the electroactive species at the electrode, v represents the scan rate, and D denotes the diffusion coefficient of the electroactive species. Each of these factors is critical in establishing the peak current in CV (Choudhary et al., 2017).

Capacitance is measured at varying sweep speeds to provide a comprehensive picture of its behavior in the CV. In addition, the following formula can be used to estimate the material precise capacitance:

$$C_s = \frac{\int IdV}{vm\Delta V} \qquad \text{Equation 2.7}$$

where ΔV is the potential window (V), m is the mass of electroactive material (g), v is the scan rate (mV/s), and $\int$ IdV is the area under the curve in the plot of I versus V.

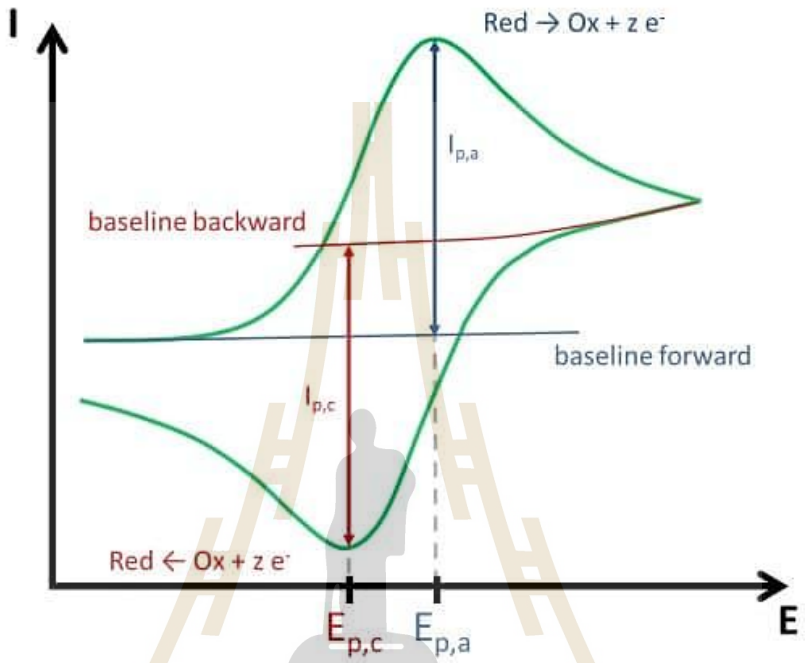

Figure 2.11 The CV of a freely diffusing reversible species, together with an indication of the peak currents and peak potentials for the anodic and cathodic peaks.

A cyclic voltammogram involves regulating the voltage and monitoring the current. The potential for either growth or decay is linear. The scan rate v is the rate of change of the potential over time. Mathematically speaking, this corresponds to the slope of the linear potential (see equation 2.8).

$$V = \frac{\partial E}{\partial t} \qquad \text{Equation 2.8}$$

Potentials at the outset are often inactive, meaning no electrochemical reaction is taking place. In most cases, the linear sweep of the potential will cross the formal potential of the species under study (Figure 2.11). After a certain threshold is crossed, the slope of the linear potential flips, such that a negative potential becomes

a positive one and vice versa. The vertex potential is the name given to this potential. When the potential returns to its initial value, the cycle is complete.

This procedure may be repeated as often as desired. The purpose of performing several cycles is to gauge the robustness of a system. In most modern software, the potential sweeps between the two vertex potentials and begins at a potential between these two, with the opportunity to specify a start potential in between.

2.4.2.2 The shape of a cyclic voltammogram

An example CV for a solution with a single freely diffusing reversible species is shown in Figure 2.11. The peak data is read in the same way. The peak information includes the cathodic peak currents Ip, c, and potential Ep, c, as well as the anodic peak current Ip, a. The arrangement of a curriculum vitae can provide a wealth of qualitative data. Either by analyzing the peaks themselves or by monitoring how they evolve over the course of a series of observations, more crucial information can be gleaned. Please be aware that it is more challenging to establish a baseline for the back scan because the current at the beginning of the back scan incorporates the diffusion-limited current of the forward scan. In this section of the guidelines, you'll find details on how to account for this circumstance. If the peak current is being monitored solely for quantitative analysis purposes, then the baseline offset is irrelevant.

2.4.3 Electrochemical Impedance Spectroscopy (EIS)

Electrochemical Impedance Spectroscopy (EIS) is a powerful and versatile technique used to investigate the electrical properties of materials and the kinetics of electrochemical reactions. EIS is widely employed in various fields, including battery research, fuel cells, corrosion studies, and sensor development. This technique provides detailed information about the electrochemical processes occurring at the electrode-electrolyte interface and within the bulk of the material.

2.4.3.1 Basics of Electrical Impedance Spectroscopy

Impedance spectroscopy is a non-destructive measurement technique that can be used to examine a battery or parts of a battery (e.g. a half-cell, i.e. only the anode). Figure 2.12a shows the basic measurement principle. For the

measurement, the cell is connected at its two poles to an impedance spectroscopy meter. These are offered by various manufacturers such as Biologic or Gamry Instruments. There are different measurement variants, but one of the standard measurement methods is galvanostatic impedance spectroscopy. In this, a sinusoidal alternating current is applied to the cell. A low current is set, since only then does the battery exhibit linear behavior to a first approximation [1]. The alternating current pulse then leads to a phase-shifted voltage response. The behavior follows the basic equations of AC theory. With the current amplitude I0 it results in the following AC time signal:

$$I(t) = I_0 * \sin(\omega t) \qquad \text{Equation 2.9}$$

The voltage of the cell responds to this excitation and accordingly the following phase-shifted AC voltage time signal can be measured:

$$U(t) = U_0 \sin(\omega t + \phi) \qquad \text{Equation 2.10}$$

EIS involves the application of a small, alternating current (AC) signal to an electrochemical system and the measurement of the resulting voltage response. By varying the frequency of the AC signal over a wide range, typically from milli-hertz to mega- hertz, EIS can probe different processes occurring in the system. The impedance (Z), a complex quantity, is calculated as the ratio of the AC voltage (U) to the AC current (I) at each frequency (ω):

$$Z(\omega) = \frac{U(\omega)}{I(\omega)} \qquad \text{Equation 2.11}$$

The impedance is a complex quantity with magnitude and phase shift, both of which depend on the frequency of the signal. In electrochemical systems, the frequency typically ranges from 100 kHz to 0.1 Hz. As mentioned earlier, $Z(\omega)$ is a complex quantity and can be expressed in polar coordinates. The impedance can be written as:

$$Z(\omega) = |Z(\omega)| e^{j\emptyset(\omega)} \qquad \text{Equation 2.12}$$

where ω is the magnitude of the impedance at frequency $\emptyset(\omega)$ and ω is the phase shift at frequency ω. In Cartesian coordinates, impedance can be written as:

$$Z(\omega) = Z'(\omega) + jZ''(\omega) \qquad \text{Equation 2.13}$$

where $Z'(\omega)$ is the real component and $Z''(\omega)$ is the imaginary part at frequency ω with $j = \sqrt{-1}$

With these data it is now possible to calculate the complex resistance (also called impedance) which results from Ohm's law (Figure 2.12b):

The graph showing the relationship between the real and imaginary parts of impedance is called a Nyquist plot, as illustrated in Figure 2.12. The advantage of the Nyquist plot is that it provides a quick overview of the data and allows qualitative interpretation. The axes for the real and imaginary parts are kept equal to avoid distorting the shape of the graph, which is crucial for qualitative analysis. However, the downside of the Nyquist plot is that it does not display frequency dimensions. One way to address this issue is by labeling the frequency values directly on the graph. This impedance spectrum is often displayed in a Nyquist diagram (Figure 2.12c) and serves as the basis for evaluation. In the Nyquist diagram, each point represents a specific frequency, with the real and imaginary parts of the complex resistance plotted on the x and y axes, respectively.

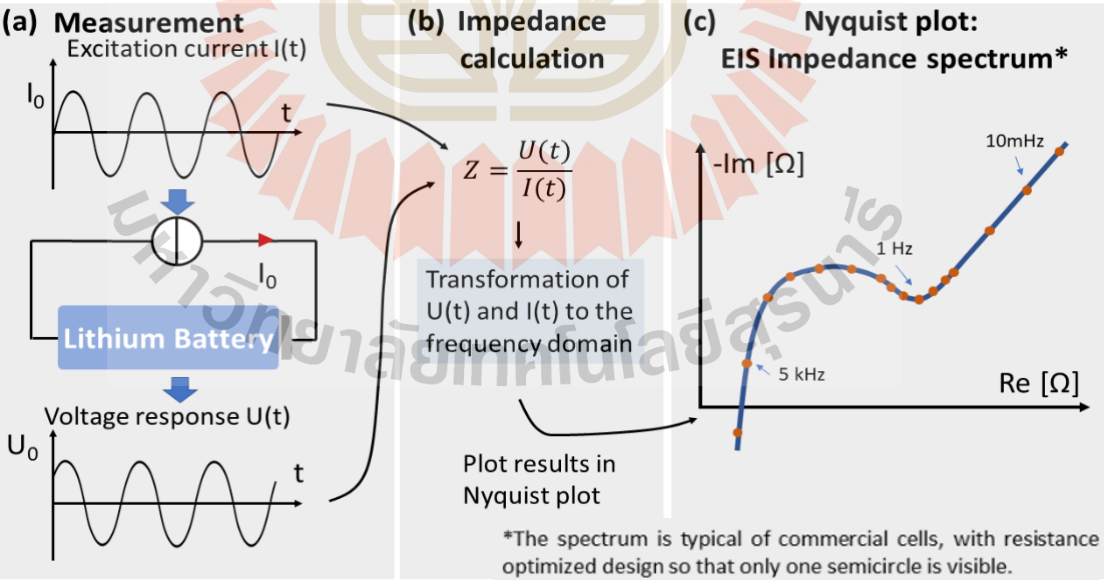

Figure 2.12 Measurement principle for measuring galvanostatic impedance; (b) Conversion of the measured values into impedance; (c) Representation of the measurement results in the Nyquist plot, Own illustration.

2.4.3.2 Electrochemical equivalent circuit

A common method for analysis is the development of an empirical equivalent circuit of the cell, based on the impedance graph, which indicates the internal temperature of the cell. This equivalent circuit typically consists of components such as resistors, capacitors, and possibly inductors. Constructing the equivalent circuit can minimize deviation from the measured impedance spectrum. This approach simplifies the analysis by using various components, as shown in the diagram, which may provide the desired information, such as the structure of the equivalent circuit. A semicircular model is often used in this method, visible on the impedance spectrum, and values can be extracted from the impedance spectrum using simple formulas (as referenced in the work of Choi, W., Shin, H., et al.). Several key parameters can be extracted from EIS measurements:

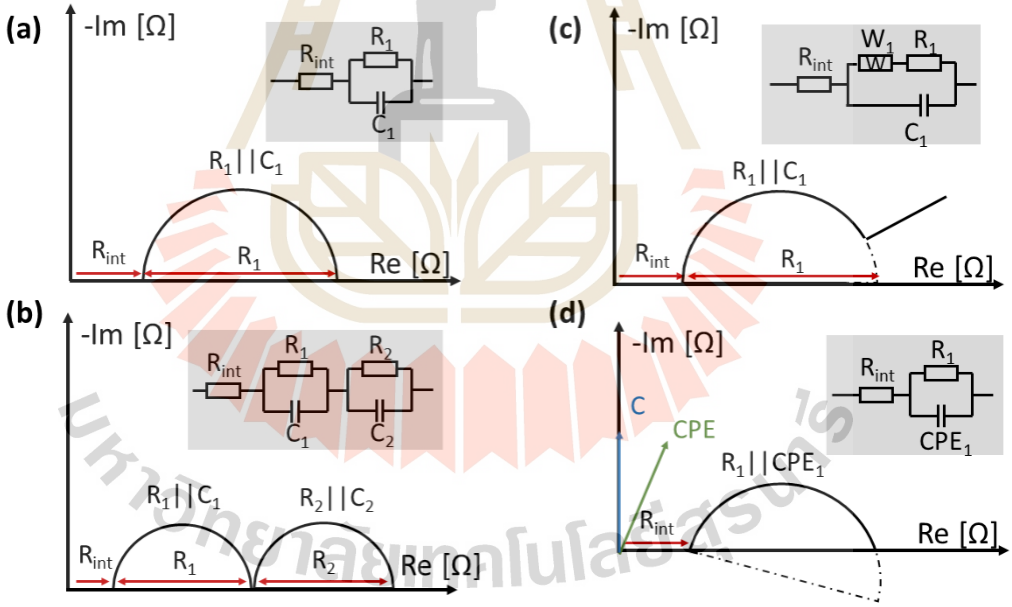

Figure 2.13 The illustration shows different simplified equivalent circuits in the Nyquist diagram: (a) RC components with an additional resistor, (b) a series connection of two RC components and one internal resistor, and (c) an RC component with Warburg impedance and an internal resistor.

- **Solution Resistance (R_s):** Also known as bulk resistance (Rb), this is the resistance of the electrolyte, typically observed at the high-frequency intercept on the real axis of the Nyquist plot.
- **Charge Transfer Resistance (R_{ct}):** This represents the resistance to electrochemical reactions occurring at the electrode surface and often appears as a semicircular arc in the Nyquist plot. Rct increases as the electrode becomes more polarized when the electrode potential is forced to deviate from zero during an open circuit, due to electrochemical reactions, causing current flow at the electrode surface.
- **Constant Phase Element (CPE):** This is an ideal capacitor, assuming the surface properties in the experiment are uniform throughout the system, which is often not the case. Thus, the CPE is used to describe the non-uniform characteristics of the surface.
- **Warburg Impedance (Z_w):** Related to the diffusion of electrochemical species to the electrode surface, it typically appears as a straight line at a 45-degree angle in the low-frequency region of the Nyquist plot. The impedance of some electrochemical cells can result from the adsorption of reactants on the surface, which can be modeled by an inductor. Additionally, inductance may arise from uneven current distribution.

2.4.3.3 Physical models and their evaluation

Figure 2.14 shows the structure of a battery. The anode and cathode each consist of many small grains of active material (for the anode here graphite, for the cathode here LCO) immersed in the liquid electrolyte (For Li-ion batteries). During the discharge process, the lithium moves within a grain at its grain boundary. The lithium deintercalates from the graphite grains and splits into a positively charged lithium ion and an electron. The lithium ion migrates through the porous separator to the cathode with the help of the conducting salt (usually $LiPF_6$). The electron uses conductive soot (carbon black), and migrates via the negative terminal and the connected load to the positive terminal and reaches the cathode this way. At the grain

boundaries of the active cathode particles, the Li-ion and electron react with the cathode. The lithium is then deposited between the cobalt oxide layers.

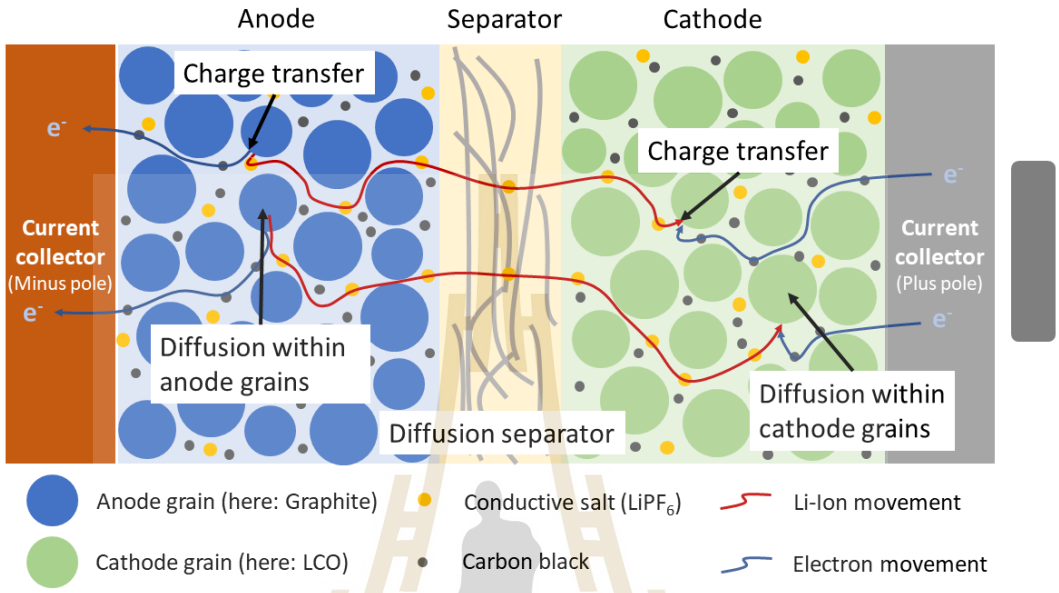

Figure 2.14 The movement of ions and electrons during discharge was examined using a lithium-ion battery with a lithium foil anode and a glassy carbon cathode as an example.

In order to generate an (approximately) correct chemical-physical equivalent circuit of the battery, the individual influence parameters of the chemical discharge process must be modeled in an equivalent circuit. Nevertheless, simplifications are still used here and, for example, the influence of the SEI layer on the surface of the anode is not taken into account. Figure 2.15 shows the equivalent circuit for the anode and the separator for a single reaction path.

A complete electrochemical model is usually too complex to be used to investigate actual processes in the battery. Therefore, a much-used approach is to simplify the model and to summarize or omit parameters that have only a minor influence on the equivalent circuit. A well-known simplification is the De Levie model, which completely neglects the effects of diffusion of ion and anion in separator, anode and cathode. In principle, the model can be further simplified. For example, it may be

possible to completely neglect the ohmic resistances in the anode and cathode. This results in a final equivalent circuit as shown in figure 2.15.

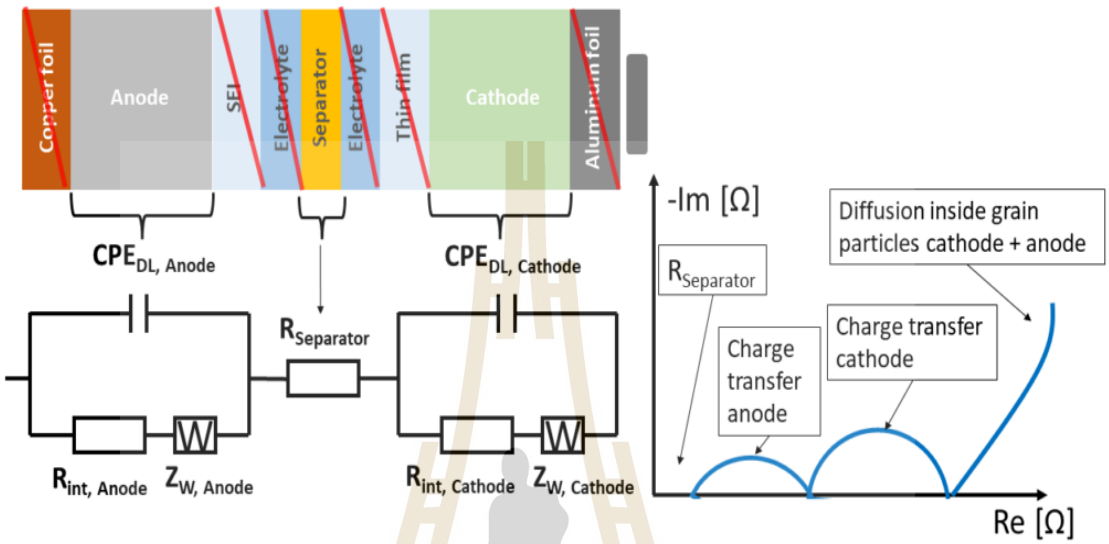

Figure 2.15 Simplified De Levie model of a complete cell. The admissibility of the simplification is not given as a general rule, but must be verified by suitable procedures.

However, the assessment of which parameters of the complete physical equivalent circuit can be neglected is not trivial. It must always be specifically checked in each individual case which simplifications are permissible without distorting the result. For example, if only high frequencies are investigated, ignoring diffusion in the separator, anode and cathode is perfectly justifiable, but for other investigations this adjustment may not be permissible. In other words, the De Levie model may have excellent accuracy in one case and completely fail for another cell in a different set of experiments.

2.4.4 X-ray absorption spectroscopy (XAS)

The inception of x-ray absorption spectroscopy (XAS) dates back over a century, and its progress has been substantial throughout the intervening years. However, because it grew out of a relatively unexplored area of scientific inquiry and was only studied by a small group of dedicated scholars, this methodology was at first seen as a fascinating curiosity that had no practical use and lacked a complete and strong

theoretical framework that could explain and predict experimental observations made on gaseous, liquid, and solid (both crystalline and amorphous) substances. Fourier analysis was used by Sayers, Stern, and Lytle in 1971 to flip the experimental data they got from photoelectron wave-vector space, turning it into a radial distribution function. The initial determination of quantitative values was conducted for bond distance, coordination number, temperature, and disorder features. The field has made significant advancements at an exponential rate over the course of 44 years following the publication of that fundamental work. X-ray absorption spectroscopy (XAS) and its associated methodologies are currently regarded as essential tools for advanced research in a wide range of disciplines, including materials science, solid-state physics and chemistry, catalysis, chemistry, biology, medicine, earth science, environmental studies, cultural heritage preservation, and nanoscience, among others. This introduction chapter provides a comprehensive summary of the key advancements that have contributed to the extensive utilization of XAS and its associated techniques for scientific characterization.

2.4.4.1 Principle of XAS

The core principles underlying X-ray absorption spectroscopy can be succinctly elucidated within a concise statement. When a sample is exposed to an X-ray photon of sufficient energy, it has the potential to ignite a core electron within the material. The energy levels of the core electrons remain largely unaltered by the chemical environment in which they reside due to their occupation of confined states. The selectivity of X-ray absorption spectroscopy (XAS) can be attributed to this particular component. The phrase "absorption edge" denotes the specific energy threshold at which a sudden and significant alteration occurs in the absorption coefficient. This particular aspect is indicative of the binding energy associated with the core level. The absorption edges, often referred to as sudden rises in absorption, correlate to the energy required for the ejection of a core electron into the lowest unoccupied molecular orbital (LUMO) or into the continuum, resulting in the creation of a photoelectron. The absorption discontinuity associated with the photoelectron originating from a 1s core level is commonly known as the K-edge. Conversely, the term "L-edge" is employed to denote the ionization event resulting from the excitation

or removal of a 2s or 2p electron. According to the data shown in Figure 2.16, the electron in an excited state possesses the capability to transition to either unoccupied bound levels or continuous unbound levels.

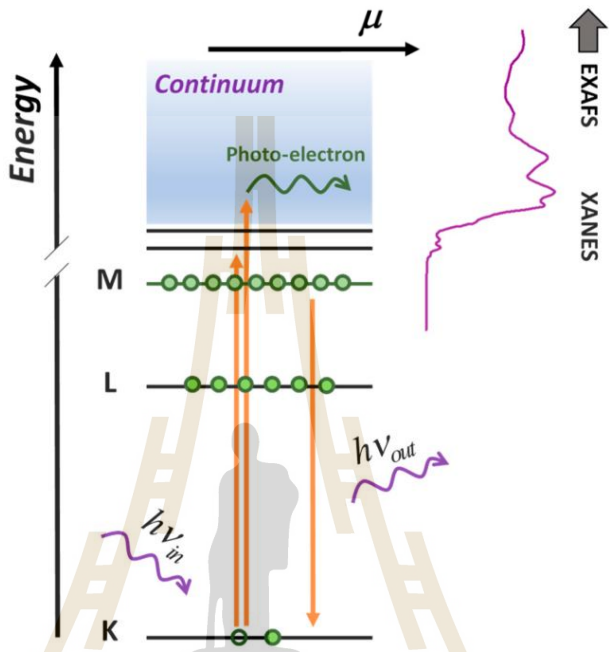

Figure 2.16 Scheme of the X-ray absorption process (Fracchia, Ghigna, Vertova, Rondinini, and Minguzzi, 2018).

The atoms in its vicinity can then scatter it back, a process known as back-diffusion. The interatomic distance determines whether the emitted electron and the back-scattered waves have a destructive or constructive interaction for a given photon energy. The result of this effect is a fluctuation in the X-ray absorption coefficient that can be measured hundreds of electron volts (eV) above the absorption edge. This allows one to determine the local structure (number, nature, and distance of surrounding atoms) in the area immediately surrounding the photo absorber; this is known as the "Extended X-ray Absorption Fine Structure" (EXAFS). Specifically, the absorption coefficient strongly modulates at energies near the boundary. In this case, the electronic transitions to bound unoccupied states and/or multiple scattering events are responsible for the X-ray absorption near edge structure (XANES). Significant data on the surrounding coordination environment can be gleaned from XANES (type

of coordination and its distortions). In conclusion, the oxidation state is reflected in the fine energy at which the absorption edge falls, which is directly proportional to the electron density on the photo absorber. Therefore, XAS provides a reliable, objective measure of atomic oxidation states in compounds.

- **X-ray absorption near edge structure (XANES)**

X-ray absorption near-edge structure (XANES) spectra reveal the oxidation state and coordination environment of metal atoms with great specificity (Figure 2.17a). In general, higher oxidation states have higher K-edge absorption edge energies. The position of the incrementing changes as a result of 1s core hole shielding effects on the effective number of positive charges (or, in a simplified view, the oxidation state). As an example, in a single-electron atom, the electron feels the full charge of the positive nucleus. On the other hand, in a highly charged atom, the outer electrons are repelled by the negatively charged electrons and attracted to the positively charged nucleus. It takes more energy to excite an electron from an orbital when the metal's oxidation state is higher because a higher oxidation state results in a more positively charged atom. When a negative charge is applied to a metal, however, the X-ray energy spectrum changes to a lower level.

Transitions from 1s to np, where np is the lowest occupied p orbital of the absorbing atom, are the primary contributors to the K-edge spectrum. This transition, with l = 1 (where l is the quantum number of the orbital momentum), is permitted by quantum mechanics and is typically strong. Pre-edge features resulting from 1s to (n-1) d transitions provide additional insight for transition metals with partially occupied d orbitals. These have a low intensity (l = 2, so they are formally forbidden or dipole-forbidden), but they are detectable because they occur at energies just below the main absorption edge. When the ligand environment is broken from octahedral symmetry, the intensity of the pre-edge peak rises (Yano and Yachandra, 2009).

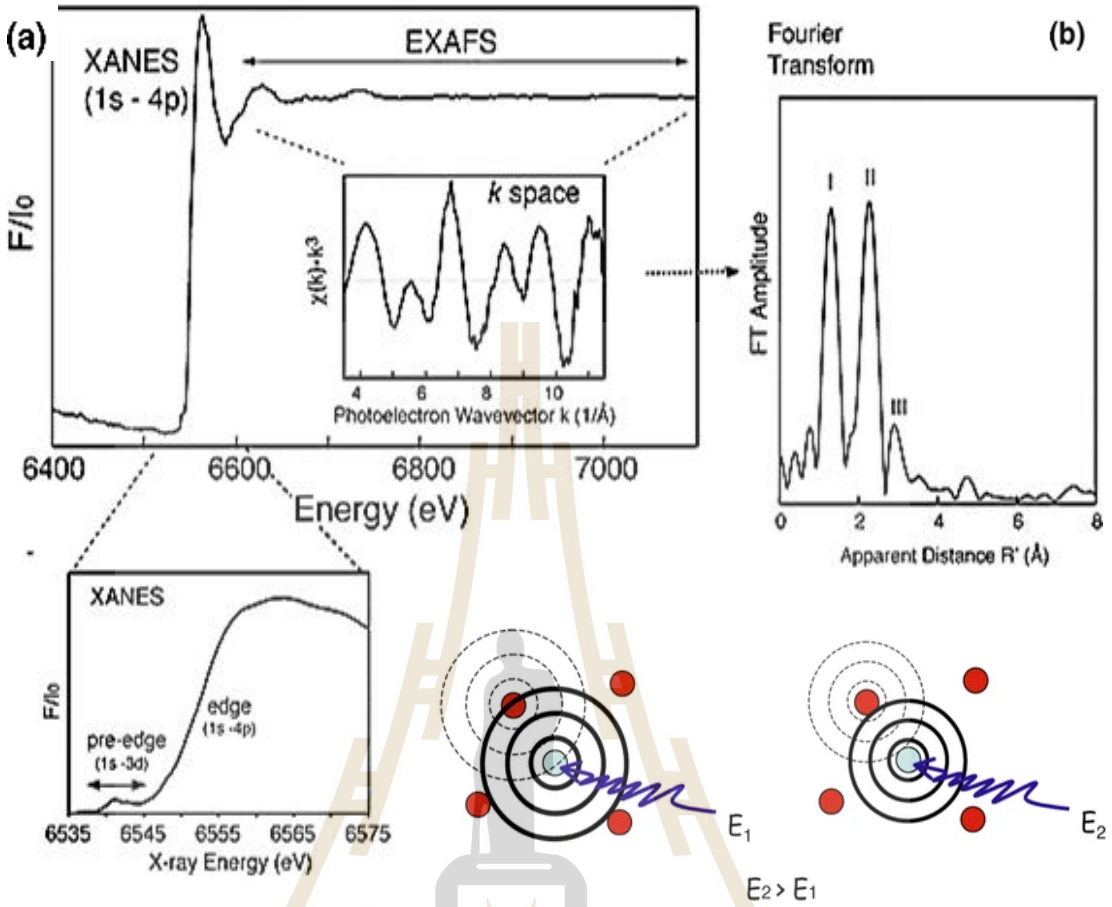

Figure 2.17 a) XANES and EXAFS spectra of the manganese K edge. Upper left: XANES and EXAFS regions of the X-ray absorption spectrum of a PS II sample, b) A diagram showing the propagating and reflected photoelectron wave, which represents interference in EXAFS (Yano and Yachandra, 2009).

- **Extended fine structure (EXAFS)**

Detailed information about the partial pair distribution functions of the atoms surrounding the absorber, such as distances, mean square deviations in distance, coordination numbers, and coordinating species, can be obtained through analysis of the extended x-ray absorption fine structure (EXAFS). EXAFS can be applied to any type of condensed matter, as its theory and interpretation do not rely on any assumptions of configurational symmetry or periodicity. EXAFS can be used on diluted systems because the fundamental physical process of x-ray absorption spectroscopy (XAS), the photo-excitation of a deep-core electron, is element specific. Thus, EXAFS

plays an important role in a wide range of scientific fields, including the study of life, the environment, chemistry, materials science, cultural heritage, and more. In a nutshell, EXAFS is a vital skill for any synchrotron radiation lab.

In XAS spectrum, the difference between XANES and EXAFS can be thought of as a difference in regime. One of the limitations of this definition is that there is no single, overarching principle that distinguishes the two systems in question, even though they appear to share the same conceptual principles. Most people place XANES at an energy level where the potential is 50 eV above the edge, while they place EXAFS at an energy level where the potential is between 50 and 1000 eV above the edge (Yano and Yachandra, 2009).

In the context of EXAFS (Extended X-ray Absorption Fine Structure), k-space and R-space are two crucial domains used for data analysis.

1. k-space: This is the energy domain used to analyze the variations in X-ray absorption due to the excited electrons ejected from an atom. In EXAFS, k represents the wave vector of the excited electrons, measured in Ångström^{-1} (Å^{-1}). Analyzing data in k-space involves studying the interference patterns of these outgoing and backscattered electron waves, which helps identify the scattering processes and energy changes.

2. R-space: This is the distance domain used to analyze the distribution of atoms around the central atom. In EXAFS, R represents the radial distance between the central atom and its neighboring atoms, measured in Ångström (Å). Data in R-space is obtained through Fourier transform of the k-space data, allowing determination of interatomic distances, coordination numbers, and the atomic distribution within the structure.

2.5 Thesis motivation

In this section, the research's origins will be addressed, drawing inspiration from two research studies. This has led to questions, challenges that arise, and problems that need to be solved based on the above research.

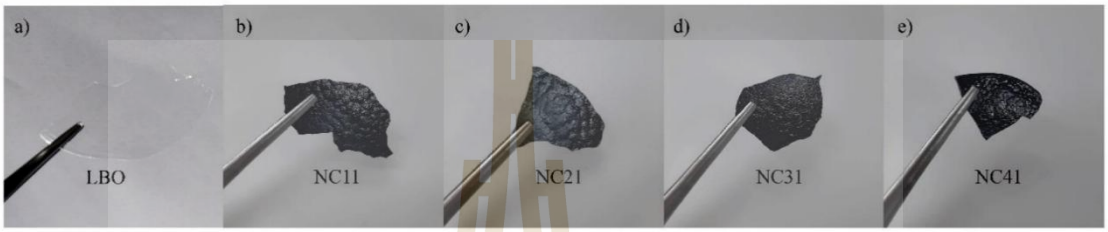

Figure 2.18 The plate glasses of a) LBO glass and b) - e) Ni/Co doped LBO, with the Ni:Co ratios being 1:1, 2:1, 3:1, and 4:1, respectively (Siriroj et al., 2023).

Due to the previous study titled "New glass cathode materials for Li-ion battery: Ni-Co doping in Li-B-O based glass" (Siriroj et al., 2023) which involved incorporating Ni-Co doping into LBO at a ratio of 0.2 (Ni-Co) to 0.8 LBO and varying the Ni and Co concentrations. Figure 2.18 shows the physiological characteristics of the glass plate sample. In electrochemical testing of glass cathodes, the glass cathode with a high cobalt (Co) content (NC11 which uses a Ni-CO ratio of 1:1) initially exhibited the highest specific capacity (380 mAh/g) during its first discharge cycle (Figure 2.19a).

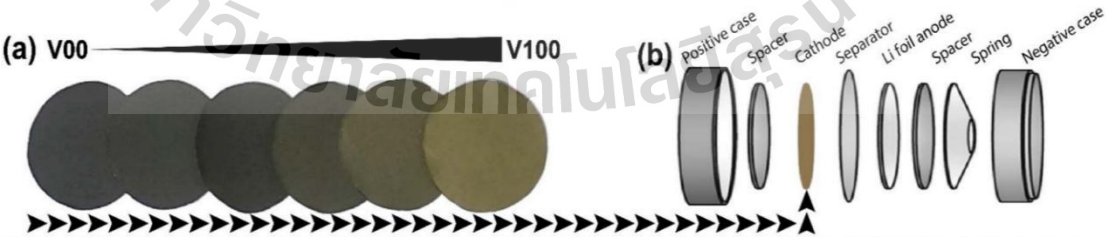

Figure 2.19 This figure show (a) The photograph of film composition of V_2O_5 from black color (0%) to yellowish-brown color (100%). (b) The coin cell assembly components (Siriroj et al., 2022).

However, in subsequent cycles, there was a significant decrease in capacity due to the entrapment of lithium ions in the glassy structure. Conversely, glass cathodes with a higher concentration of nickel ions in the co-doped Ni/Co-LBO glass (NC41 which uses a Ni-CO ratio of 4:1) displayed improved long-term retention properties (Figure 2.20a), indicating that a nickel-rich composition might facilitate the release of free lithium ions from the host glass structure (Siriroj et al., 2023).

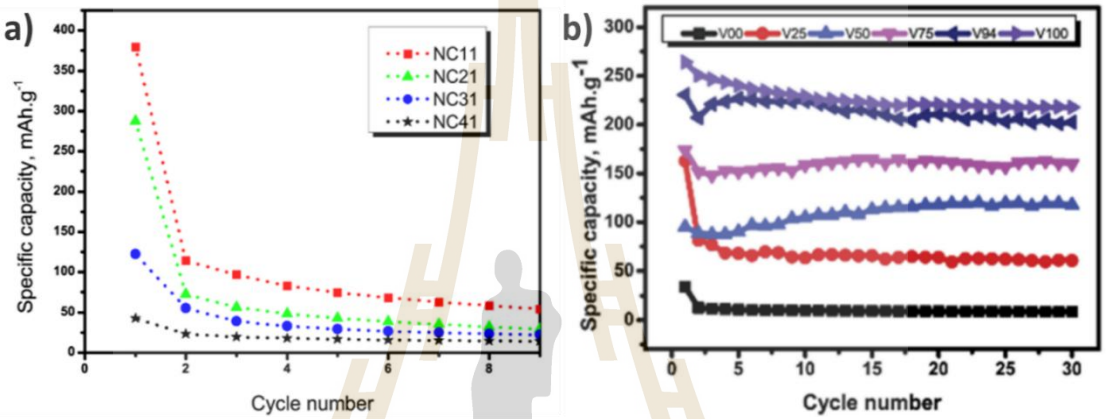

Figure 2.20 Shows specific capacitance value compared to test cycles of a) NC11, NC21, NC31 and NC41 (Siriroj et al., 2023). b) V00, V25, V50, V75, V94 and V100 (Siriroj et al., 2023; Siriroj et al., 2022).

For the reasons mentioned above, in the subsequent research on the topic "Enhancement of V_2O_5 Li-ion cathode stability by Ni/Co-doped Li-borate-based glass" the sample with the most stable capacitance value was selected. NC41 (25%) was incorporated into V_2O_5 (75%) and mixed for 24 hours, aiming to enhance the capacity to a higher level. Using symbols such as V00 to represent the absence of V_2O_5 (0%), and V100 to denote the presence of V_2O_5 at 100%. The cell was assembled using the coin cell technique. Figure 2.19a the cathode was constructed using a V_2O_5 mixed Ni/Co glass-based Li-borate film on an Al foil, featuring various compositional conditions, with a PP separator film (Celgard 2400) dividing it (Kayyar, Huang, Samiee, and Luo, 2012), while the anode consisted of Li foil. Afterward, it was infused with 50 microliters of 1 M $LiPF_6$ in an ethylene carbonate (EC): dimethyl carbonate (DMC) (1:1) electrolyte solution. Subsequently, the coin cell was sealed by utilizing an ECCCM-160E-A crimping

machine from MTI Corporation with a 1-ton push. In Figure 2.19b shows an overview of the components of a coin cell construction. The battery test results show that adding glass can change the voltage-capacity curve from pure V_2O_5 stairway form to a straighter line (Figure 2.20b).

Therefore, this work has piqued an interest in the glass-making process that is easy to make and produces the most efficient results through the traditional melt quenching method, drawing inspiration from two previous studies (Siriroj et al., 2023; Siriroj et al., 2022).

This study consisted of four distinct processes. In the initial process, Ni-Co and LBO were used, and this was followed by the glass melt quenching method, which was consistent with the methodology employed in a prior study (referenced as research (Siriroj et al., 2023)). The second process commenced by mixing the products of the first process with V_2O_5 before proceeding to the glass melt quenching method. In the third process, LBO, Ni, Co, and V_2O_5 were all combined and subjected to the glass melt quenching method simultaneously. The final process involved combining glass from the first process with V_2O_5 and mixing them for 24 hours to complete the procedure, mirroring the approach taken in another previous study (referred to as research (Siriroj et al., 2022)).

2.6 Sope and limitation

In this study, the scope and limitations revolve around materials, instrumentation, and research locations. Material selection is based on availability and alignment with research goals, while instrumentation is restricted by budget and technical constraints.

2.6.1 Materials

In this work, for the preparation of the glass base, we use Lithium carbonate (Li_2CO_3) with a purity of 99.5% and Boric acid (H_3BO_3) with a purity of 99.8%. Additionally, in the chemical doping part of this project, we employ other chemicals sourced from Himedia, including Nickel oxide (NiO) with a purity of 97.0%, Vanadium(V) oxide (V_2O_5) with a purity of 99.6%, and Coalt (II, III) oxide (Co_3O_4) with a purity of 70.0%.

2.6.2 Instrumentation and Research locations

In this research project, we operated under the guidance and assistance of the Battery and Energy Material Research Laboratory (Glass Novel Battery), which is a part of the Synchrotron Light Research Institute (a public organization). This study also involves the examination of sample materials using X-ray diffraction (XRD) techniques, overseen by the Science and Technology Instrumentation Center at Suranaree University of Technology.

CHAPTER III

EXPERIMENTAL

3.1 Research procedure

The research process involves five steps, starting with base glass preparation, followed by sample preparation, which includes four processes yielding eight samples. The final step focuses on characterizing these samples to evaluate their structural properties. The workflow is shown in Figure 3.1.

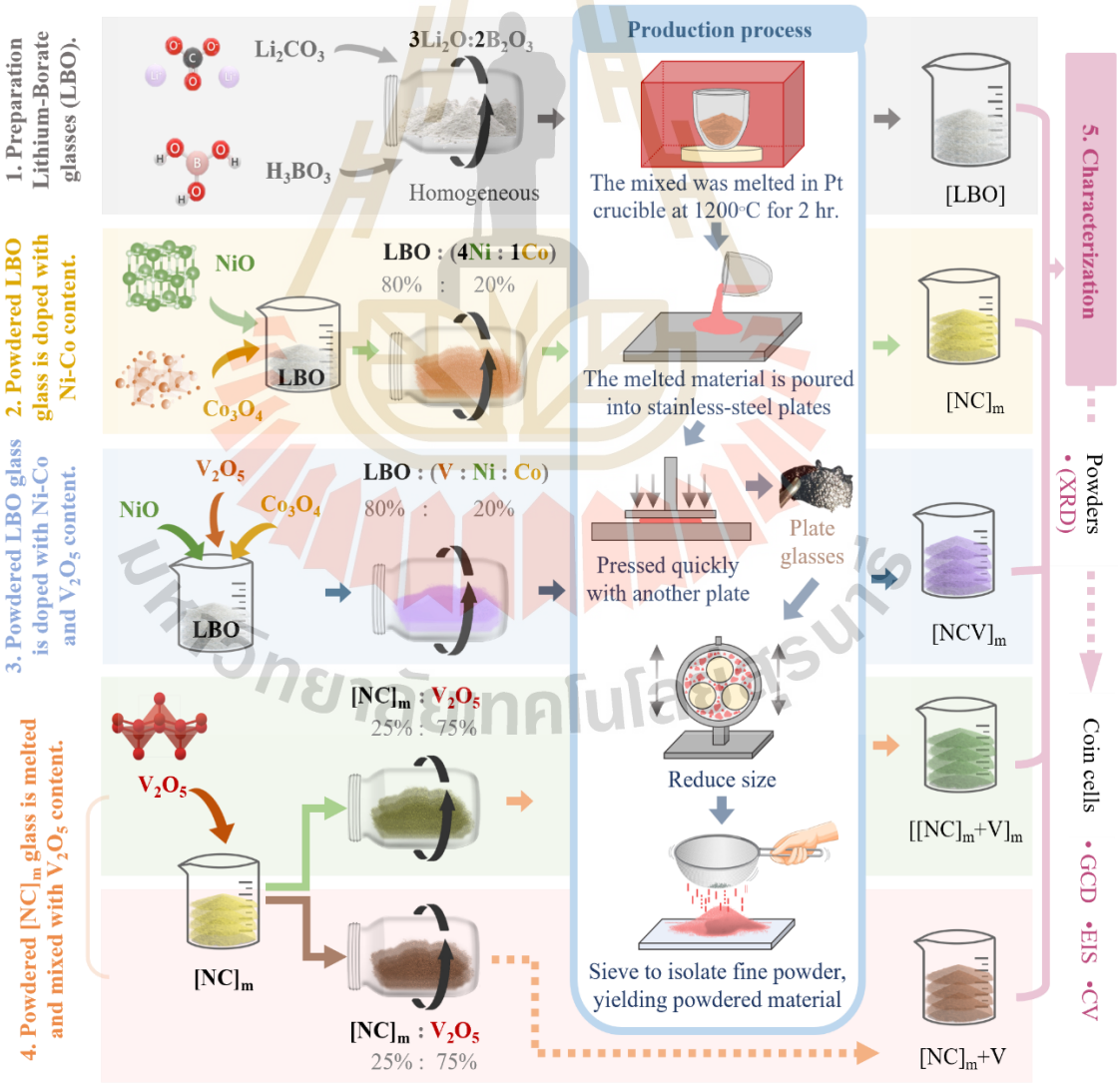

Figure 3.1 Overview of the Research Workflow.

3.2 Sample Preparation

To prepare all the samples, the process is divided into two official steps. The first step involves the preparation of Lithium-Borate glasses (LBO), and the subsequent step entails doping with substances such as Ni, Co, and V_2O_5. In this work, the formula for preparing the glass samples is given as follows:

Chemical system $LiBO_3$: NiO + Co_3O_4 + V_2O_5 with fixed $LiBO_3$ and V_2O_5 content but varied NiO and Co_3O_4 content.

- Sample 1) 0.800LBO: 0.100NiO-0.100Co_3O_4 or $[NC11]_m$
- Sample 2) 0.800LBO: 0.160NiO-0.040Co_3O_4 or $[NC41]_m$
- Sample 3) 0.250$[NC11]_m$-0.750V_2O_5: Mix or $[NC11]_m$ +V
- Sample 4) 0.250$[NC41]_m$ - 0.750V_2O_5: Mix or $[NC41]_m$ +V
- Sample 5) 0.250$[NC11]_m$ - 0.750V_2O_5: Melt or $[[NC11]_m$ +V$]_m$
- Sample 6) 0.250$[NC41]_m$ - 0.750V_2O_5: Melt or $[[NC41]_m$ +V$]_m$
- Sample 7) 0.200LBO- 0.025NiO-0.025Co_3O_4-0.750V_2O_5 or $[NC11+V]_m$
- Sample 8) 0.200LBO- 0.040NiO-0.010Co_3O_4-0.750V_2O_5 or $[NC41+V]_m$

3.2.1 Preparation LBO glasses

Glass-based of $LiBO_3$, generally called LBO is obtained by burning and $2H_3BO_3$ together, leading to the precipitation reaction with the following chemical formulas:

$$Li_2CO_3 \longrightarrow Li_2O + CO_2 \qquad \text{Equation 3.1}$$

$$H_3BO_3 \longrightarrow B_2O_3 + 3H_2O \qquad \text{Equation 3.2}$$

The products of this chemical reaction, when mixed with each other (Equation 3.1 and 3.2), are H_2O and CO_2, which are completely evaporated by heat, leaving only Li_2O and B_2O_3 as precipitation reactions, and the resulting product is $LiBO_3$ (LBO). In this work, the ratio between Li_2O and B_2O_3 of 1:2 was used. Its total molecular mass is 99.464 g/mol. 20 g of LBO was required, so 14.8521 g of Li_2CO_3 and 49.7101 g of H_3BO_3 are needed (Figure 3.2a). The powders of Li_2CO_3 (99.5% purity, Himedia) and H_3BO_3 (99.8% purity, Himedia) were finely powdered and mixed by ball milling for 24 hours (Figure 3.2b). After mixing, it was put in a platinum (Pt) crucible using an electric furnace

at 1100°C for 120 min (Figure 3.2b-c). by heating was fixed at 10°C/min. Each melt was splat-quenched between stainless-steel plates and pressed quickly with another plate at room temperature (RT) (Figure 3.2d-e). This will yield a glass LBO plate as depicted in Figure 3.2f. After that, they were mixed and ground thoroughly using a Mini Mill Pulverisette 23 at a frequency of 30 Hz for 10 min using a Grinding Bowl zirconium oxide and Grinding Balls zirconium oxide 10 mm (3 pcs) (Figure 3.2g). By sieving to filter out only the fine powder, the resulting material is in powdered form (Figure 3.2h-i).

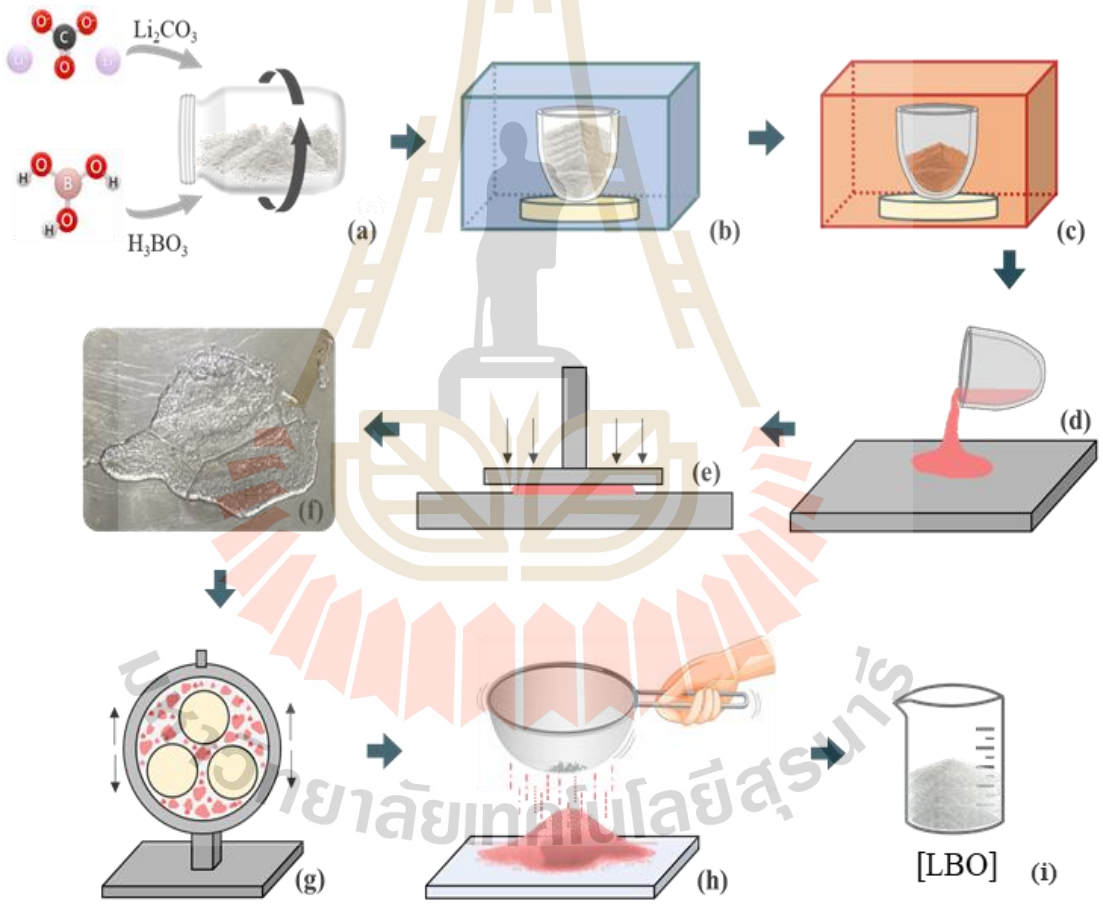

Figure 3.2 Shows the process of preparing LBO glasses.

3.2.2 Preparation of Li-borate base glass mixed with NiO, Co_3O_4, and V_2O_5

Moving on to the next section, we will provide a detailed exposition on the sample preparation process for the eight samples. This comprehensive exploration will delve into the intricacies of each preparation step, offering a more in-depth understanding of the procedures involved.

3.2.2.1 Samples of $[NC11]_m$ and $[NC41]_m$

Preparation Ni, Co and V_2O_5 doped Li-borate base glass electrode. Table 3.1 shows chemical composition ratios in of samples $[NC11]_m$ and $[NC41]_m$, which contain lithium borate glass with nickel (II) oxide and cobalt (III) oxide (LBO: NiO: C_3O_4). The preparation method involves using 80% LBO and the remaining 20% consists of Ni and Co. In the case of $[NC11]_m$, the Ni:Co ratio is 1:1, while for $[NC41]_m$, it is 4:1. Each sample is prepared with a total mass of 10 grams. Subsequently, they are mixed together and subjected to a Melt-quenching and size reduction process, as shown in figure 3.1 (Production process). After completion of the process, glass plates are obtained, as seen in figure 3.1 for samples $[NC11]_m$ and $[NC41]_m$ are (a) and (d), respectively. Finally, the resulting material is sieved to isolate the fine powder.

Table 3.1 Illustrates the ratio conditions of the $[NC11]_m$ and $[NC41]_m$ formulas for a total of 10 g of prepared samples.

Sample	%LBO	%NiO	%Co_3O_4	$MW._{all}$ (g/mol)	Preparation of glass compounds (g)		
					LBO	NiO	Co_3O_4
$[NC11]_m$	80.0	10.0	10.0	101.15	7.1611	0.6721	2.1667
$[NC41]_m$	80.0	16.0	4.0	111.12	7.8666	1.1813	0.9521

3.2.2.2 Samples of $[NC11+V]_m$ and $[NC41+V]_m$

Examples of $[NC11+V]_m$ and $[NC41+V]_m$ involve the co-melting of NiO, Co_3O_4, V_2O_5 and LBO. The chemical composition ratios for these components are

presented in Table 3.2. The preparation method utilizes 80% lithium borate (LBO) with the remaining 20% consisting of Ni, Co, and V_2O_5. However, there is a difference between the two examples in terms of the Ni:Co ratio. For $[NC11+V]_m$, the ratio is 1:1, whereas for $[NC41+V]_m$, it is 4:1. Each sample is prepared with a total mass of 10 grams. After preparing the substances according to their respective weights, they were mixed together for 24 hours. Subsequently, they were introduced into the process outlined in figure 3.1 (Production process). After the glass melting process, it was poured into stainless steel sheets, glass plate is obtained as shown in figure 3.1 c and f for samples $[NC11+V]_m$ and $[NC41+V]_m$, respectively. In the final step, we obtain powdered material.

Table 3.2 Show the ratio conditions for the $[NC11+V]_m$ and $[NC41+V]_m$ formulations.

Sample	% LBO	% NiO	% Co_3O_4	% V_2O_5	Preparation of glass compounds (g)			
					LBO	NiO	Co_3O_4	V_2O_5
$[NC11+V]_m$	20.0	2.5	2.5	75.0	1.2118	0.1137	0.3667	8.3078
$[NC41+V]_m$	20.0	4.0	1.0	75.0	1.2305	0.1848	0.1489	8.4358

Table 3.3 Illustrates the ratio conditions of the $[NC11]_m$ +V, $[NC41]_m$ +V, $[NC11]_m$ +$V]_m$, and $[NC41]_m$ +$V]_m$ formulas for a total of 10 g of prepared samples.

Sample	% $[NC11]_m$	% $[NC41]_m$	% V_2O_5	MW.$_{all}$ (g/mol)	Preparation of glass compounds (g)		
					$[NC11]_m$	$[NC41]_m$	V_2O_5
$[NC11]_m$ +V $[NC11]_m+V]_m$	25.0	-	75.0	164.15	1.6922	-	8.3078
$[NC41]_m$ +V $[NC41]_m+V]_m$	-	25.0	75.0	161.66	-	1.5642	8.4358

3.2.2.3 Samples of $[NC11]_m$ +V and $[NC41]_m$ +V

For the remaining four samples, their chemical compositions are presented in table 3.3. Notably, the Mix and Melt samples share the same chemical composition, which consists of a mixture of nickel cobalt glass doped with vanadium pentoxide (GNC: V_2O_5) in a 25:75 ratio. The key difference lies in the glass fabrication process. In the case of the 'Mix' samples, it involves blending Glass Nickel Cobalt (GNC) with V_2O_5 for a duration of 24 hours to complete the process. The outcome is a powdered form of the samples denoted as $[NC11]_m$ +V and $[NC41]_m$ +V, as illustrated in figure 3.1.

3.2.2.4 Samples of $[[NC11]_m +V]_m$ and $[[NC41]_m +V]_m$

In the case of the Melt sample, after achieving a homogeneous mixture ($[[NC11]_m+V]_m$ and $[[NC41]_m +V]_m$), it is subjected to the glass melting process (as shown in figure 3.1, Production Process). This process results in glass plates, depicted in figure 3.1 b and e. Once completed, the process results in the production of powders denoted as $[[NC11]_m+V]_m$ and $[[NC41]_m +V]_m$, respectively.

3.3 Manufacturing of Li-ion battery coin cells

The cell was assembled using the coin cell technique figure 3.3 shows an overview of the components of a coin cell construction.

3.3.1 Preparation of Cathode

- In this work, carbon black (CB) was used as a conductive material, and polyvinylidene fluoride (PVDF) was used as a binder to help adhere the material to both the CB and the foil. The ratio used was 8 : 1 : 1 (glass powder: CB: PVDF), which was prepared by mixing 1.2 ml of 2.5% PVDF solution, 0.03 g of CB, and 0.24 g of glass powder, as shown in Figures 3.3a-b. The three components were combined using two 2 mm grinding balls and one 5 mm ball to ensure better homogeneity.
- The mixture was then shaken for 30 minutes (Figure 3.3c). Afterward, the grinding balls were removed, leaving only the well-mixed sample.

- A layer of PVDF was evenly applied to the glass base, followed by placing aluminum foil on top. Another layer of PVDF was used, and the foil was smoothed to ensure full contact. The Doctor Blade Coating Device was adjusted to a thickness of 20 µm, and the device was placed on the aluminum foil. The prepared sample mixture was poured onto the foil and then coated to form a uniform layer, as shown in Figures 3.3d-e.
- The coated sheet was dried in an oven at 80°C for 1 hour to prevent cracking and ensure proper drying. The section of the aluminum foil with the sample was pressed using a force of approximately 1 ton Figure 3.3f.

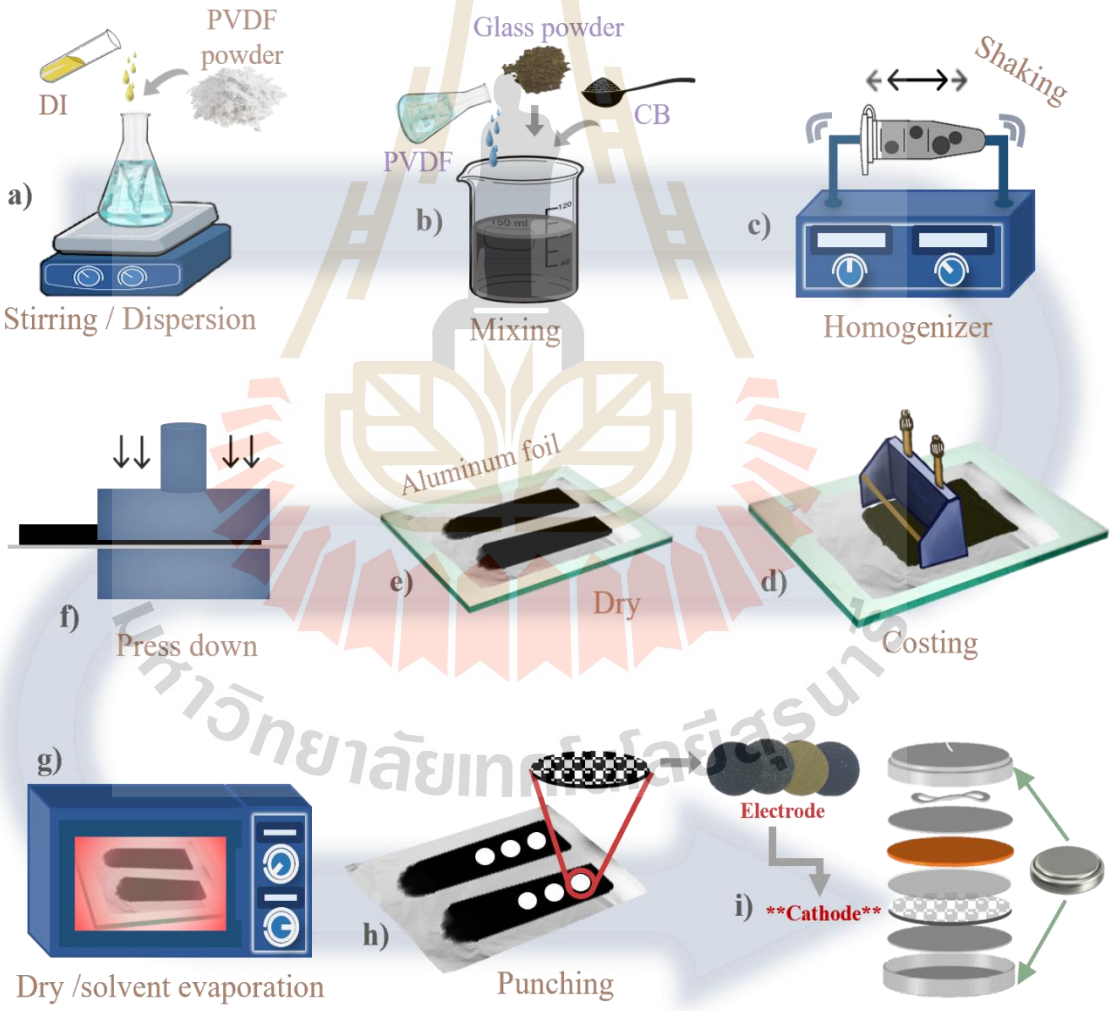

Figure 3.3 Schematic representation of the stages in cathode preparation, from material selection to assembly.

- The pressed sheet was then baked again at 120°C for 1 hour to completely remove any moisture (Figure 3.3g).
- Finally, the sheet was cut into 16 mm diameter circles, as shown in Figure 3.4b.

3.3.2 Coin Cell Assembly

In Figure 3.4, the cathode was constructed using a V_2O_5 mixed Ni/Co glass-based Li-borate film on an Al foil, featuring various compositional conditions, with a PP separator film (Celgard 2400) dividing it (Kayyar, Huang, Samiee, and Luo, 2012), while the anode consisted of Li foil. Afterward, it was infused with 50 microliters of 1 M $LiPF_6$ in an ethylene carbonate (EC): dimethyl carbonate (DMC) (1:1) electrolyte solution. Subsequently, the coin cell was sealed by utilizing an ECCCM-160E-A crimping machine from MTI Corporation with a 1-ton push.

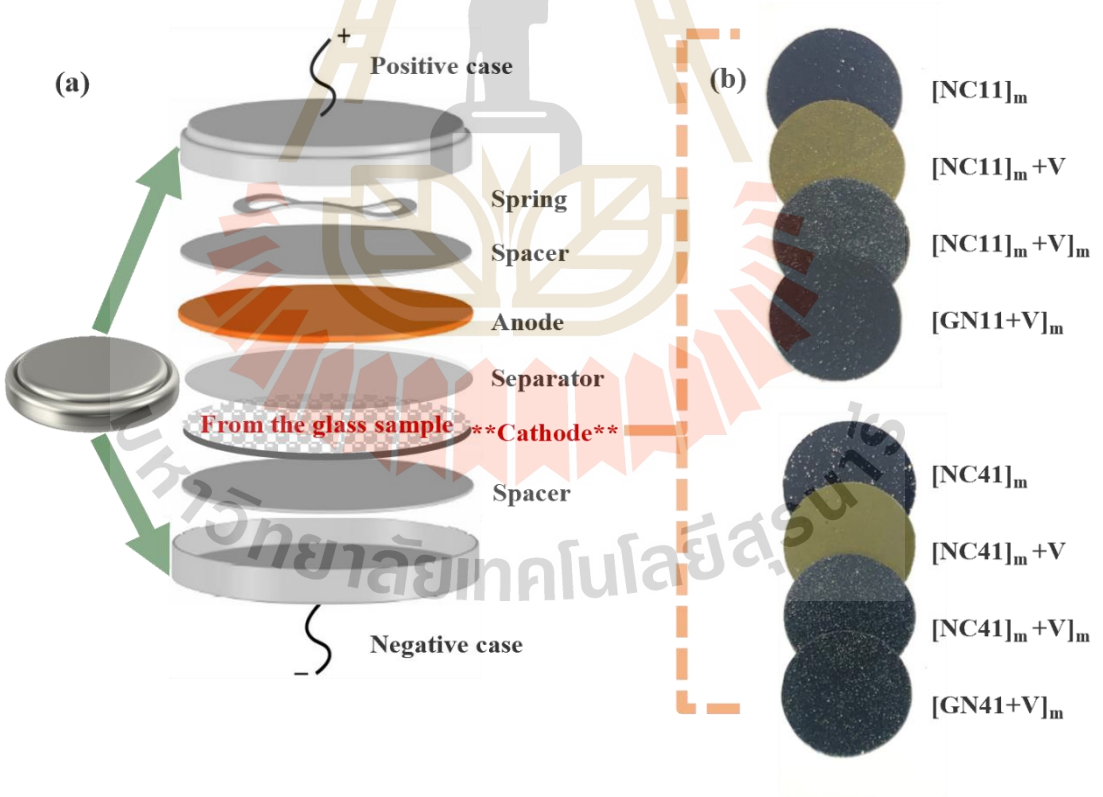

Figure 3.4 This figure show (a) The coin cell assembly components. (b) The photograph of film composition of $[NC11]_m$, $[NC11]_m$ +V, $[NC11]_m$ +V]$_m$, $[NC11+V]_m$, $[NC41]_m$, $[NC41]_m$ +V, $[NC41]_m$ +V]$_m$ and $[NC41+V]_m$.

3.4 Instrumentation

3.4.1 Powder X-ray Diffraction Analysis using Bruker D8 Advance

Figure 3.5 Bruker D8 X-ray diffractometer (XRD) was used for the analysis.

In this work, we utilized the Bruker D8 Advance Powder X-ray Diffractometer (XRD). This system is equipped with a high-performance PhotonMax 9 kW rotating anode X-ray source and a HyPix-3000 multidimensional semiconductor detector with high-energy resolution. The HyPix-3000 detector supports 0D, 1D, and 2D measurement modes, allowing for versatile applications without the need to switch detectors for different tasks. With this detector, 2D powder diffraction patterns can be obtained. Additionally, the system features an in-plane diffraction arm and a high-resolution, closed-loop goniometer drive mechanism. The Cross-Beam Optics (CBO) system, featuring fully automated switchable optics (CBO-Auto), enables both reflection and transmission modes with ease.

3.4.2 Neware Battery Testing Systems

The Neware Battery Testing Systems BTS4000-5V10mA and 5V50mA are essential tools for measuring battery capacity and analyzing electrochemical performance. These systems are designed to evaluate the charge and discharge behavior of batteries, providing crucial insights into their electrochemical properties.

The BTS4000 series supports precision testing at both low and moderate current ranges, with the 5V10mA model suitable for small-scale battery cells and the 5V50mA model ideal for larger cells. These systems allow for accurate tracking of voltage, current, and capacity over time, which is critical for determining battery efficiency, energy density, and stability.

Figure 3.6 Battery Capacity Measurement using Neware BTS4000-5V10mA5V50mA Systems.

Through the charge and discharge curves generated during testing, users can assess the battery's performance under various conditions, including cycle life and capacity retention. The versatility of the Neware BTS4000 systems makes them widely used in research and development of new battery materials, including lithium-ion, solid-state, and other advanced energy storage technologies.

3.4.3 Potentiostat galvanostat analysis using metrohm autolab

The Biologic SP300 Potentiostat/Galvanostat is a versatile and high-performance electrochemical workstation designed for a wide range of electrochemical measurements, including cyclic voltammetry (CV), electrochemical impedance spectroscopy (EIS), and charge-discharge studies. In this research, the Biologic SP300 was used to evaluate the electrochemical properties of battery electrodes.

For EIS measurements, the SP300 was employed to determine the impedance values of the battery electrodes, providing insights into the electrode's charge transfer

resistance and electrolyte resistance. This analysis helps in understanding the behavior of the electrode material and the efficiency of ion transport in the system. Additionally, cyclic voltammetry (CV) was used to measure the specific capacitance of the glass electrodes. By applying a varying voltage and recording the resulting current, the CV data from the SP300 provided information on the charge storage capability and redox activity of the electrode material.

Figure 3.7 Potentiostat Galvanostat Analysis using Metrohm (Biologic) SP300.

The SP300 features a high-frequency response and wide dynamic range, making it ideal for precision electrochemical measurements, ensuring reliable data for the characterization and development of advanced battery materials.

3.4.4 SUT-NANOTEC-SLRI XAS beamline at SLRI

X-ray absorption spectroscopy (XAS) is the only focus of the SUT-NANOTEC-BL5.2 SLRI beamline. Chemical speciation and local structure (number of coordination complexes, inter-atomic distance, etc.) can both be determined with this method. X-ray absorption spectroscopy (XAS) is a non-destructive technique that can be applied to any solid (crystalline or amorphous), liquid, or gas (pressure and temperature control) outside of ambient conditions. Real-world samples from fields as varied as materials science, biology, environmental science, archaeology, and geology can all be studied with this method. To detect and quantify S species in difficult materials such as minerals, coals, sediments, and rubber, X-ray Absorption Near Edge Structure (XANES) spectroscopy is an excellent, non-destructive option. Materials in this category include minerals, coals, sediments, and even rubber. Differences in the S-K apex and XANES bands can oxidize sulfur compounds in either an inorganic or organic form. Like fingerprints, XANES bands can provide insight about a substance's coordination

chemistry. The fundamental idea of both BL5.2 and BL8 is the same. It relies heavily on an in-house-built double-crystal monochromator (DCM) with a fixed outlet. To adjust the level of x-ray radiation, a DCM equipped with a wide range of crystals, from 1240 eV to 12100 eV, is employed. All the way from magnesium to gallium, you can do K-edge absorption tests. The L and M limits are useful for studying heavier atomic species.

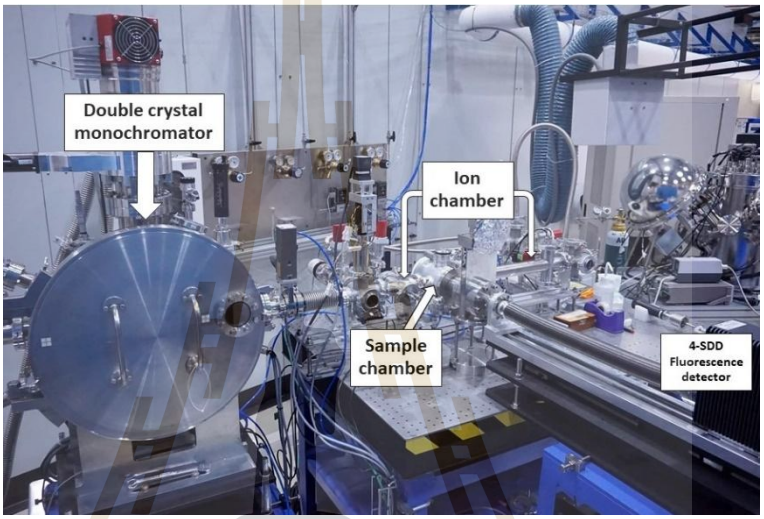

Figure 3.8 BL5.2: SUT-NANOTEC-SLRI XAS Beamline.

CHAPTER IV
RESULTS AND DISCUSSIONS

The characterization of the glass sample involved an in-depth analysis of its crystal structure, which was meticulously investigated through X-ray diffraction techniques (XRD). This method provided valuable insights into the internal arrangement and properties of the glass material, contributing to a comprehensive understanding of its structural composition. In addition, we have conducted extensive studies in various aspects. The electrochemical properties were assessed through charge-discharge curve analysis. Furthermore, impedance values within the battery electrodes were precisely measured using the Electrochemical Impedance Spectroscopy (EIS) technique. Additionally, the energy density measurements of glass electrodes were carried out using cyclic voltammetry (CV). X-ray Absorption Near Edge Structure (XANES) provided information on the electronic and structural properties, and Extended X-ray Absorption Fine Structure (EXAFS) revealed the local structural environment around specific atoms.

Figure 4.1 Show the physical and morphological properties of samples a) $[NC11]_m$, b) $[NC11+V]_m$, c) $[NC11]_m+V]_m$, d) $[NC41]_m$, e) $[NC41+V]_m$ and f) $[NC41]_m+V]_m$ respectively.

4.1 Physical characteristics

Figure 4.1 illustrates the physical surface of LBO glass samples that have been mixed with varying concentrations of Ni/Co_3O_4 and V_2O_5. The prepared glass samples, after the firing process, exhibit a dense and smooth surface structure. The addition of cobalt, in different concentrations, results in some samples displaying a black coloration, indicating successful incorporation of the dopants into the glass matrix. The glass produced appears to be of high quality, characterized by its density and a uniform surface.

One of the notable features of the glass is its hard yet brittle nature, a typical characteristic of glass materials. This brittleness makes the material prone to breaking, often resulting in sharp cracks when fractured. Despite this, the surface of the glass retains a shiny, reflective gleam, further confirming the integrity of the glass's surface and its smoothness. These qualities suggest that the material has maintained its glassy properties while incorporating the metallic oxides, which likely contribute to its coloration and potentially to other physical and chemical properties. The high quality and density of the glass surfaces are key indicators of successful preparation, which will influence the material's application in various fields, such as energy storage or electronic devices.

4.2 The crystal structure was investigated by X-ray diffraction

The phase formation of the glass samples was confirmed through X-ray diffraction (XRD) using a Bruker D8 Advance with a Cu k alpha source (λ = 1.54 Å), Detectoe 1 Dimesional conpound silicon strip, High temp 25-1600°C, 40kv 40mA. XRD data were collected at room temperature over a 2θ range of 10° to 80°, with a scanning speed of 2.4 deg/min and a step size of 0.02 s. From the experimental results of making glass samples according to the formula in this work, it was found that the phase verification results of XRD patterns It was found that it was an imperfect amorphous phase. as shown in Figure 4.2 and Table 4.2, calculated using Equation 4.1.

$$\text{Crystallinity (\%)} = \frac{\text{Area of crystalline peaks}}{\text{Area of all peaks (crystalline+amorphous)}} \times 100 \quad \text{Equation 4.1}$$

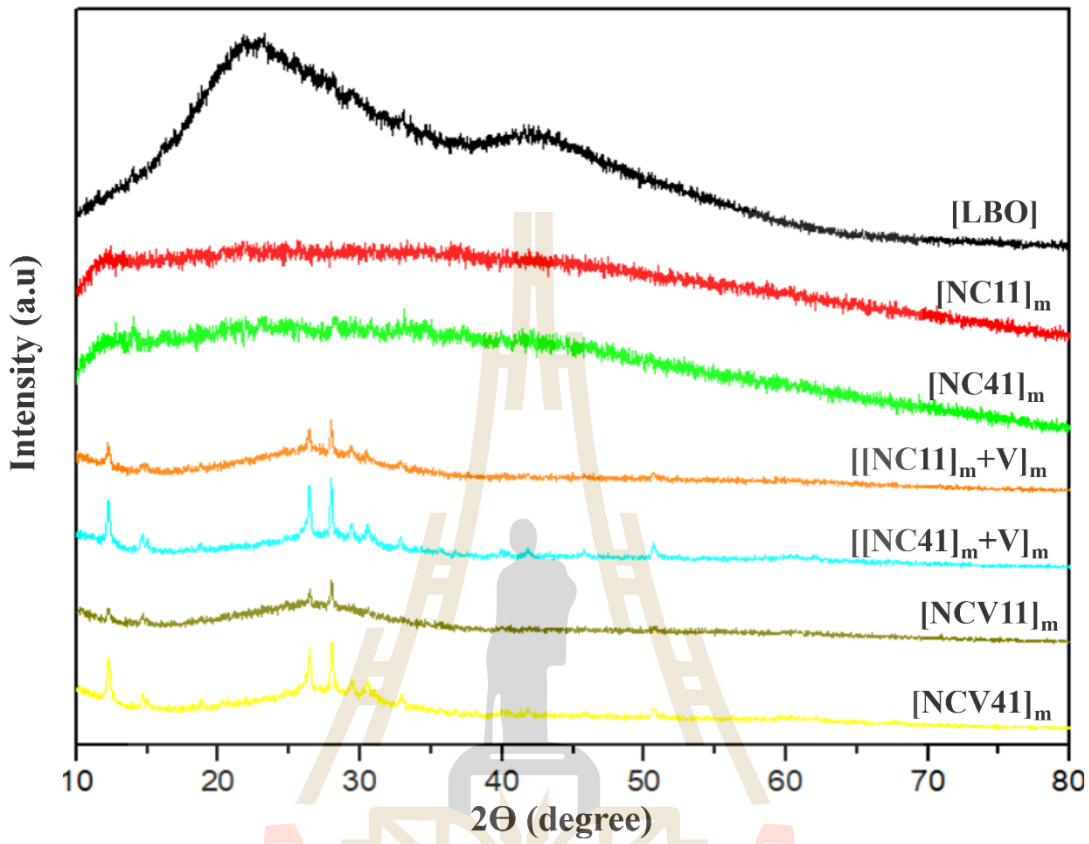

Figure 4.2 The XRD patterns of LBO, $[NC11]_m$, $[NC41]_m$, $[NC11]_m+V]_m$, $[NC41]_m+V]_m$, $[NC11+V]_m$ and $[NC41+V]_m$ respectively.

The $[NC11]_m$ and $[NC41]_m$ sample exhibits a glassy nature with less than 3% crystallinity. In comparison, the $[[NC11]_m+V]_m$, $[[NC41]_m+V]_m$, $[NC11+V]_m$ and $[NC41+V]_m$ samples show about 30% crystallinity, indicating that adding V_2O_5, followed by sintering, induces the formation of glass ceramics. To determine the crystalline structure, the observed peaks were analyzed using Jana2006 software and the Materials Project model, identifying them as corresponding to Lithium Hexaborate ($Li_6B_4O_9$). The peaks in the $[[NC11]_m+V]_m$, $[[NC41]_m+V]_m$, $[NC11+V]_m$ and $[NC41+V]_m$ samples matched the characteristic planes of $Li_6B_4O_9$, such as (021), (100), and (11-2), as shown in figure 4.3. The base glass, referred to as Lithium Tetraborate ($Li_2B_4O_7$ or LBO), exhibited an amorphous structure (black line, figure 4.2).

Table 4.1 Shows the percentage of crystallinity of the material of all sample.

No	Sum of area of crystalline peaks	Area of all peaks	Crystallinity of this material
$[NC11]_m$	65	4642	1 %
$[NC41]_m$	186	6900	3 %
$[NC11]_m+V]_m$	402	2426	17 %
$[NC41]_m+V]_m$	784	2611	30 %
$[NC11+V]_m$	280	2471	11 %
$[NC41+V]_m$	786	2682	29 %

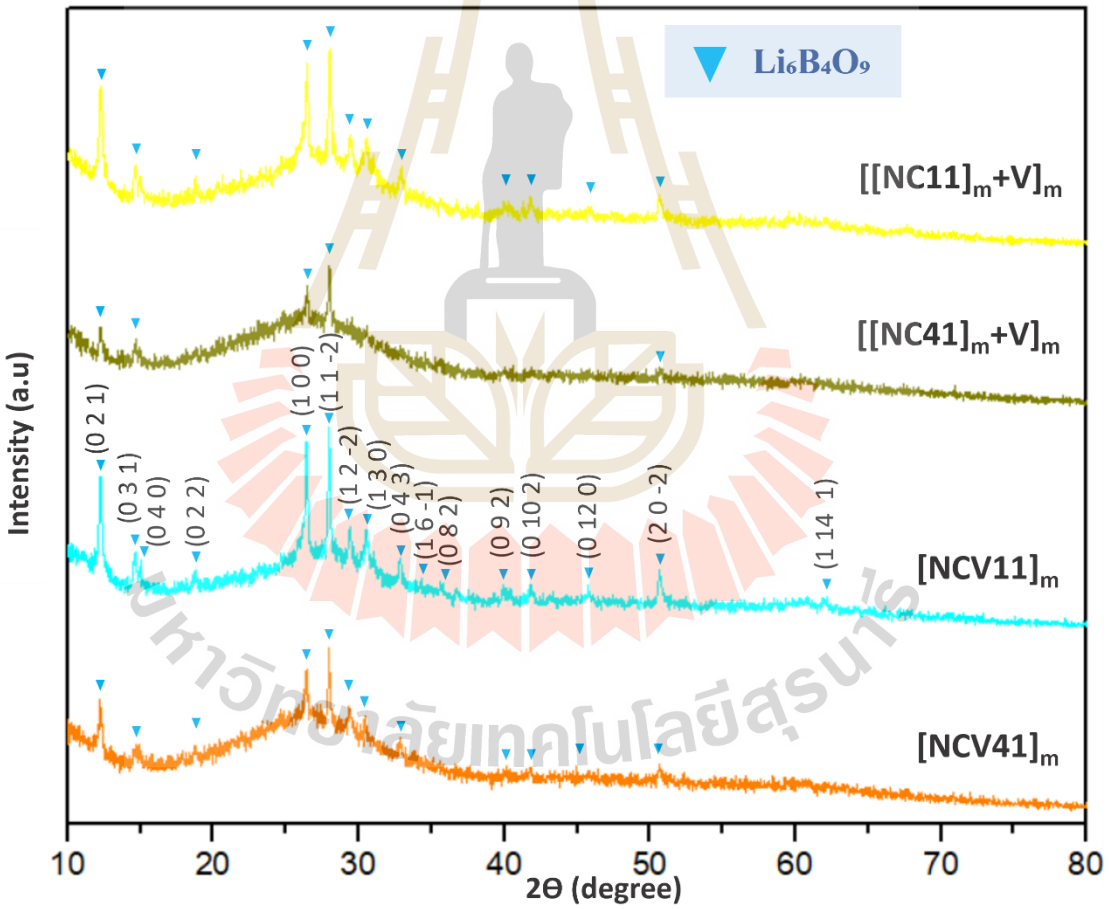

Figure 4.3 XRD patterns of the $Li_6B_4O_9$ ceramic.

When LBO was mixed with Ni/Co and subjected to a second sintering process ($[NC]_m$), it retained its amorphous nature (red and green line). The study of the $Li_6B_4O_9$

peak revealed that the $[[NC]_m + V]_m$ sample exhibited a higher peak intensity compared to the $[NCV]_m$ sample. This indicates that the sample with a lower peak intensity possesses a more amorphous nature (Figure 4.4). The improved crystallinity in the $[[NC]_m + V]_m$ sample is attributed to undergoing three melting cycles. These repeated cycles facilitated more thorough crystallization than samples that underwent only two cycles. Consequently, the crystalline structure in the $[[NC]_m + V]_m$ sample became more defined and complete after the additional melting process.

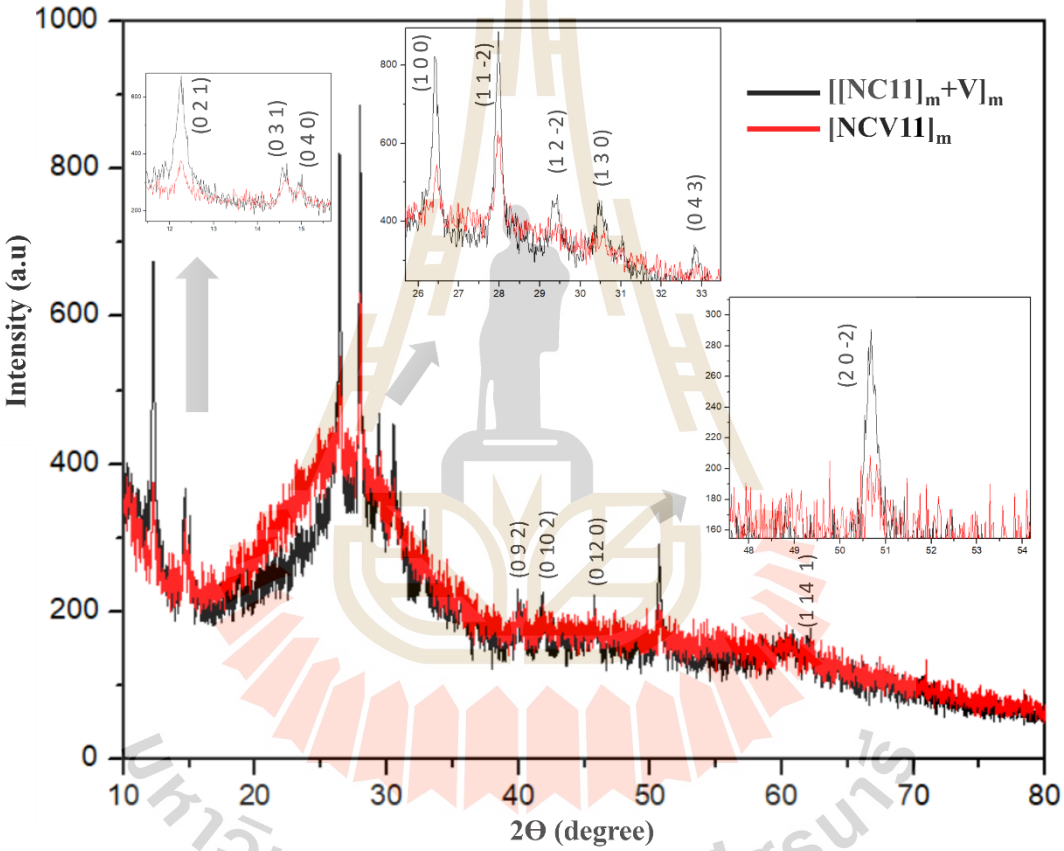

Figure 4.4 The graph compares the intensity of the $Li_6B_4O_9$ peak between the samples $[[NC]_m + V]_m$ and $[NCV]_m$.

$Li_6B_4O_9$ exhibits a monoclinic crystal structure with refined cell parameters of a = 3.39 Å, b = 23.65 Å, c = 9.73 Å, and angles α = 90.00°, β = 107.90°, and γ = 90.00°, resulting in a unit cell volume of 743.42 Å^3. The crystal system is monoclinic, with a Hall number of -P 2ybc and an International Number of 14, classified under the space

group $P2_1/c$. It has a density of 2.04 $g{\cdot}cm^{-3}$ and possible oxidation states of Li^{+}, B^{3+}, and O^{2-}. There are four formula units per cell, with the lithium, boron, and oxygen atoms occupying the Wyckoff general position 4e, with full occupancy. The boron atoms form planar BO_3 units, linked at their vertices to create quasi-planar B_4O_9 groups, which stack perpendicular to the [100] direction. Lithium atoms are located between these B_4O_9 platelets, coordinated by oxygen atoms within distorted tetrahedra and trigonal bipyramids. The Li–O bond lengths range from 1.90 to 2.40 Å, contributing to varying lithium coordination across the structure. This complex arrangement contributes to the unique electrochemical properties of $Li_6B_4O_9$ (G. Rousse, B. Baptiste, and G. Lelong, 2014; G. l. Rousse, B. Baptiste, and G. r. Lelong, 2014; Zhou, Pang, Wang, Qi, and Reaney, 2018).

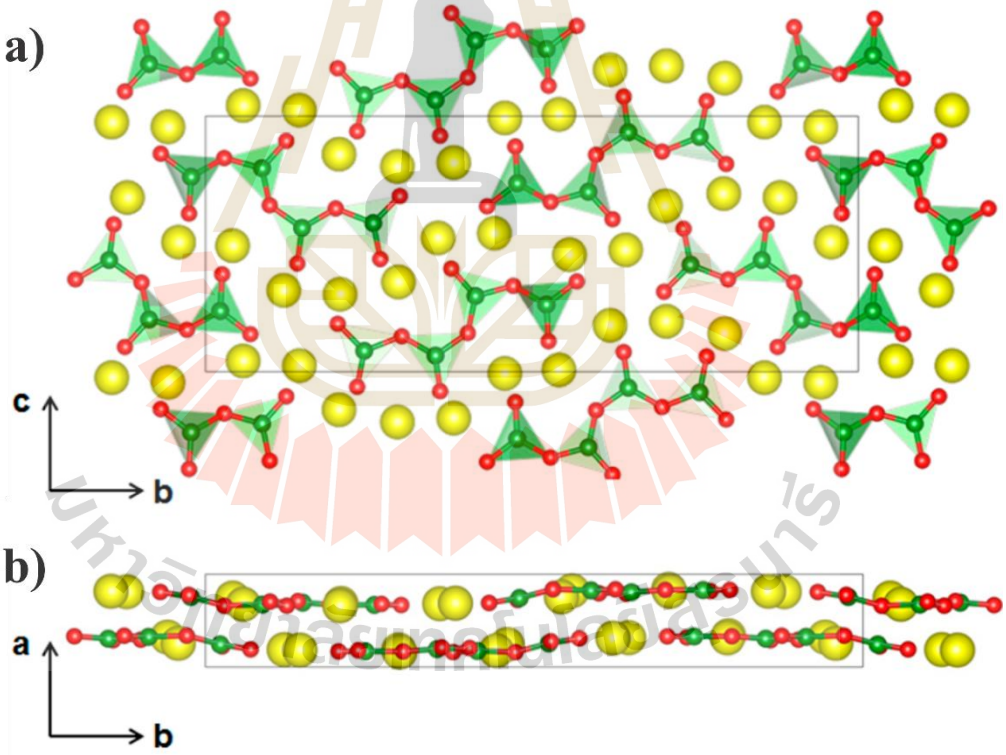

Figure 4.5 The structure of $Li_6B_4O_9$, when viewed along the [100] a) and [001] b) crystallographic axes, shows B, O, and Li atoms represented in green, red, and yellow, respectively. The BO_3 triangular units are also depicted in green, highlighting the arrangement of boron and oxygen atoms within the lattice structure.

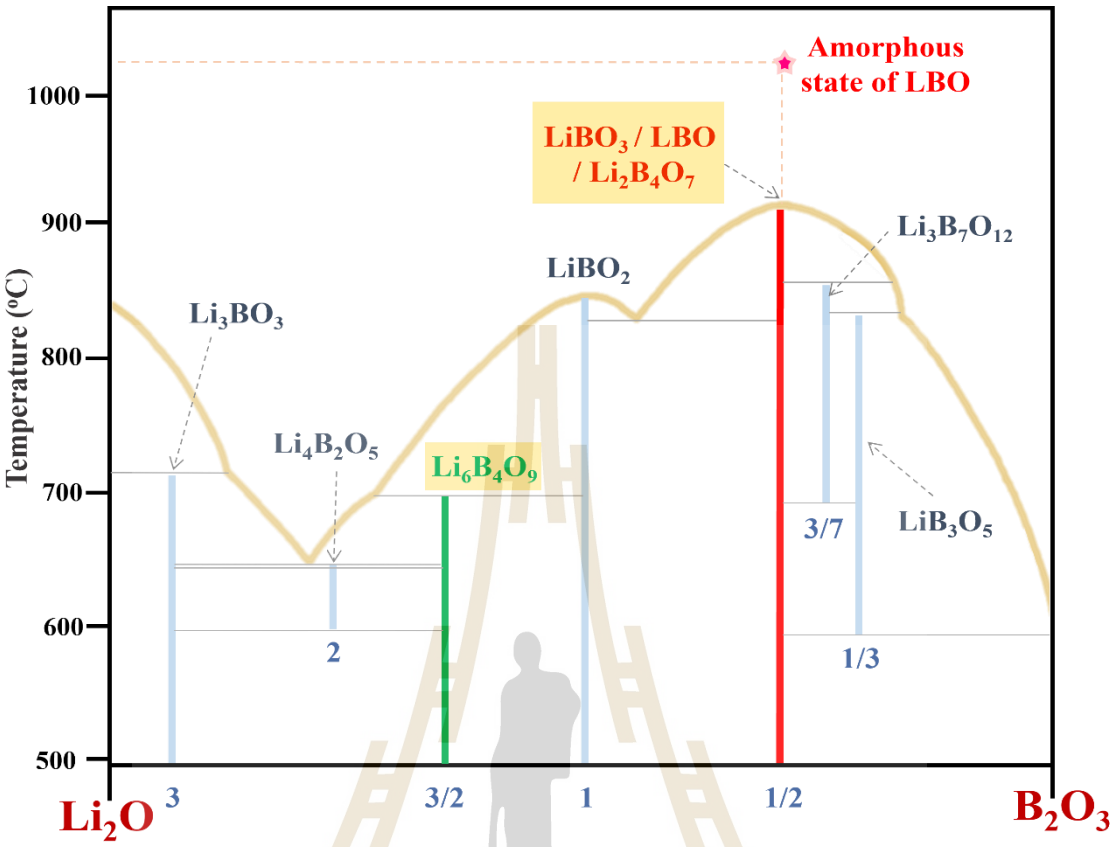

Figure 4.6 The binary phase diagram of Li_2O–B_2O_3, adapted from reference (G. l. Rousse et al., 2014).

The Li_2O–B_2O_3 binary system, which has been studied for over 50 years, exhibits significant complexity with around 10 distinct compounds, some of which are high-temperature or pressure-induced polymorphs (Figure 4.6). In ceramic production, solid-state reactions are often favored over soft chemical routes due to their cost-effectiveness and scalability (G. l. Rousse et al., 2014). However, sourcing B_2O_3 for borate production poses challenges. Both H_3BO_3 and B_2O_3 were initially used, but issues such as the loss of B_2O_3 through volatilization and solubility in aqueous environments led to complications, including the formation of $Li_4B_2O_5$. To compensate for this, excess B_2O_3 was added, which ultimately resulted in lithium metaborate ($LiBO_2$) formation. $LiBO_2$ has proven to be a stable and suitable starting material for synthesizing $Li_6B_4O_9$ when reacted with Li_2CO_3. according to the following equation:

$$4LiBO_2 + Li_2CO_3 \longrightarrow Li_6B_4O_9 + CO_2 \qquad \text{Equation 4.2}$$

Successfully forms $Li_6B_4O_9$ ceramics when sintered at 600°C, as confirmed by XRD traces showing no secondary phases. Full density is achieved near 630°C, suggesting $LiBO_2$'s superiority over other borate sources like H_3BO_3 and B_2O_3. The crystal structures of compounds within the Li_2O–B_2O_3 system have been thoroughly investigated, with six lithium borate crystals synthesized and characterized, including $Li_6B_4O_9$ (Zhou et al., 2018).

The incorporation of V_2O_5 into the glass system facilitates the bonding between boron and vanadium, leading to the formation of a glass matrix. Several studies have reported that in Li_2O– V_2O_5–B_2O_3 glass systems, increasing the V content significantly enhances the bonding between vanadium and boron (Saetova, Raskovalov, Antonov, Denisova, and Zhuravlev, 2020; Saetova et al., 2018). This finding has also been corroborated by molecular dynamics simulations, further confirming the strengthening of these interactions as V content increases. Meanwhile, the amount of Li_2O remains unchanged, but the B_2O_3 content decreases due to its reaction with vanadium. Consequently, the remaining ratio of Li_2O to B_2O_3 is 3:2 (Lelong et al., 2017). According to the binary phase diagram (Figure 3a), this ratio at approximately 700°C results in the formation of LiB_4O_9. This finding is consistent with the peaks observed in the $[[NC41]_m$ $+V]_m$ and $[NCV41]_m$ samples (Figure 4.3).

From the experimental data, a phase diagram of the melt quenching process was simulated as shown in Figure 4.7a-b. In Figure 4.6, it is evident that the research employed a temperature of 1100°C for the crystallization process, followed by rapid cooling to prevent crystallization, resulting in an amorphous structure in the glass, as seen in samples like LBO and $[NC41]_m$ (Figure 4.7b). This outcome aligns with the binary phase diagram, which indicates that rapid cooling leads to the formation of an amorphous structure.

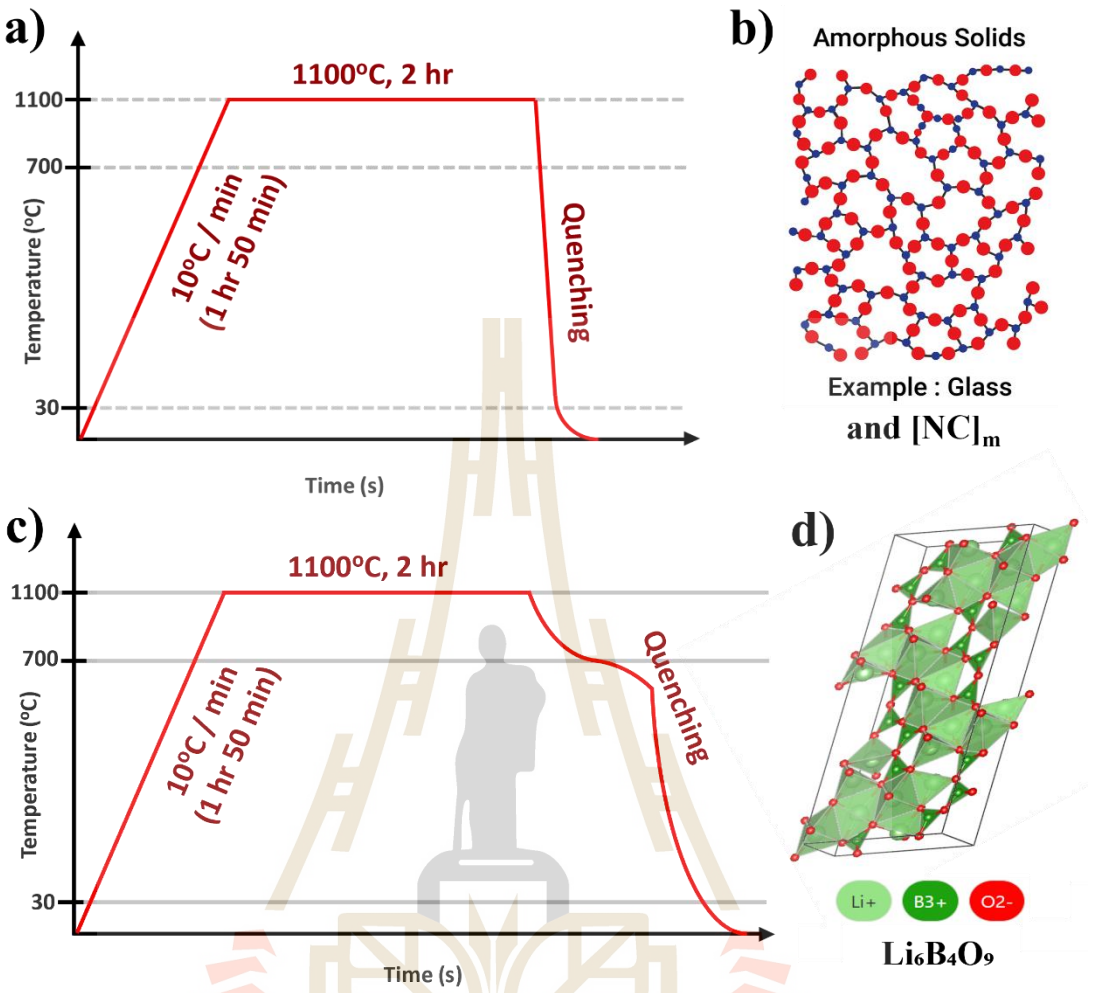

Figure 4.7 Schematic diagram of the melting process steps.

The formation of the glass-ceramic structure of $Li_6B_4O_9$, as illustrated in Figure 4.7c-d, involves a melt-quenching process. In step (Figure 4.7a) of this process, LBO is first melted and then rapidly cooled to create a disordered structure. This is followed by a melt quenching to induce partial crystallization, resulting in a material that exhibits ceramic-like. In this study, the sample underwent two firing steps consistent with the glass-ceramic formation process. Initially, the LBO glass base was prepared by melting at 1100°C and then quickly cooled. It was then combined with Ni, Co, and V_2O_5, followed by a second firing at the same temperature of 1100°C. This heat treatment encourages atoms to rearrange into a more ordered, crystalline structure, though some portions may remain in a glassy state. Previous studies have indicated that the addition

of a significant amount of vanadium (75%) can slow the cooling process, as depicted in the cooling diagram in Figure 4.7b. The low sintering temperature of $Li_6B_4O_9$ ceramic (Figure 4.7d), approximately 700°C, allows for atomic movement and realignment within the glass, ultimately leading to the formation of a crystalline structure.

4.3 Battery capacity measurement

Battery capacity measurement is a crucial process for assessing the performance and efficiency of batteries. The capacity of a battery is measured in ampere-hours (Ah) or milliampere-hours (mAh). The process involves fully charging the battery to a specified voltage, followed by discharging it continuously until the voltage drops to a predetermined level. The capacity is calculated based on the amount of current discharged over this period. This measurement can be conducted through controlled charging and discharging conditions. Accurate battery capacity measurement is essential for evaluating the battery's ability to store and deliver energy.

C-rate or Charge Rate is an indicator of the charging or discharging rate of a battery in relation to its full capacity. The C-rate value shows how fast the battery can be charged or discharged compared to its full capacity. For example, a C-rate of 1C means the battery can be fully charged or discharged in 1 hour, while a C-rate of 0.5C means it will take 2 hours to charge or discharge the battery fully. A lower C-rate results in a longer charging or discharging time. Selecting an appropriate C-rate helps to extend the battery's lifespan and maintain its performance over the long term.

$$C\text{-rate} = QI \qquad \text{Equation 4.3}$$

In this study, a C-rate of 0.2 Ah/g was used, meaning that charging or discharging took place over 5 hours. This value was determined experimentally to achieve optimal performance. From the equation, the current used for charging or discharging was calculated to be 0.04 A/g. The average weight of each sample used in the anode substrate was 8.64 mg (All substrate). To determine the mass of the active material in each sample (Total mass), the formula (Total mass - All substrate) * 0.8 was applied,

where the factor of 0.8 accounts for the presence of carbon black (CB) along with the active material. Once the mass of the active material was obtained, the current was divided by the mass to calculate the starting and ending current required for the experiment.

Setting the voltage range in battery testing is a critical step that impacts the accuracy and reliability of measurements. Setting the voltage range too low may result in missing important data and an inability to accurately observe differences in low battery voltages. Conversely, setting the voltage range too high can lead to damage or risk of damage to the battery. Considering the appropriate voltage range for testing is crucial to obtain accurate and trustworthy results. It also helps prevent potential damage to the battery from testing with inappropriate voltage levels.

In some samples, the voltage range is adjusted due to the low charge and conductivity of LBO, which necessitates the use of a lower voltage range to improve its electrical conductivity. In this study, a voltage range of 0.2–2V was used for LBO. In contrast, V_2O_5 was set to operate within the 2–4V range due to its suitable electrical properties and behavior in this voltage range. The 2–4V range is crucial for V_2O_5 in several aspects, such as structural stability, electrical performance, and redox reactions, involving changes in oxidation states between V^{5+} and V^{3+}, allowing for efficient energy storage and release. Moreover, this voltage range enables V_2O_5 to work synergistically with other materials in lithium-ion batteries, enhancing overall battery performance.

For the other samples, the capacity values are illustrated in Figure 4, and the summarized data are presented in Table 4.2. This table compares the samples using the average values from cycles 1 to 100 for calculating specific capacity, energy density, and capacity retention. The data reveal that the $[NC41]_m$ sample, used as the cathode, exhibited the highest specific capacity in the first cycle. However, as the number of cycles increased, the capacity decreased rapidly. This phenomenon is attributed to the Initial Coulombic Efficiency (ICE), which is the ratio of the energy a battery can discharge in the first cycle compared to the energy it was charged with. ICE is typically lower

than the charged energy due to factors such as energy loss during charging and discharging, the formation of a protective Solid Electrolyte Interphase (SEI) layer on the electrode surface, and heat loss. This SEI layer, which forms during the first cycle, consumes some lithium ions, thereby reducing the battery's capacity to discharge energy in subsequent cycles (He, Sun, Tang, Wang, and Shao, 2019). For this work, we excluded the first cycle and designated the second cycle as the new first cycle. As for the 99^{th} cycle, it represents the 100^{th} cycle.

In the battery testing, coin cells were assembled following the procedures mentioned earlier. The voltage range was appropriately set for each sample material: 0.2-2V for LBO, 0.5-3V for $[NC41]_m$ and 2-4V for samples containing V_2O_5. These voltage ranges were selected based on the suitability of the materials' properties and electrical behavior within these ranges.

The specific capacity compared to the number of cycles (Cycle Test) from 1 to 100 cycles, as shown in Figure 4a, revealed that LBO had an average capacity of 11.81 mAh/g (average from cycles 5 to 100) and an energy density of 272.01 mWh/g, which is relatively low. However, its capacity was notably stable, consistent with reports on LBO's stability, such as the study by (Siriroj et al., 2022), which found that the battery maintained 99.28% of its capacity after numerous cycles, indicating a loss of only 0.72% from its initial capacity. Meanwhile, the battery using V_2O_5 as the cathode delivered approximately 224.33 mAh/g and had an energy density of about 653.14 mWh/g, which is relatively high. However, the battery maintained only 78.57% of its initial capacity after 100 cycles, indicating a 21.43% reduction in capacity retention. Data from Figure 4a showed a significant decrease in the capacity retention of V_2O_5 over the number of cycles, which is a natural property of V_2O_5. The vanadium oxide structure in this material is fragile and prone to degradation after repeated use, leading to a rapid decrease in battery capacity (Cheah, Aravindan, and Madhavi, 2013; Li et al., 2021).

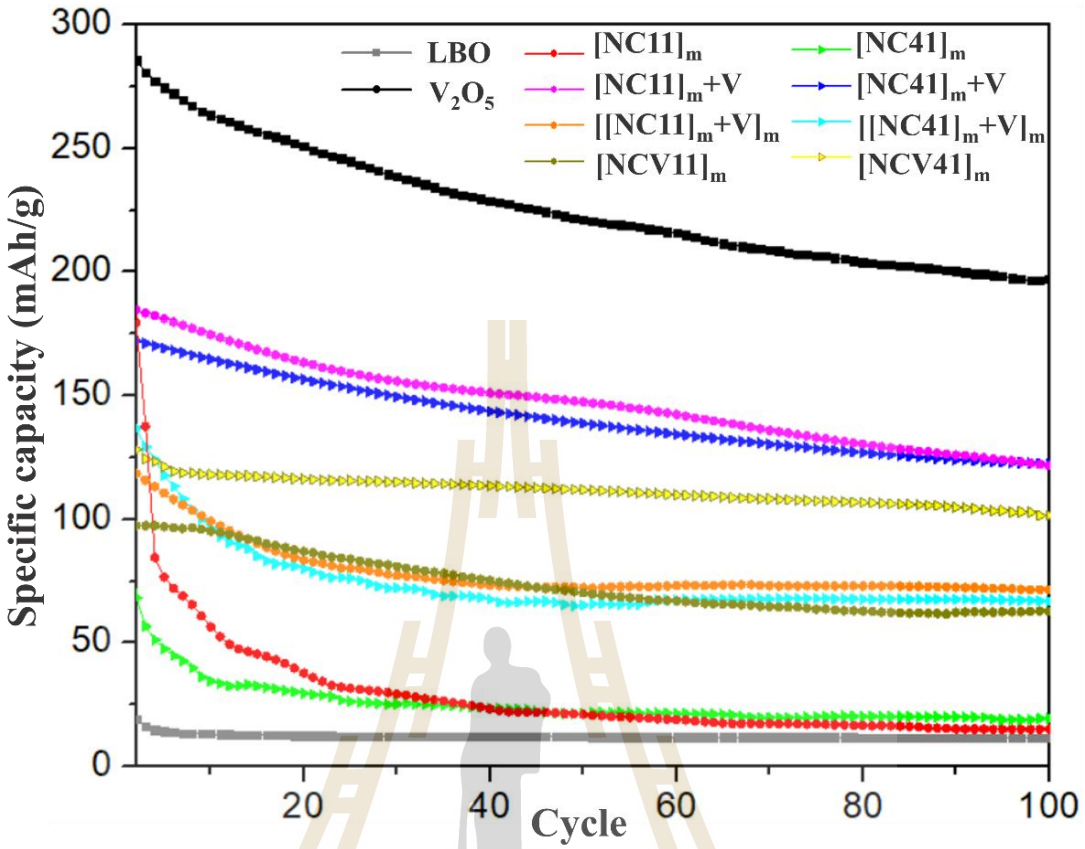

Figure 4.8 Specific capacity as a function of the number of cycles.

In the $[NC41]_m$ sample, the average specific capacity and energy density were the lowest, with values of 24.09 mAh/g and 20.55 mWh/g, respectively. Additionally, the capacity retention was 65.54%, which is also the lowest among the samples. This indicates that the combination of LBO with Ni:Co in a 4:1 ratio, followed by the melting process, resulted in an increase in capacity compared to pure LBO, with an increase of approximately twofold or around 54%. Moreover, the sample also exhibited stability in accordance with the properties of LBO. In the case of the $[NC11]_m$ sample, the average specific capacity and energy density were the lowest, with values of 24.09 mAh/g and 20.55 mWh/g, respectively. Additionally, the capacity retention was 65.54%. Over time, while the capacity remained relatively stable, the specific capacity was still quite low.

Table 4.2 Illustrates the Specific capacity (mWh/g) and Energy density (mAh/g) along with the Capacity Retention (%).

Sample	Specific capacity (mAh/g)	Energy density (mWh/g)	Cycle 1	cycle 100	Capacity Retention (%)	Capacity Fade (%)
LBO	11.82	8.57	12.64	11.69	92.46	7.54
V_2O_5	226.31	658.97	283.51	196.48	69.30	30.70
$[NC11]_m$	29.25	19.90	96.004	15.08	15.71	84.29
$[NC11]_m$+V	147.33	430.02	161.96	125.61	77.56	22.44
$[NC11]_m$+V$]_m$	78.61	219.45	118.39	71.27	60.20	39.80
$[NC11+V]_m$	74.01	201.45	102.26	62.69	61.31	38.69
$[NC41]_m$	25.19	21.46	68.18	19.26	28.25	71.75
$[NC41]_m$+V	141.26	414.58	174.26	122.94	70.55	29.45
$[NC41]_m$+V$]_m$	74.17	207.27	142.26	66.94	47.06	52.94
$[NC41+V]_m$	111.42	306.26	130.43	105.24	80.69	19.31

The experimental results of the samples mixed with 75% V_2O_5 revealed that the sample $[NC11]_m$ +V (Figure 4.8) had an average capacity of approximately 59.85 mAh/g (average from 1-100 cycles) and an energy density of 169.00 mWh/g, with a capacity retention of 62.06%. The $[NC41]_m$ +V sample showed the highest capacity and energy density at 140.13 mAh/g and 410.93 mWh/g, respectively. The observed capacity values are relatively high, yet the stability remains suboptimal.

The samples that were mixed with 75% V_2O_5 and subjected to the melt quenching process had different results. The $[[NC11]_m +V]_m$ lt sample had an average capacity and energy density of around 77.05 mAh/g and 215.90 mWh/g, with a capacity retention of 87.36%, indicating a capacity loss of only 12.64% over 100 continuous cycles. Meanwhile, the $[[NC41]_m +V]_m$ sample had an average capacity of 72.36 mAh/g and an energy density of 202.04 mWh/g, which aligns with previous reports (Siriroj et al., 2023; Siriroj et al., 2022), and a capacity retention of 85.05%, showing a capacity loss of only 14.95% after 100 cycles. The observed capacity, while measurable, remains below the desired level and exhibits stability that is not yet satisfactory. Further optimization is required to enhance both the capacity and stability to meet the expected performance standards.

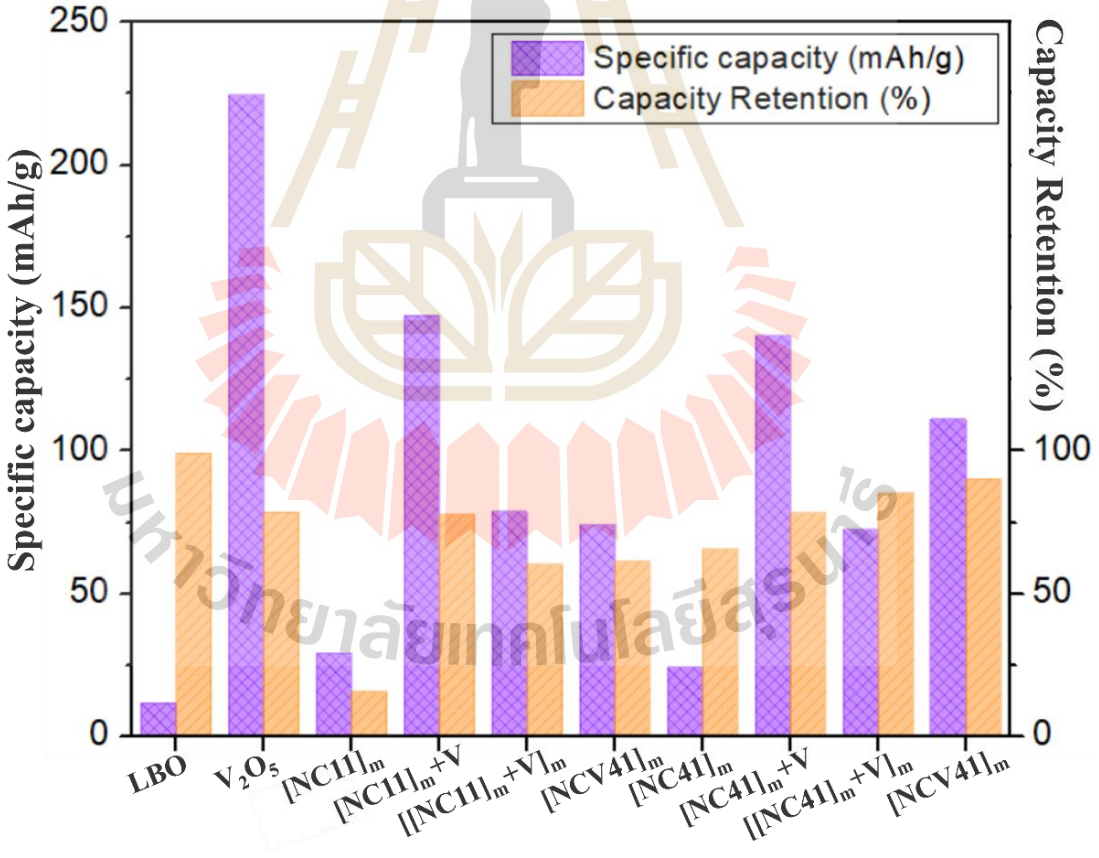

Figure 4.9 Comparison of Specific capacity and Capacity retention in average cycle test of 1 to 100 cycles.

For the samples where LBO, Ni, Co, and V_2O_5 were mixed through the melt quenching process, the $[NCV11]_m$ sample showed an average capacity of around 71.97 mAh/g and an energy density of 198.64 mWh/g. The calculated capacity retention was 79.47%, meaning a capacity reduction of only 20.53% after 100 cycles. The $[NCV41]_m$ sample exhibited an average capacity of 110.96 mAh/g and an energy density of 304.80 mWh/g, with a capacity retention of 90.27%, showing only a 9.73% capacity loss after 100 continuous cycles. The $[NCV41]_m$ sample demonstrated a notably high capacity, which is highly satisfactory. Moreover, it exhibited excellent stability throughout testing. In addition to its promising performance, the fabrication process of this sample is straightforward and uncomplicated, further enhancing its practicality for application.

For all four samples, an additional firing process was applied, which caused significant capacity reduction, as shown in Figure 4.8. This was due to the formation of a glass-ceramic structure of $Li_6B_4O_9$ during the firing process, as displayed in Figure 4.3, which revealed a hexaborate structure. This structure enhances strength and durability, allowing the material to withstand long-term use in harsh conditions requiring high strength and damage resistance (Cahill and Graeve, 2019).

4.4 The electrochemical properties by charge and discharge curve

In batteries, the electrochemical properties are evaluated using charge and discharge curves. These curves are crucial for testing various performance aspects, such as capacity, voltage stability, and overall energy efficiency during cycling. By analyzing the charge and discharge profiles, researchers can assess the battery's ability to store and release energy, monitor the voltage changes at different states of charge, and identify any potential degradation in performance over time. This method provides valuable insights into the battery's behavior under real-world operating conditions.

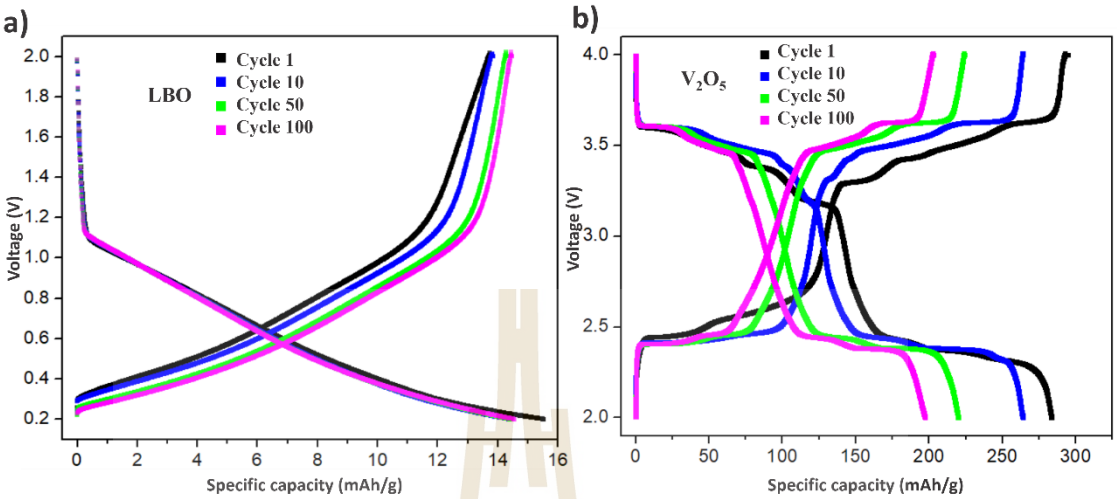

Figure 4.10 The voltage-capacity curves for charge and discharge cycles of a) LBO and b) V_2O_5 at the 1st, 10th, 50th, and 100th cycles.

The results of the charge and discharge curve also revealed that LBO exhibited better voltage stability and overall energy efficiency during cycling compared to V_2O_5. LBO (Figure 4.10a) maintained a consistent voltage throughout the charge-discharge process, contributing to its stable performance over time. In contrast, V_2O_5 (Figure 4.10b) showed significant voltage fluctuations during charging states, indicating instability in its electrochemical behavior. Additionally, V_2O_5 experienced noticeable degradation in performance over time, with a reduction in capacity retention, highlighting its vulnerability to structural breakdown after prolonged use.

Figure 4.11 presents the charge and discharge cycles at the 1st, 10th, 50th, and 100th cycles. From the figure, it is evident that a) $[NC11]_m$ and b) $[NC11]_m$ +V show significant changes as the number of cycles reaches 100, indicating a decline in performance. In contrast, c) $[[NC11]_m$ +V$]_m$ and d) $[NCV11]_m$ exhibit improved stability in voltage and overall energy efficiency throughout the cycling process, demonstrating better performance and consistency over time.

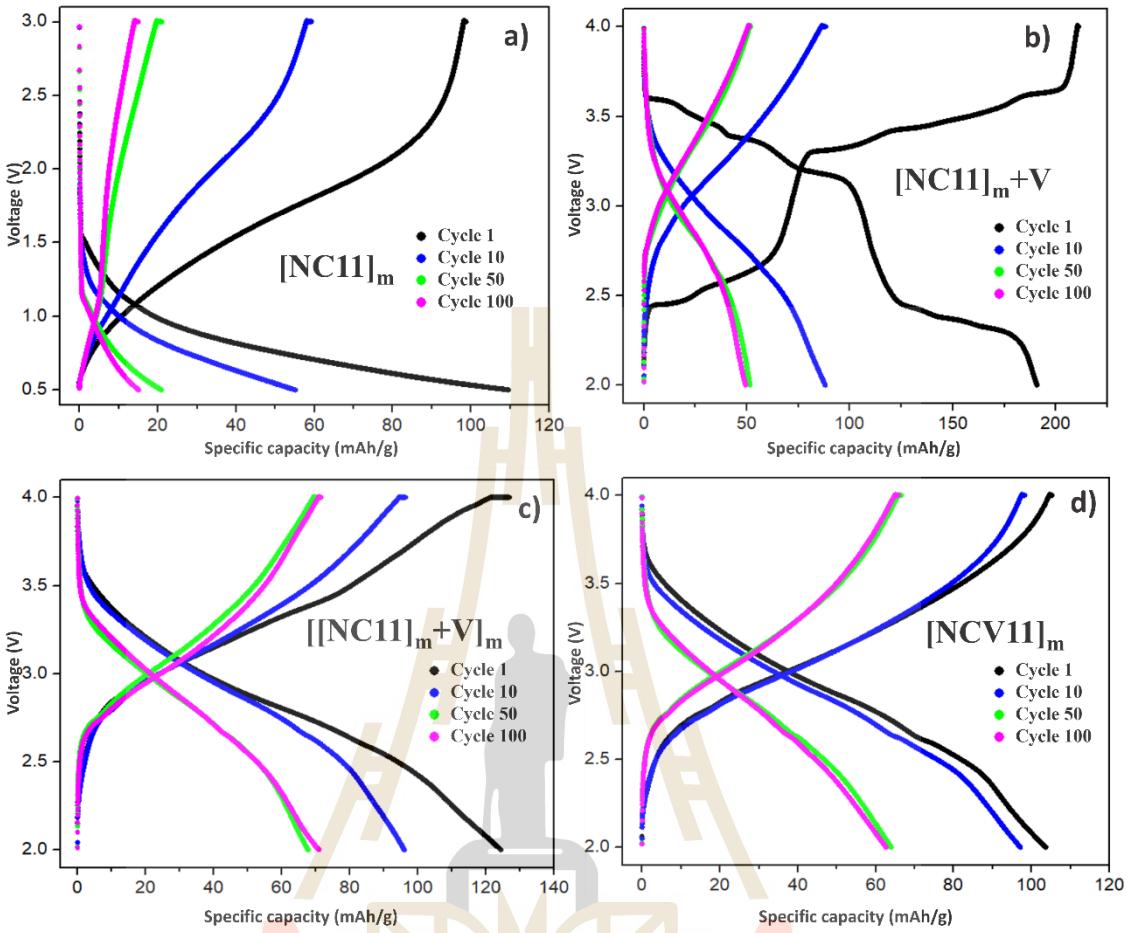

Figure 4.11 The voltage-capacity curves for charge and discharge cycles of a) $[NC11]_m$, b) $[NC11]_m$ +V, c) $[[NC11]_m$ +V$]_m$, and d) $[NCV11]_m$ at the 1st, 10th, 50th, and 100th cycles.

Figure 4.12 illustrates the charge and discharge profiles at the 1st, 10th, 50th, and 100th cycles. The results reveal noticeable degradation in performance for samples a) $[NC41]_m$, b) $[NC41]_m$ + V, and c) $[[NC11]_m$ + V$]_m$ by the 100th cycle. Conversely, sample d) $[NCV4\ 1]_m$ showed enhanced stability in both voltage and energy efficiency, maintaining more consistent performance throughout the cycling process.

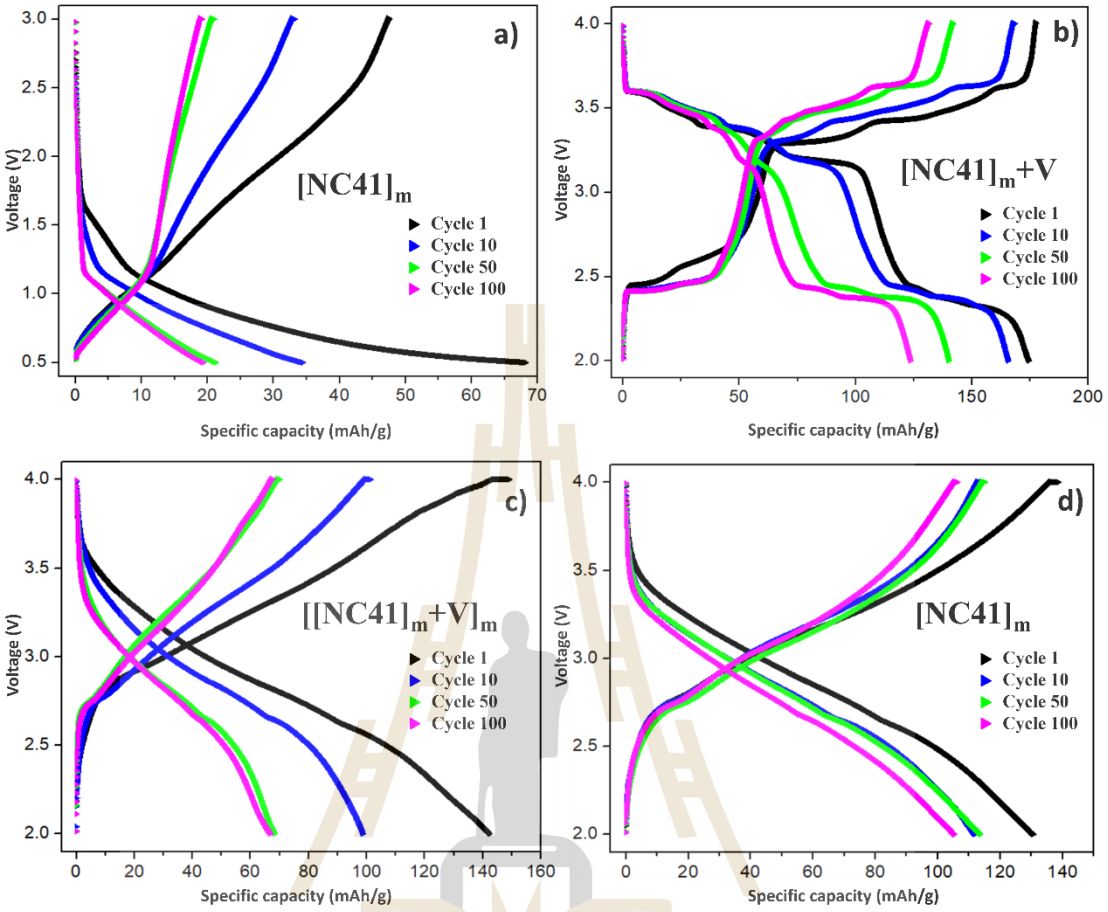

Figure 4.12 The voltage-capacity curves for charge and discharge cycles of a) $[NC11]_m$, b) $[NC11]_m$ +V, c) $[[NC11]_m$ +V$]_m$, and d) $[NCV11]_m$ at the 1st, 10th, 50th, and 100th cycles.

4.5 The Electrochemical Impedance Spectroscopy (EIS) technique was employed to determine impedance values within the battery electrodes

The study utilized Electrochemical Impedance Spectroscopy (EIS) to assess the impedance values of the battery electrodes. This technique provided valuable insights into the internal resistance and charge transfer properties of the materials, helping to evaluate their overall electrochemical performance. The EIS analysis allowed for a deeper understanding of the conductivity and resistance characteristics, which are crucial factors for optimizing battery efficiency and longevity.

To gain further insights, cyclic voltammetry (CV) and electrochemical impedance spectroscopy (EIS) measurements were conducted. A new set of cells was used, with EIS measurements taken first, followed by three cycles of CV, and a final EIS measurement. The CV measurements began from the open-circuit voltage of the cells, which was approximately 2.5 V, and were performed at a scan rate of 0.5 mV/s.

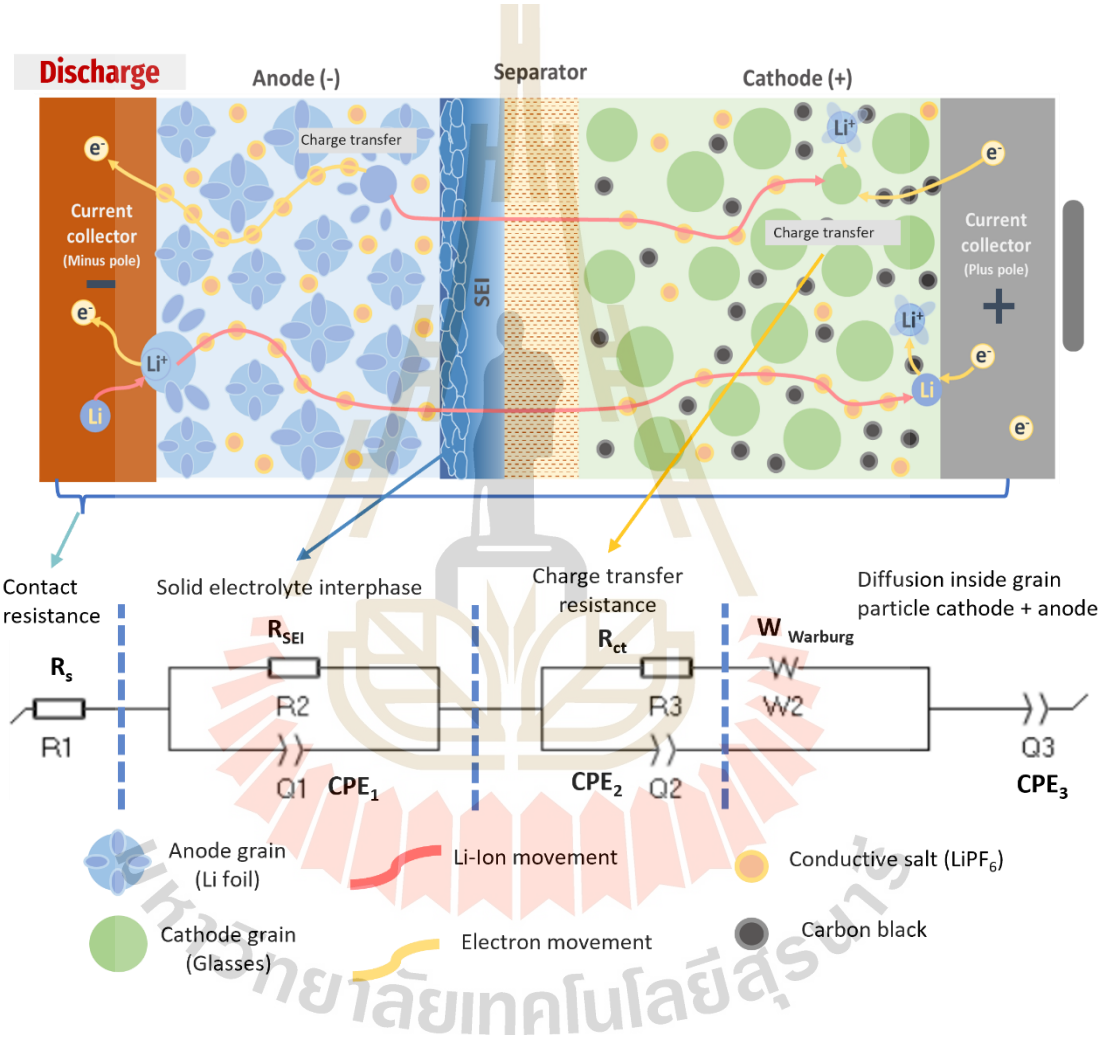

Figure 4.13 The movement of ions and electrons during discharge was examined using a lithium-ion battery with a lithium foil anode and a glassy carbon cathode as an example.

The internal changes within the cell during testing were evaluated by conducting EIS measurements before and after the test. The EIS results, presented in Figure 4.14, were analyzed by fitting the data to the model shown in Figure 4.13.

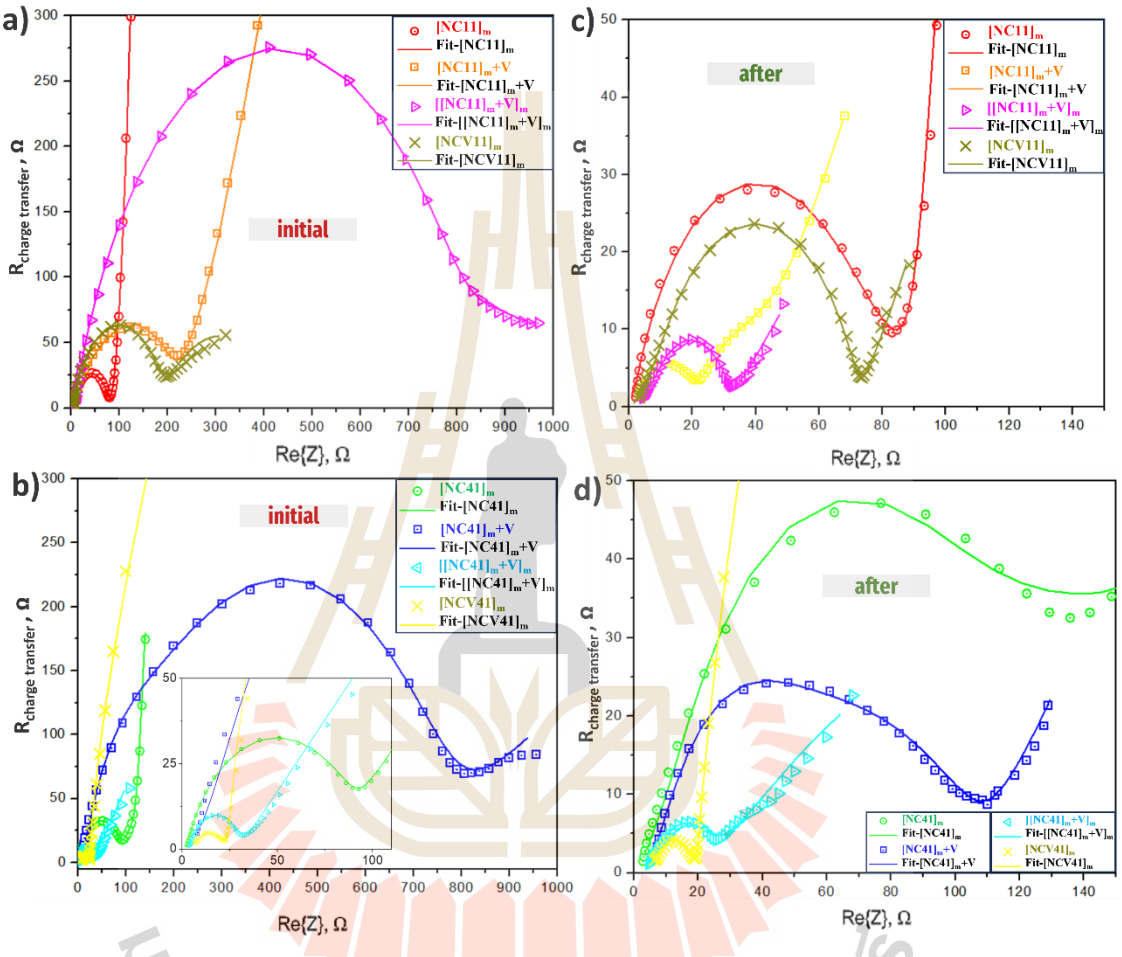

Figure 4.14 c) The initial cell assembly and d) the condition after three cycles of CV testing were analyzed using EIS measurements.

The charge transfer resistance, which reflects ion transfer within the cathode, was examined for the $[NC11]_m$ and $[NC41]_m$ sample. It was found that the internal resistance before measurement and after three cycles of CV (Figures 4.14a-d) did not differ significantly. In contrast, the $[NC11]_m$ +V and $[NC41]_m$ +V sample exhibited a high initial internal resistance, reaching up to 600-800 **Ω**. This elevated resistance is attributed to

the low ionic conductivity of the LBO glass and V_2O_5, which contributed to the increased internal resistance of the cell. However, after CV testing, a subsequent EIS measurement revealed that the resistance decreased to 20-80 Ω, though it still remains relatively high.

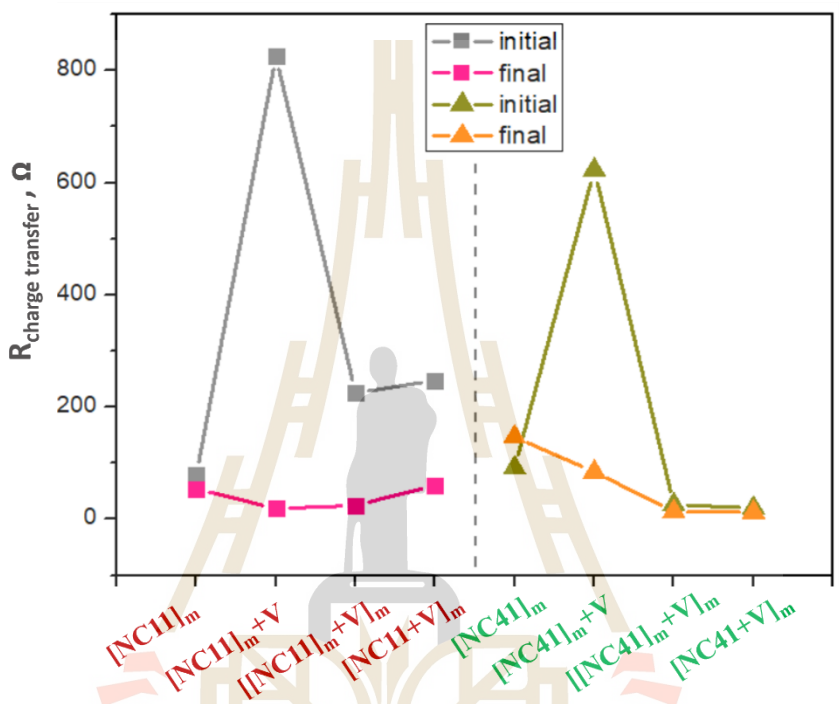

Figure 4.15 EIS measurements were compared initially and after testing.

In the samples of $[[NC11]_m +V]_m$, $[[NC41]_m +V]_m$, $[NCV11]_m$ and $[NCV41]_m$, the internal resistance values remained remarkably stable before and after measurement, with only a slight reduction observed following three cycles of CV testing. This stability is a clear indication that the incorporation of V_2O_5, followed by melt-quenching process, significantly strengthens the material's structure and enhances its durability. The consistency in resistance reflects the superior atomic arrangement and molecular bonding, which contribute to the material's remarkable resilience under stress (Cahill and Graeve, 2019). Such advanced resistive properties are crucial in minimizing energy loss within the battery, ultimately leading to enhanced performance and significantly extending the battery's lifespan. This promising outcome aligns perfectly with earlier

experimental findings, underscoring the material's potential for high-efficiency, long-lasting energy storage solutions.

4.6 The specific capacitance measurements of glass electrodes using cyclic voltammetry (CV).

The specific capacitance of the glass electrodes was evaluated using cyclic voltammetry (CV) measurements. This method provided insights into the electrochemical behavior of the electrodes, revealing any potential phase transitions during the testing process. Changes in the shape of the CV curves, especially at different scan rates, offered valuable information about phase transitions occurring within the glass materials, helping to assess their electrochemical stability and overall performance.

Additional insights from CV measurements were obtained using the same cell as the EIS measurements. EIS was measured first, followed by two CV cycles. The CV measurements started from the open-circuit potential of the cell, which was approximately 2.5 V, and the potential was swept between 2.0 V and 4.0 V at a scan rate of 0.5 mV/s. The results from the third CV cycle are shown in Figure 4.16, where (a and c) represents the Ni: Co ratio of 1:1 and (b and d) the Ni: Co ratio of 4:1. Here's the corrected version:

The CV graph represents the relationship between current density, which refers to the amount of electric current flowing through the electrode in an electrochemical system, and potential (V vs Li/Li^+), which measures the voltage during the intercalation and deintercalation of lithium ions (Li^+) into/from the electrode materials in the battery system. In Figure 4.16-4.17, the comparison with V_2O_5 (black line) highlights the phase transitions occurring within different glass systems. The characteristics of V_2O_5 exhibit well-defined redox peaks, indicating the intercalation of Li-ions into the material. One Li-ion intercalation process occurs between 3.0 and 3.5 V versus Li/Li^+. In the first three cycles shown in Figure 4.16-4.17, the 3^{th} cycle (Figure 4.18-4.19) clearly displays three

cathodic peaks at 3.31 V, 3.13 V, and 2.23 V, corresponding to the cathodic process of a redox reaction. This refers to the process occurring at the cathode of an electrochemical cell during reduction, involving electron acceptance and comprising three distinct steps.

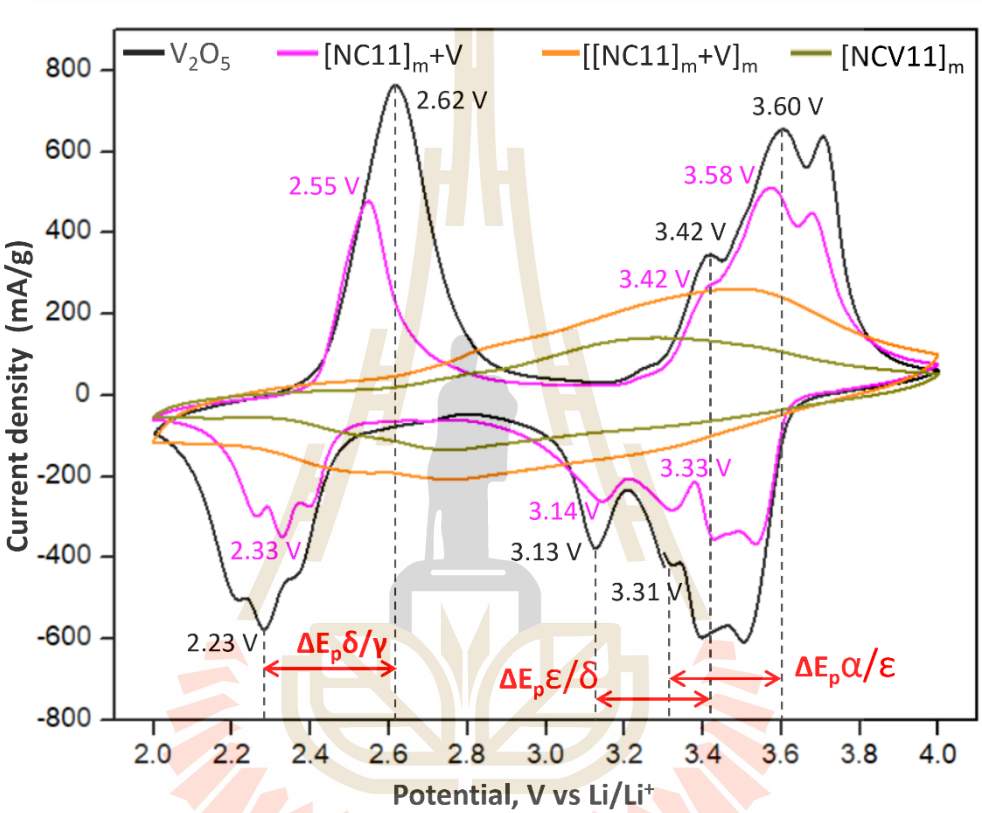

Figure 4.16 The coin cells with glass samples underwent three cycles of EIS measurements, followed by CV testing. The redox peak separation (ΔEp) for the third cycle of V_2O_5, $[NC11]_m$ +V, $[[NC11]_m$ +V$]_m$ and $[NCV11]_m$.

The first process involves the crystal phase transition from **α/ε** (**α**V_2O_5 to **ε**-Li0.5V_2O_5). **α**V_2O_5, or alpha-phase vanadium pentoxide, is the initial crystal structure of V_2O_5 in its stable **α**-phase. **ε**-Li0.5V_2O_5, or epsilon-phase lithium vanadium pentoxide, forms when lithium ions are intercalated into the structure of **α**-V_2O_5,

causing a change in the crystal structure to the ε-phase. In this phase, lithium ions are intercalated at a ratio of 0.5 lithium per V_2O_5.

The second process is the crystal phase transition from ε/δ (ε-LiV_2O_5 to δ-LiV_2O_5). In the epsilon-phase, lithium ions intercalate into the V_2O_5 structure at a ratio of 0.5 lithium per V_2O_5. δ-LiV_2O_5, or delta-phase, forms when additional lithium is inserted, reaching a ratio of 1 lithium per V_2O_5. The δ-phase is generally more stable and can accommodate more lithium ions compared to the ε-phase.

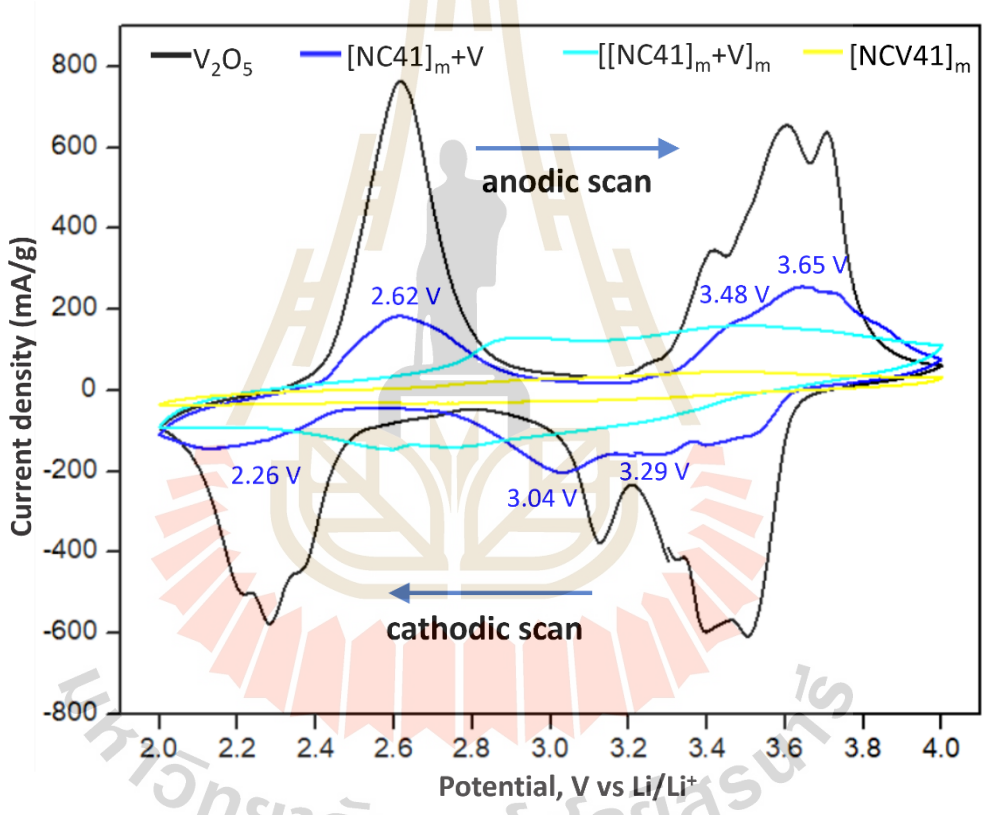

Figure 4.17 The redox peak separation (ΔEp) for the third cycle of $[NC41]_m$ +V, $[[NC41]_m$ +V$]_m$ and $[NCV41]_m$.

The third and final cathodic process is the δ/γ transition (δ-LiV_2O_5 to γ-$Li_2V_2O_5$), which refers to the crystal phase transition from the delta-phase to the gamma-phase. γ-$Li_2V_2O_5$, or gamma-phase, occurs when further lithium ions are intercalated, reaching a ratio of 2 lithium ions per V_2O_5. This phase change leads to the formation of the γ-

phase, which can support even more lithium ions than the δ-phase, resulting in higher capacity. However, this may also alter the structure compared to the previous phase (Armer et al., 2018; Wang, Chen, Xu, Wang, and Zhen, 2017).

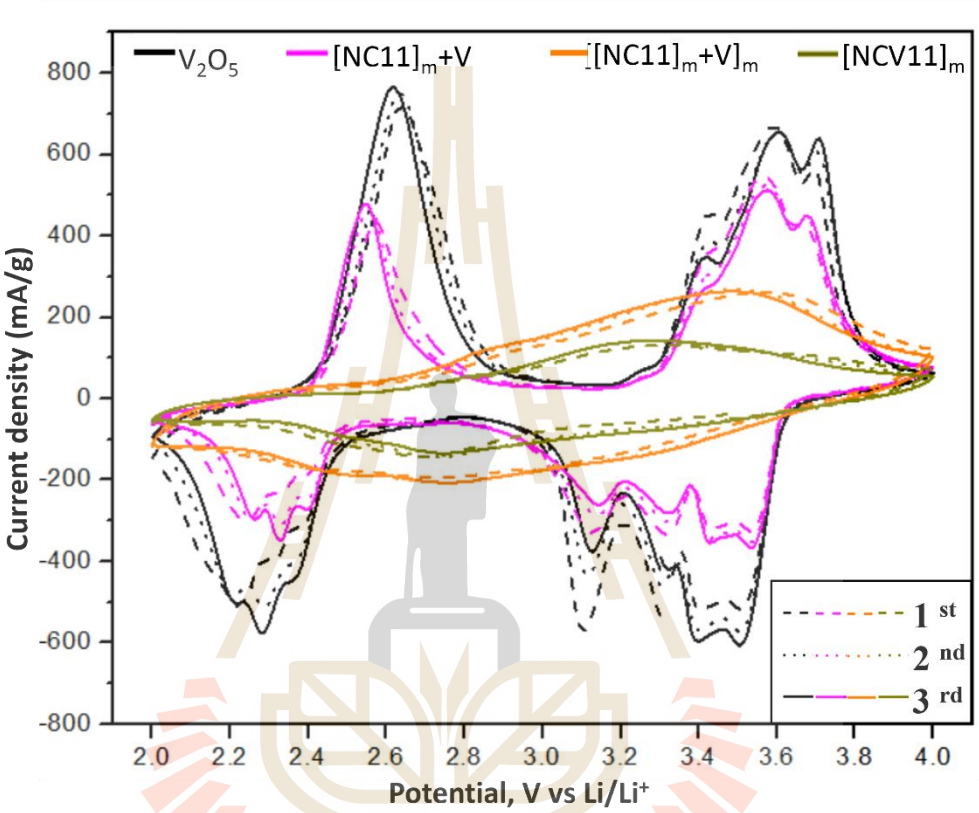

Figure 4.18 The graph displays CV data from the first to third cycles of V_2O_5, $[NC11]_m$ +V, $[[NC11]_m +V]_m$ and $[NCV11]_m$.

Simultaneously, three corresponding anodic peaks were observed at 2.62, 3.42, and 3.60 V, indicating the anodic process of the redox reactions on the anode. These peaks correspond to oxidation reactions occurring at the anode in the electrochemical cell, demonstrating good reversibility of the electrode. The separation of the redox peaks (ΔEp) for the α/ε, ε/δ, and δ/γ phase transitions in V_2O_5 were calculated to be 0.29, 0.29, and 0.39 V, respectively (Figure 4.16). A smaller potential difference suggests

more favorable Li^+ insertion/extraction reactions and highlights the importance of phase transition kinetics within the material.

In the $[NC11]_m$ +V sample, three distinct cathodic peaks were clearly observed at 3.33, 3.14, and 2.33 V, along with three anodic peaks at 3.58, 3.42, and 2.55 V. From Figure 4.18, the redox peak separations (ΔEp) for the **α/ε**, **ε/δ**, and **δ/γ** transitions in $[NC11]_m$ +V were calculated as 0.25, 0.28, and 0.22 V, respectively. For the $[NC41]_m$ +V sample, the redox peaks were less distinct, though three cathodic peaks were observed at 3.29, 3.04, and 2.26 V, and three anodic peaks at 3.65, 3.48, and 2.62 V. The redox peak separations (ΔEp) for $[NC41]_m$ +V were calculated as 0.36, 0.44, and 0.36 V, respectively, as shown in Figure 4.18.

For samples incorporating V_2O_5 into the glass system and then undergoing a subsequent firing process, no clear redox peaks corresponding to V_2O_5 were observed, as shown in Figure 4.16-4.17. However, a significant reduction in current density was noted. In batteries, lower current density implies reduced current flow through the energy storage system. The current density for $[[NC11]_m$ +V$]_m$ was higher than [NC11 +V$]_m$, and similarly, the current density for $[[NC41]_m$ +V$]_m$ was higher than [NC41 +V$]_m$, though V_2O_5 still exhibited the highest current density. This suggests that these four samples exhibited lower current flow through the energy storage material, possibly due to operation under low current load conditions. Adjusting the current to lower values helps conserve energy and prevents unnecessary energy loss during battery operation. Lower current density generally extends the battery's lifespan and enhances energy conservation during daily use, with [NC11 +V$]_m$ and [NC41 +V$]_m$ showing the lowest values, consistent with the CV results. Reducing the fluctuations in Li^+ insertion/extraction reactions within the material helps minimize energy loss during the battery's charge-discharge processes. This energy conservation also contributes to extending the battery's lifespan and maintaining capacity over the long term.

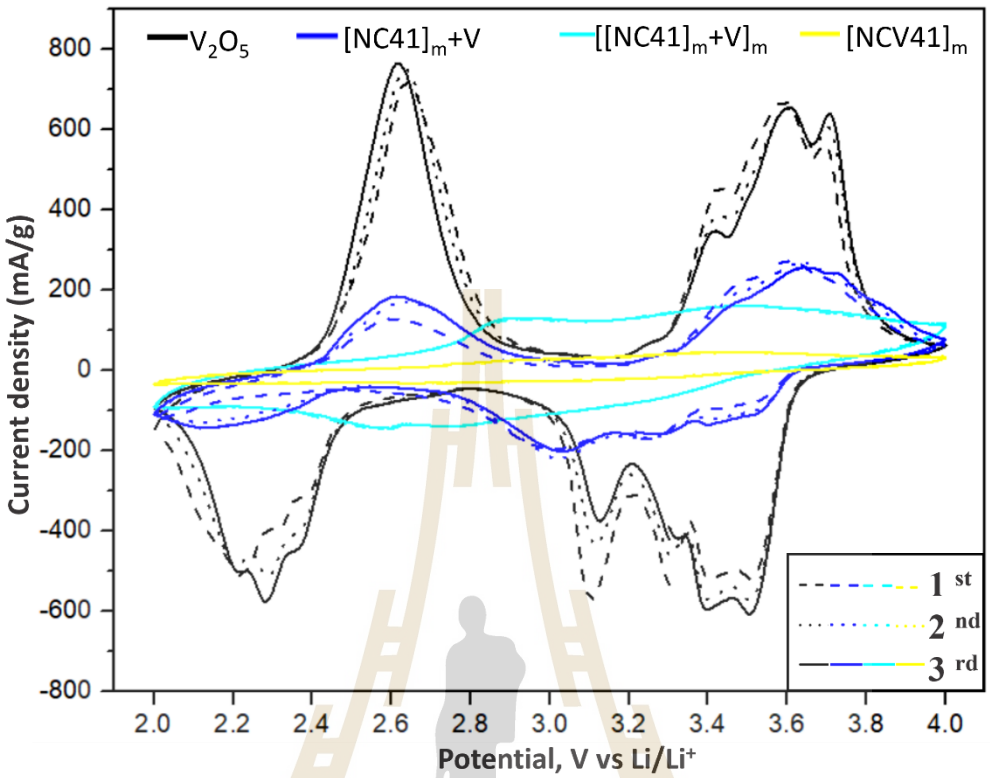

Figure 4.19 The graph displays CV data from the first to third cycles of V_2O_5, $[NC41]_m$ +V, $[[NC41]_m$ +V$]_m$ and $[NCV41]_m$.

Additionally, the CV curves in Figure 4.18-4.19 represent cycles 1–3 (excluding the initial cycle due to damaged initial graphs in each sample, which were not used for comparison). As shown, the curves for V_2O_5, $[NC11]_m$ +V, and $[NC41]_m$ +V in cycles 1, 2, and 3 exhibit noticeable changes in the CV profile and redox peak positions. However, for $[[NC11]_m$ +V$]_m$, $[[NC41]_m$ +V$]_m$, $[NC11$ +V$]_m$ and $[NC41$ +V$]_m$, as displayed in Figure 4.18-4.19. The curves nearly overlap from cycles 1 to 3 in terms of peak positions and intensities, indicating good stability and reversibility of the electrodes. This aligns with the battery capacity and Capacity Retention (%) measurements, emphasizing the importance of stability in maintaining battery performance over the long term. Materials that exhibit good Li^+ insertion/extraction behavior tend to degrade more slowly and retain capacity more effectively (Siriroj et al., 2024).

Additionally, the electrochemical performance was evaluated by determining the specific capacity from the cyclic voltammograms (CCV) of the glass electrode, calculated using the following equation (Khajonrit et al., 2018).

$$C_{CV} = \frac{1}{vm\Delta V} \int IdV \qquad \text{Equation 4.4}$$

where V is the scan rate (mV/s), m is the active material mass (g), ΔV is the potential window (V), and I is the current response (A). The specific capacity of the glass samples, calculated from the area under the CV curve at a scan rate of 0.5 mV/s, is presented in Figure 30e, while the energy density can be calculated and the results are shown in Figure 30f. However, the specific capacity is only reported for cycles 1 through 3.

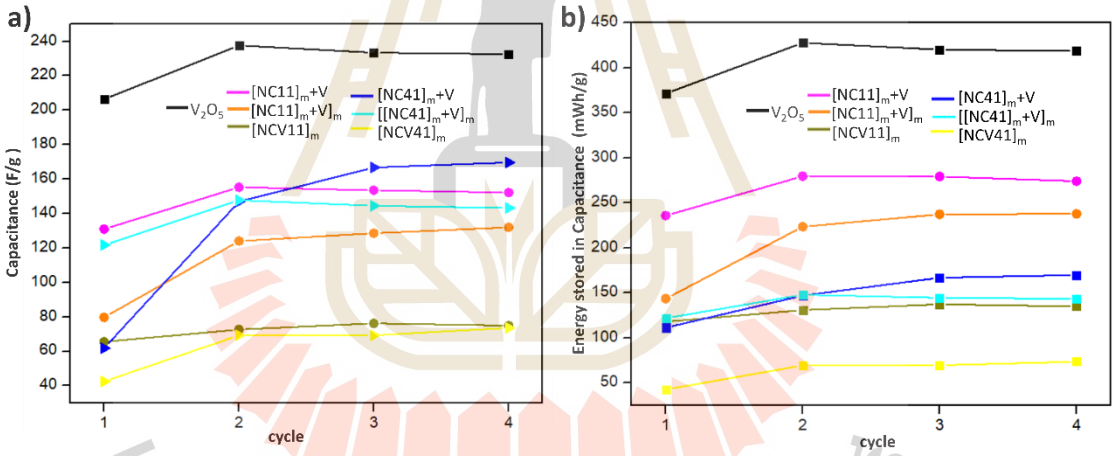

Figure 4.20 a) The capacitance and b) energy density values were measured, with a consistent scan rate of 0.5 mV/s throughout the experiment.

4.7 X-ray Absorption Near Edge Structure (XANES)

X-ray Absorption Near Edge Structure (XANES) is a powerful technique used to probe the electronic structure and local environment of atoms in a material. It focuses on the near-edge region of an X-ray absorption spectrum, typically within 50 eV of the absorption edge, providing detailed information about oxidation states, coordination geometry, and electronic transitions. XANES is particularly useful in studying the

chemical state of elements within complex systems, such as battery electrodes, catalysts, and other functional materials. By analyzing the fine structure near the absorption edge, researchers can gain insights into the local bonding environment and electronic configuration of specific atoms, helping to understand the material's properties and behavior under different conditions.

4.7.1 Verification of Oxidation States in Nickel-Mixed Glass Samples Using X-ray Absorption Near Edge Structure (XANES) Analysis

The glass sample was analyzed using X-ray Absorption Spectroscopy (XAS). The sample, prepared from a new glass film that had not yet been assembled into a coils cell, was utilized to measure the X-ray Absorption Near Edge Structure (XANES) spectrum. All glass samples were assessed for X-ray absorption in the XANES region of Ni at the K-edge, with photon energy at 409.9 ± 0.2 eV, employing transmission mode. The data obtained were processed using Athena software, yielding two forms of XANES spectra: the Normalized Spectrum and the First Derivative Spectrum, as illustrated in Figure 4.21.

From these spectra, the slope of the Normalized Spectrum and the peak position of the First Derivative Spectrum were analyzed to determine the absorption edge energy of Ni-glass in comparison to standard materials, as detailed in Table 4.3. This table reveals that nickel in the glass samples is predominantly present in the forms of Ni^{2+} and Ni^{3+}.

Furthermore, the concentrations of these oxidation states provide valuable insights into the electronic environment of nickel within the glass matrix, which can influence the material’s properties, such as conductivity and thermal stability. The average oxidation state of nickel ions in the glass samples was calculated using equations 4.5-4.7. These calculations are crucial for understanding the role of nickel in the overall glass structure and its potential applications in advanced materials and devices (Daengsakul et al., 2015).

$$\langle \%\ \text{of}\ N^{3+} \rangle = \left[\frac{\Delta E \text{ of sample}}{\Delta E \text{ of } Ni^{3+} \text{ and } Ni^{2+}} \right] \times 100 \qquad \text{Equation 4.5}$$

$$\langle \%\ \text{of}\ N^{2+} \rangle = \left[1 - \frac{\Delta E \text{ of sample}}{\Delta E \text{ of } Ni^{3+} \text{ and } Ni^{2+}} \right] \times 100 \qquad \text{Equation 4.6}$$

$$\langle \text{Ni oxidation state} \rangle = 3 \left[\frac{\Delta E \text{ of sample}}{\Delta E \text{ of } Ni^{3+} \text{ and } Ni^{2+}} \right] + 2 \left[1 - \frac{\Delta E \text{ of sample}}{\Delta E \text{ of } Ni^{3+} \text{ and } Ni^{2+}} \right] \qquad \text{Equation 4.7}$$

Table 4.3 Position of X-ray absorption of Ni-glass with standard material.

Sample of standard	Peak Position (eV)	Sample	Peak Position (eV)	Sample	Peak Position (eV)
NiO: 2+ (Calculate)	8343.20	**$[NC11]_m$**	8344.88	**$[NC41]_m$**	8343.36
$Ni(OH)_2$: 2+ (Standard)	8344.55	**$[NC11]_m$+V**	8344.67	**$[NC41]_m$+V**	8344.95
Li_2NiBO_4: 3+ (Standard)	8348.52	**$[NC11]_m$+V$]_m$**	8344.98	**$[NC41]_m$+V$]_m$**	8345.38
		[NC11+V$]_m$	8346.03	**[NC41+V$]_m$**	8345.13

Table 4.3 displays the average oxidation state calculations for the glass samples. It was found that the oxidation state of nickel in the glass is predominantly Ni^{2+} rather than Ni^{3+}, indicating a higher concentration of Ni^{2+} ions in the samples. This suggests that the nickel in the glass remains in a lower oxidation state compared to Ni^{3+}. The prevalence of Ni^{2+} over Ni^{3+} is likely due to the glass matrix composition and its stabilizing effect on Ni^{2+} ions, which favors this lower oxidation state.

The presence of a greater amount of Ni^{2+} ions can significantly influence the chemical and physical properties of the glass, such as its color, electronic conductivity, and thermal stability. For instance, Ni^{2+} ions often contribute to a more intense color

in glass materials, while also potentially enhancing its durability and resistance to thermal stress. The predominance of Ni^{2+} can also affect the glass structure at the atomic level, leading to variations in network connectivity and, consequently, the material's mechanical properties.

However, the differences in oxidation states are not substantial, as indicated by the ΔE, which represents the energy difference at the absorption edge. This relatively small ΔE between Ni^{2+} and Ni^{3+} (5.32 eV) suggests that only minor changes occur in the electronic structure, without significantly altering the glass's overall stability. Consequently, the Ni^{2+}-rich composition likely stabilizes the glass matrix, providing a beneficial balance between enhanced physical properties and controlled electronic behavior.

Table 4.4 Average oxidation numbers of nickel ions in glass samples.

Sample	*ΔE of sample (eV)	%(Ni^{2+})	%(Ni^{3+})	Average oxidation number
$[NC11]_m$	1.68	68.42	31.58	2.32
$[NC11]_m$+V	1.47	72.37	27.63	2.28
$[NC11]_m$+V$]_m$	1.78	66.54	33.46	2.33
[NC11+V$]_m$	2.60	51.13	48.87	2.49
$[NC41]_m$	0.16	96.99	3.01	2.03
$[NC41]_m$+V	1.75	67.11	32.89	2.33
$[NC41]_m$+V$]_m$	2.18	59.02	40.98	2.41
[NC41+V$]_m$	1.93	63.72	36.28	2.36

*The ΔE for Ni^{2+} and Ni^{3+} is 5.32 eV.

*ΔE represents the energy difference at the absorption edge.

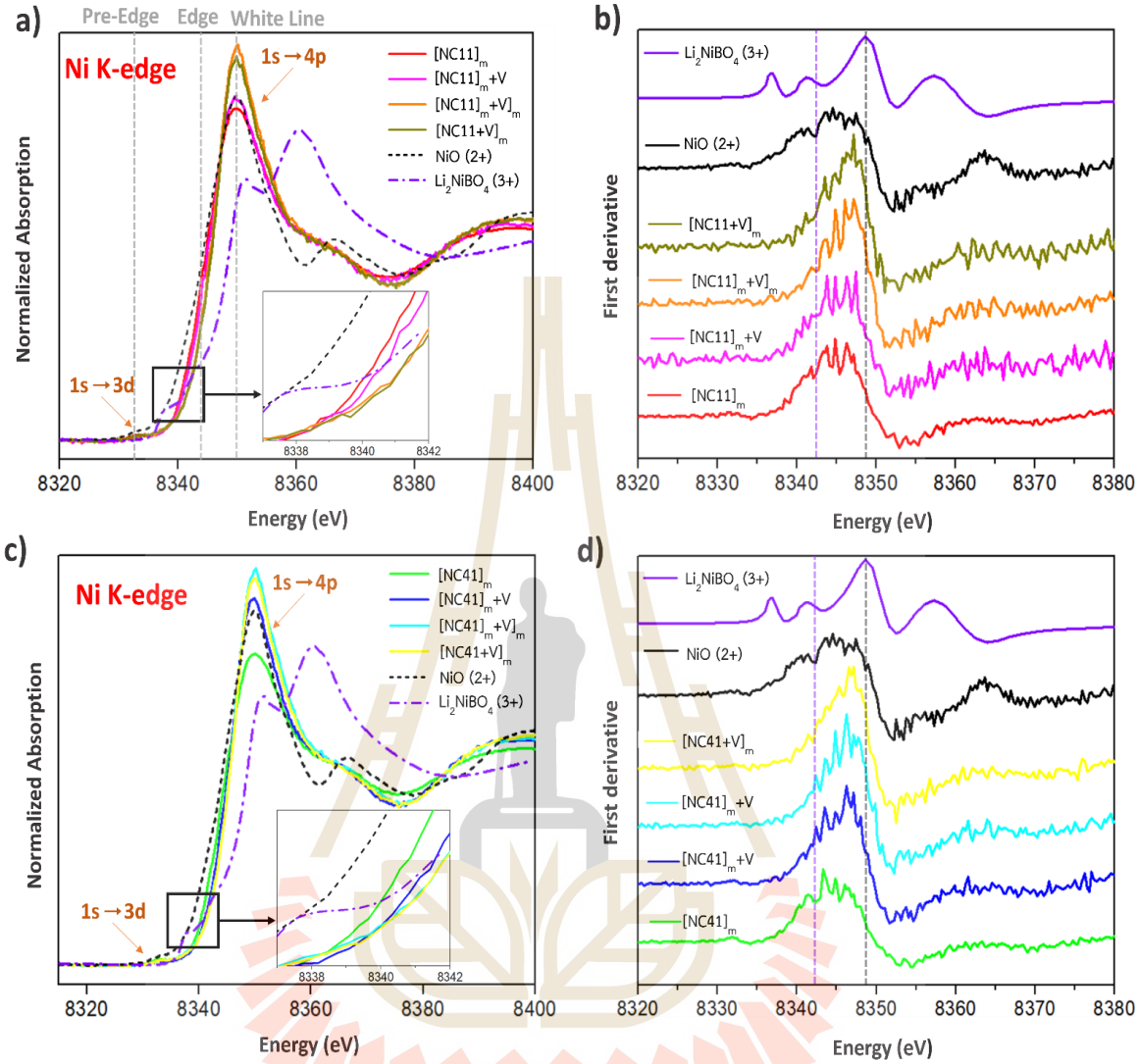

Figure 4.21 XANES spectrum a,c) Normalized Spectrum b,d) First Derivative Spectrum.

4.7.2 Verification of Oxidation States in Cobalt-Mixed Glass Samples Using X-ray Absorption Near Edge Structure (XANES) Analysis

Each glass sample was analyzed for X-ray absorption in the XANES range of Co at the K-edge, using photons with energy of 7709.0 ± 0.2 eV in transmission mode. The obtained data were analyzed with the Athena software, resulting in two distinct XANES spectra, as shown in Figure 4.22. The absorption edge position in the glass samples

closely matches the absorption position of the reference standards, as presented in Table 4.5.

Table 4.5 Position of X-ray absorption of Co-glass with standard material.

Sample of standard	Absorption position (eV)	Sample	Absorption position (eV)	Sample	Absorption position (eV)
CoO: 2+	7717.49	$[NC11]_m$	7717.69	$[NC41]_m$	7718.04
Co_3O_4: 2+,3+	7721.63	$[NC11]_m$+V	7718.19	$[NC41]_m$+V	7718.31
		$[NC11]_m$+V$]_m$	7718.00	$[NC41]_m$+V$]_m$	7718.30
		[NC11+V$]_m$	7718.81	[NC41+V$]_m$	7718.74

In order to calculate the average oxidation state of Co atoms, it is can be determined by comparing with the known standard sample as seen in Eq 4.8.

$$\langle \text{Co oxidation state} \rangle = 2.66 \left[\frac{\Delta E \text{ of sample}}{\Delta E \text{ of } Co^{2+/3+} \text{ and } Co^{2+}} \right] + 2 \left[1 - \frac{\Delta E \text{ of sample}}{\Delta E \text{ of } Co^{2+/3+} \text{ and } Co^{2+}} \right] \quad \text{Equation 4.8}$$

After calculating the average oxidation state for the glass samples presented in Table 4.6, it was found that the glass contains cobalt primarily in the oxidation states of Co^{2+} and $Co^{2+/3+}$. The results indicate that cobalt ions in the glass samples are predominantly in the Co^{2+} state rather than $Co^{2+/3+}$ suggesting a higher proportion of Co^{2+} ions over Co^{3+} ions. This finding implies that cobalt in the glass is mainly in a lower oxidation state, which can influence the chemical and physical properties of the glass, such as its structure, energy transfer capabilities, and material stability. The higher presence of Co^{2+} over Co^{3+} also reflects a chemical environment that favors nickel remaining in a lower oxidation state.

Table 4.6 Average oxidation numbers of cobalt ions in glass samples.

Sample	*ΔE of sample (eV)	%(Co^{2+})	%($Co^{2+/3+}$)	Average oxidation number
$[NC11]_m$	0.20	95.17	5.14	2.03
$[NC11]_m$+V	0.70	83.09	17.99	2.11
$[NC11]_m$+V$]_m$	0.51	87.68	13.11	2.08
[NC11+V$]_m$	1.32	68.12	33.92	2.21
$[NC41]_m$	0.55	86.71	14.14	2.09
$[NC41]_m$+V	0.82	80.19	21.07	2.13
$[NC41]_m$+V$]_m$	0.81	80.43	20.82	2.13
[NC41+V$]_m$	1.25	69.81	32.13	2.20

*ΔE of Co^{2+} and $Co^{2+/3+}$ = 4.14 eV

In Figure 4.22a, the Ni/Co-doped LBO glass and the reference NiO absorption spectrum at the Ni K-edge XANES are displayed. All Ni/Co-doped LBO glass samples show an absorption edge shift to higher energy compared to standard NiO, as noted by the main edge jump highlighted in the inset. Since the oxidation state of Ni in NiO is 2+, this shift suggests that the Ni in the glass samples has an oxidation state higher than 2+, as confirmed by the peak of the first derivative of the data (Figure 4.22b). For Co oxidation state analysis, Co_3O_4 and CoO standards were utilized to examine the Co K-edge XANES spectra in Figures 4.22 c and d. The research findings indicate that the glass spectra align with those of CoO (Co^{2+} oxidation) and Co_3O_4 (Co^{3+}), suggesting a mixed oxidation state of Co^{2+} and Co^{3+} in the Ni/Co-doped LBO glass. Additionally, linear combination fitting analysis using Athena software shows that approximately 55% of Co in the glass exists in the Co^{2+} phase, varying slightly depending on specific conditions.

This variation in Co^{2+} concentration could impact the electronic structure and potentially enhance the glass's catalytic properties. The mixed oxidation states of Ni and Co likely contribute to increased stability and conductivity in the glass matrix. This

detailed oxidation state analysis highlights the potential of Ni/Co-doped LBO glasses for applications that benefit from tailored electronic and structural characteristics.

The XANES analysis revealed that cobalt in Ni/Co-doped LBO glasses predominantly exists in the Co^{2+} state, with mixed oxidation states contributing to the material's stability and conductivity. Nickel was found to have a higher oxidation state than NiO, further influencing the electronic structure of the glass. These findings highlight the potential of Ni/Co-doped LBO glasses for applications requiring enhanced catalytic and electronic properties.

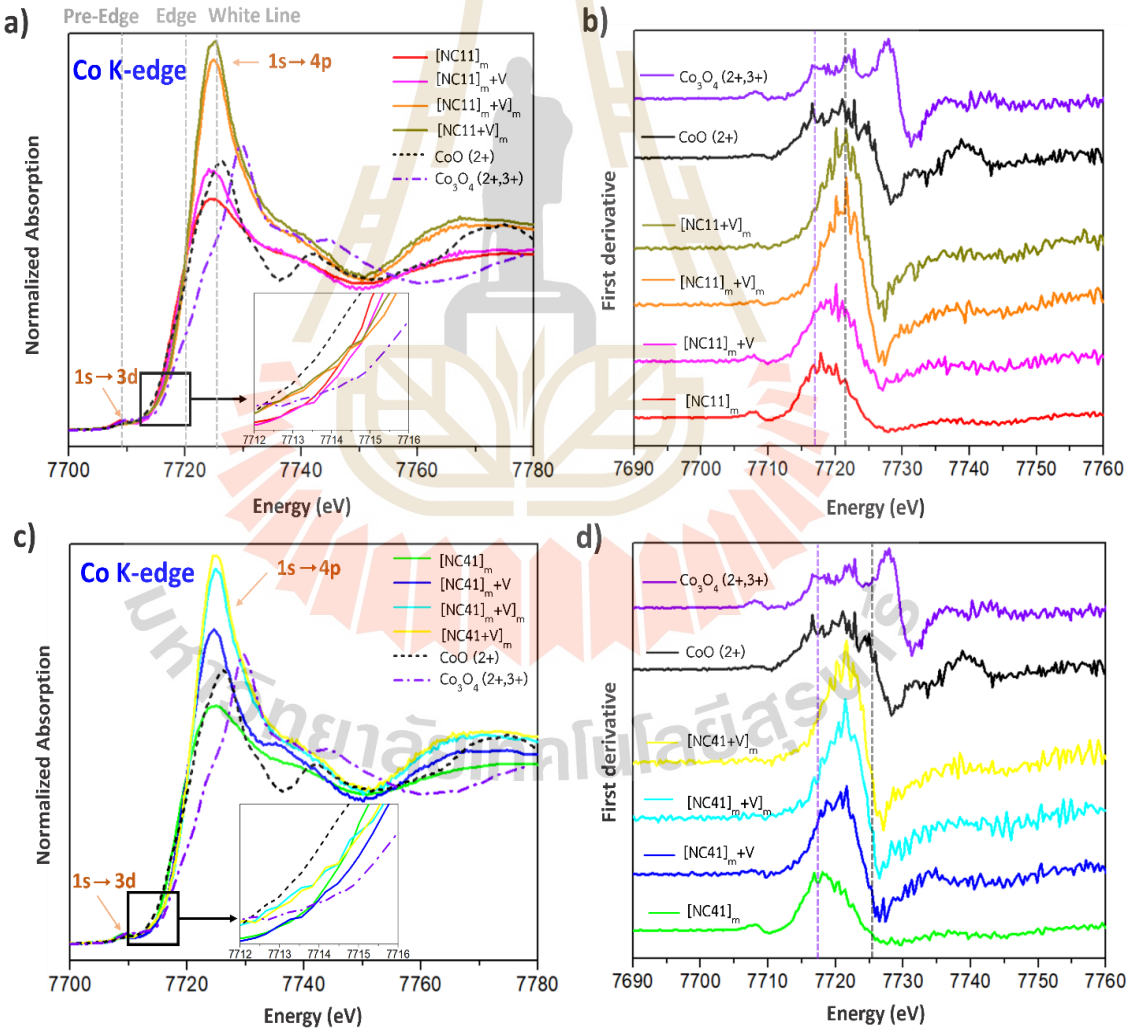

Figure 4.22 XANES spectrum a,c) Normalized Spectrum b,d) First Derivative Spectrum.

4.7.3 Verification of Oxidation States in Vanadium-Mixed Glass Samples Using X-ray Absorption Near Edge Structure (XANES) Analysis

All glass samples were analyzed for X-ray absorption in the V K-edge XANES range using photons with an energy of 5465.0 ± 0.2 eV, measured in transmission mode. The resulting data was processed using the Athena software, yielding two distinct XANES spectra, as shown in Table 4.7. The absorption edge positions of the glass samples, compared to standard compounds, are listed in Table 8, with edge positions lying between those of VO_2 and V_2O_5. This indicates that the glass samples contain vanadium in mixed oxidation states of V^{4+} and V^{5+}.

To calculate the average oxidation state of vanadium atoms, a comparison with known standard samples can be used, as demonstrated in Equation 4.9.

$$\langle \text{V oxidation state} \rangle = 5\left[\frac{\Delta E \text{ of sample}}{\Delta E \text{ of } V^{5+} \text{ and } V^{4+}}\right] + 4\left[1 - \frac{\Delta E \text{ of sample}}{\Delta E \text{ of } V^{5+} \text{ and } V^{4+}}\right] \quad \text{Equation 4.9}$$

Table 4.7 Position of X-ray absorption of V-glass with standard material.

Sample of standard	Absorption position (eV)	Sample	Absorption position (eV)	Sample	Absorption position (eV)
V_2O_3: 3+	5479.88	$[NC11]_m$+V	5481.54	$[NC41]_m$+V	5481.51
VO_2: 4+	5480.63	$[NC11]_m$+V]$_m$	5481.37	$[NC41]_m$+V]$_m$	5481.22
V_2O_5: 5+	5481.77	[NC11+V]$_m$	5481.24	[NC41+V]$_m$	5481.21

The glass samples were found to contain a higher amount of V^{5+} compared to V^{4+}, with the average oxidation state of vanadium shown in Table 4.8. The presence of V^{5+} in the glass samples aligns with the findings of (Nibel, Schmidt, and Gubler, 2014), indicating that vanadium in these samples primarily exists in a high oxidation state (V^{5+}).

This suggests that vanadium in the glass has undergone significant electron loss. The higher proportion of V^{5+} relative to V^{4+} can influence the chemical properties of the glass. The dominance of V^{5+} in the glass matrix may contribute to enhanced catalytic properties and greater stability under oxidative conditions. Additionally, the higher oxidation state could affect the glass's electronic structure, potentially improving its conductivity and suitability for advanced applications.

Table 4.8 Average oxidation numbers of vanadium ions in glass samples.

Sample	*ΔE of sample (eV)	%(V^{4+})	%(V^{5+})	Average oxidation number
$[NC11]_m$+V	0.91	20.18	79.82	4.80
$[NC11]_m$+V$]_m$	0.74	35.09	64.91	4.65
[NC11+V$]_m$	0.61	46.49	53.51	4.54
$[NC41]_m$+V	0.88	22.81	77.19	4.77
$[NC41]_m$+V$]_m$	0.59	48.25	51.75	4.52
[NC41+V$]_m$	0.58	49.12	50.88	4.51

*ΔE of $V^{4+}$and V^{5+} = 1.14 eV

According to the XANES data, nearly all vanadium compounds exist predominantly as V5+ upon synthesis and are reduced to V^{4+} during testing. The oxidation state may change as indicated by the XRD data, which suggests structural modifications that occur when lithium ions are transported from the cathode to the anode during the charging process. As a result of this ion transport, vanadium undergoes further oxidation, transitioning from V^{4+} to V^{5+}.

During discharging, there is a noticeable low-energy shift in the absorption curves, which revert to their original position upon recharging. The pre-edge feature corresponds to the dipole-forbidden 1s to 3d transition, whereas the post-edge peak is associated with the dipole-allowed 1s to 4p transition. Changes in the dipole-forbidden transition typically have low intensity or may not be visible in the spectrum,

while the dipole-allowed transition generally exhibits high intensity and is easily observable. The intensity of the pre-edge feature is sensitive to the valence state of the central vanadium atoms, the coordination environment, and the symmetry of the polyhedron. The energy position of the post-edge peak, or white line, reflects the valence state of the central vanadium atoms.

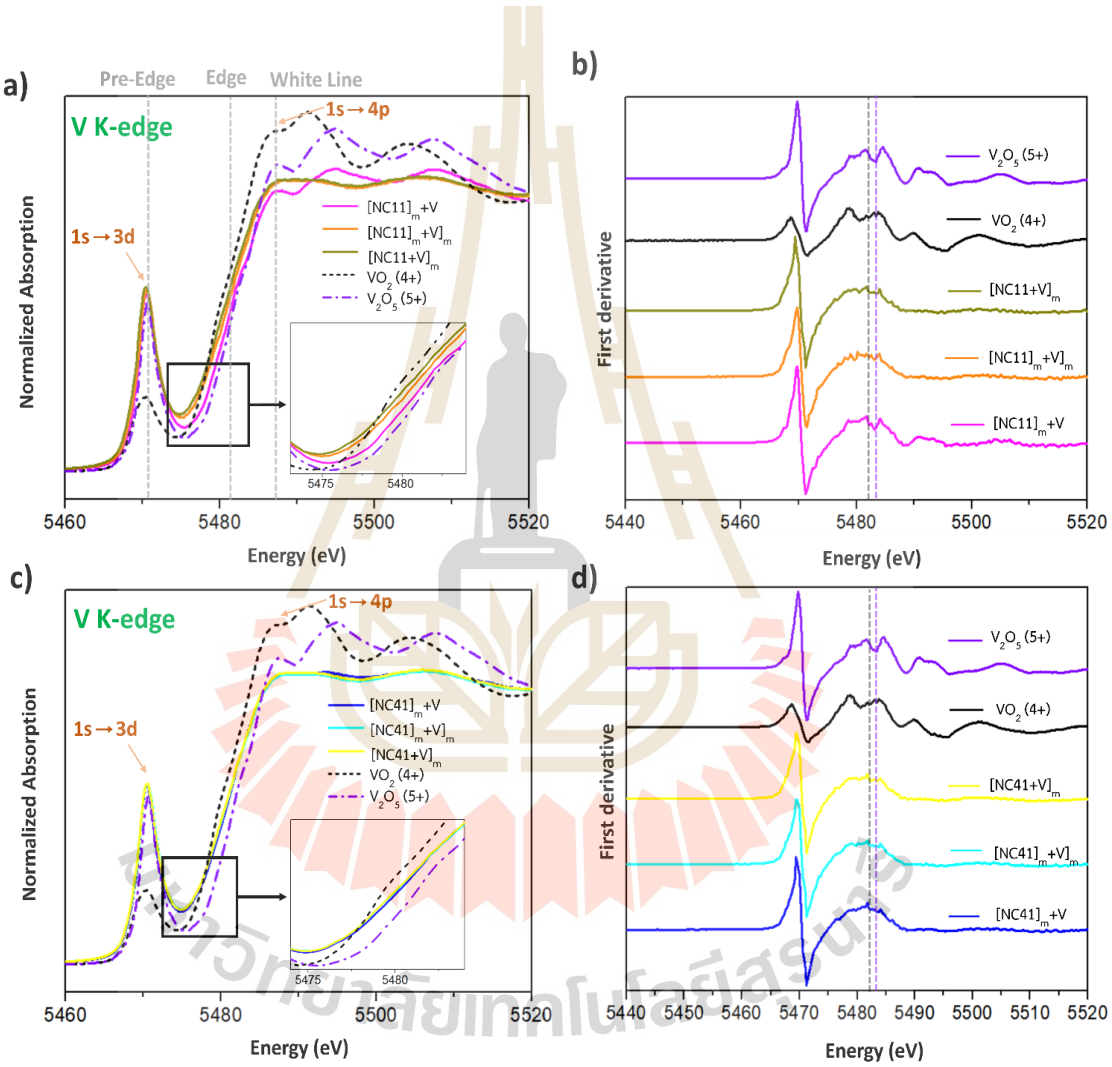

Figure 4.23 XANES spectrum a,c) Normalized Spectrum b,d) First Derivative Spectrum.

In the discharge process of lithium-ion batteries, XANES spectra reveal a decrease in the intensity of the pre-edge peak and an increase in the post-edge peak intensity. The reduction in the pre-edge peak intensity is attributed to an increase in the occupancy of vanadium d orbitals due to lithium insertion, which enhances the

symmetry of the vanadium ions in the VO_5 structure during discharge. The energy position of the post-edge peak also signifies a decrease in the oxidation state of vanadium ions, indicating that the vanadium ions receive electrons from lithium insertion, thereby reducing their oxidation state.

4.8 X-ray Absorption Fine Structure (EXAFS)

X-ray Absorption Fine Structure (EXAFS) is a powerful spectroscopic technique used to investigate the local structure around specific absorbing atoms in a material. This method involves measuring the absorption of X-rays as a function of energy, allowing researchers to obtain detailed information about the coordination environment, bond lengths, and the type of neighboring atoms surrounding the absorbing species. EXAFS provides insights into the structural and electronic properties of various materials, making it invaluable in fields such as materials science, chemistry, and solid-state physics. By analyzing the oscillatory features in the absorption spectrum, scientists can derive quantitative information regarding atomic distances and the disorder within a sample, facilitating a deeper understanding of the material's behavior and interactions at the atomic level.

4.8.1 X-ray Absorption Fine Structure (EXAFS) Analysis of Nickel-Mixed Glass Samples

The sample was analyzed by measuring the X-ray absorption spectrum in the Extended X-ray Absorption Fine Structure (EXAFS) region at the Ni K absorption edge using photons with an energy of 409.9 ± 0.2 eV in transmission mode. The data obtained were initially processed with the Athena software and subsequently analyzed further with Artemis. Additionally, crystal data for Lithium Cobalt Nickel Oxide (Li_2CoNiO_4), expected to form within the glass sample, were downloaded from the Materials Project website using the model Li_2CoNiO_4-mp-753536. The corresponding structure is shown in Figure 4.24.

Li_2CoNiO_4 crystallizes in the orthorhombic Imma space group, with a structure derived from beta polonium. The material features two inequivalent Li^{1+} sites, both forming LiO_6 octahedra that share corners and edges with CoO_6 and NiO_6 octahedra. The octahedral tilt angles range between 5-9°, and bond lengths for Li-O, Co-O, and Ni-O vary slightly, reflecting slight distortions in the structure. Co^{4+} and Ni^{2+} are both coordinated by six O^{2-} atoms, forming CoO_6 and NiO_6 octahedra. There are two distinct O^{2-} sites, each involved in bonding to Li^{1+}, Co^{4+}, and Ni^{2+}, forming complex edge- and corner-sharing octahedra.

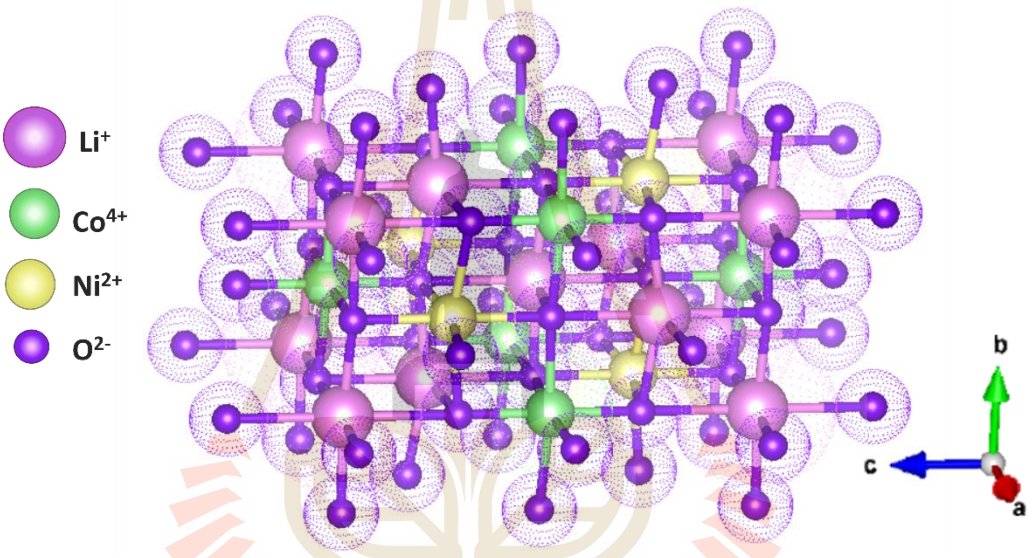

Figure 4.24 Crystal structures of Li_2CoNiO_4 Model: mp-753536.

Li_2CoNiO_4 (CAS number: 753536) is a compound that typically crystallizes in a layered oxide structure, where lithium ions (Li^+) are intercalated between layers of metal oxides formed by cobalt (Co) and nickel (Ni). The structure of this material is similar to other layered lithium transition metal oxides, such as $LiCoO_2$ or $LiNiO_2$, which are commonly used in battery applications due to their ability to reversibly insert and remove lithium ions.

In the Li_2CoNiO_4 model, cobalt and nickel ions occupy octahedral sites in a mixed transition metal oxide framework. This creates a strong bonding network with oxygen atoms (O^{2-}) that form a closely packed lattice. The lithium ions, which are

relatively mobile, can move between these layers, making this material potentially useful for electrochemical applications such as lithium-ion batteries.

Using the crystal structure data, the program identifies the scattering paths of atoms surrounding nickel, the absorber, and fits these paths to the experimental data from the glass sample. In this fitting process, only single scattering paths with high amplitude are selected, as lower amplitude paths have minimal impact on the R-factor, a statistical measure of the difference between the model and experimental data. Once the fitting is complete, the Fourier-transformed EXAFS spectrum of the NiO-doped glass sample is obtained, as illustrated in Figure 4.25.

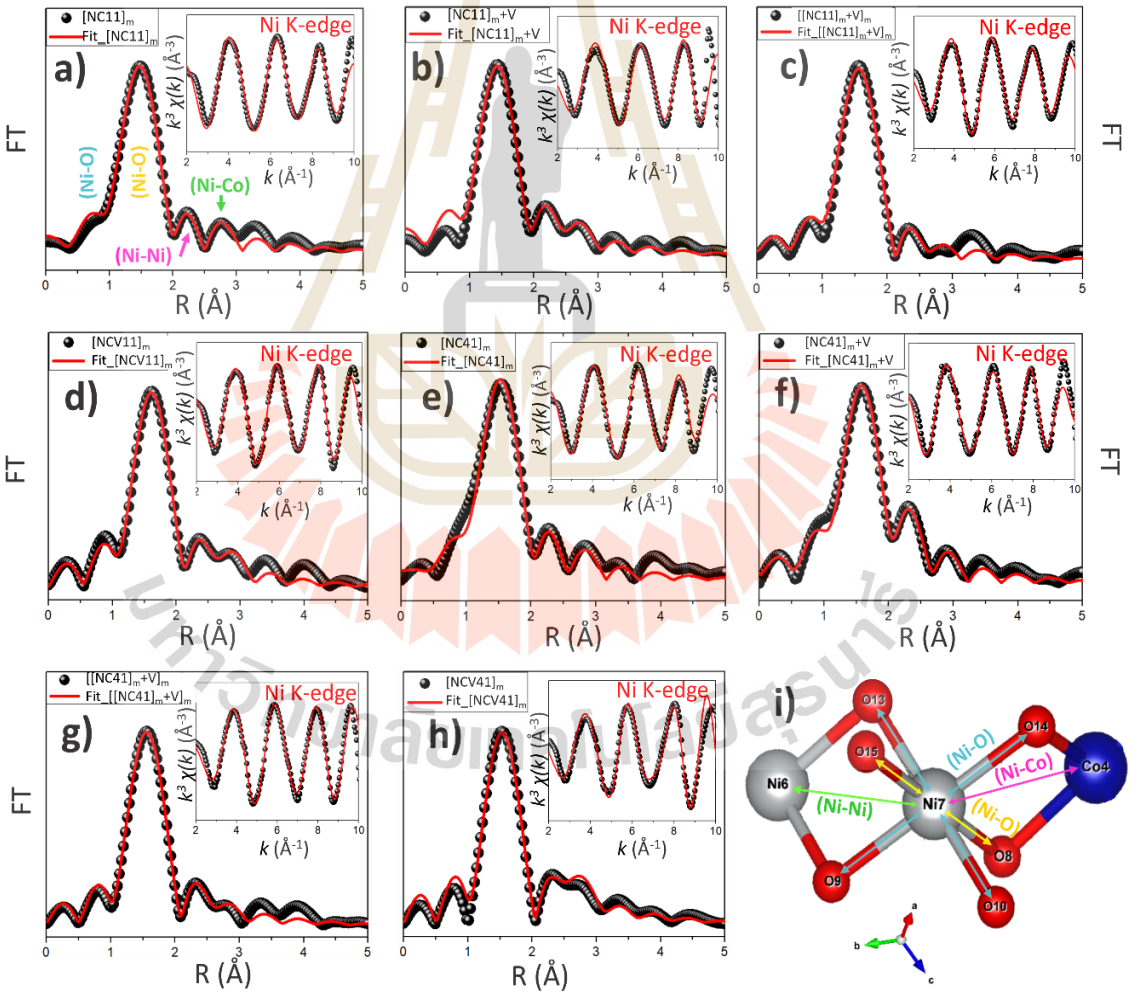

Figure 4.25 a-h) EXAFS spectra and fitting at Ni K-edge of sample. i) The model used to observe the atomic distances.

Table 4.9 Presents the optimal fitting parameters for the NiO-doped glass sample compared with data from Li_2CoNiO_4.

Sample	Paths	N	S_0^2	σ^2	R (A^o)	ΔE_0 (eV)	R-factor
$[NC11]_m$	Ni-O	6	0.737	0.00504	2.04159	-2.923	0.0118621
	Ni-Ni	2	0.737	0.02809	2.45422		
	Ni-Co	4	0.737	0.06502	2.69255		
$[NC11]_m$+V	Ni-O	6	1.000	0.00758	2.06955	-2.218	0.0040836
	Ni-Ni	2	1.000	0.00743	2.53744		
	Ni-Co	4	1.000	0.02114	2.78758		
$[NC11]_m$+V$]_m$	Ni-O	6	1.000	0.00416	2.07267	-0.767	0.0054326
	Ni-Ni	2	1.000	0.00742	2.48465		
	Ni-Co	4	1.000	0.01404	2.69021		
$[NC11+V]_m$	Ni-O	6	1.000	0.00510	2.05305	-4.330	0.0046821
	Ni-Ni	2	1.000	0.01035	2.53507		
	Ni-Co	4	1.000	0.02042	2.79672		
$[NC41]_m$	Ni-O	6	0.950	0.01018	2.05467	-2.479	0.0139459
	Ni-Ni	2	0.950	0.01587	2.40212		
	Ni-Co	4	0.950	0.02233	2.60948		
$[NC41]_m$+V	Ni-O	6	1.000	0.00587	2.04330	-4.196	0.0018229
	Ni-Ni	2	1.000	0.01162	2.46637		
	Ni-Co	4	1.000	0.02747	2.78699		
$[NC41]_m$+V$]_m$	Ni-O	6	1.000	0.00681	2.05599	-2.112	0.0038975
	Ni-Ni	2	1.000	0.01025	2.50072		
	Ni-Co	4	1.000	0.02190	2.80499		
$[NC41+V]_m$	Ni-O	6	1.000	0.00512	2.00044	-9.677	0.0077284
	Ni-Ni	2	1.000	0.00536	2.53530		
	Ni-Co	4	1.000	0.01053	2.78658		

**Note: Acceptable parameter ranges are as follows: S_0^2 (0.7–1.2), ΔE_0 (-10 to 10 eV), R-factor (<0.05), and σ^2 (>0.003).

This analysis allows for a more accurate understanding of the local atomic environment around nickel within the glass structure. The high-amplitude scattering paths contribute significantly to understanding the bonding and coordination characteristics of Ni in the doped glass sample.

After fitting the paths, the best-fit parameters obtained were R (the distance between surrounding atoms and the absorber), σ^2 (the Debye-Waller factor), S_0^2 (the scattering amplitude), ΔE_0 (the energy shift at the absorption edge), and the R-factor (a statistical measure indicating the difference between the model and experimental data) for all eight glass samples, as shown in Table 4.9. The parameters derived from the fitting are within acceptable ranges for each sample, and the spectrum lines of each glass sample closely match their best-fit lines. This indicates that the nickel ions in the glass samples have a structural environment similar to that of Ni-O bonding, with bond lengths for Ni-O (1.96 Å), Ni-Ni (2.87 Å), and Ni-Co (2.89 Å) closely aligning with those in the Li_2CoNiO_4 structure.

4.8.2 X-ray Absorption Fine Structure (EXAFS) Analysis of Cobalt-Mixed Glass Samples

Based on the crystal structure data of Li_2CoNiO_4, the program generates possible paths and then fits them to the experimental data obtained from the glass sample. Upon fitting the glass sample against the Li_2CoNiO_4 model paths, the Fourier-transformed EXAFS spectrum of the glass doped with Co_3O_4 is obtained, compared with the best-fit line, as shown in Figure 4.26, and the fitting parameters presented in Table 4.10. It was found that the parameters σ^2, S_0^2, and ΔE_0 for all samples lie outside the acceptable range. Additionally, an analysis of bond lengths in the sample shows Co–O (1.94 Å), Co–Co (2.86 Å), and Co–Ni (2.89 Å) bonds, which are relatively long within the Li_2CoNiO_4 structure. This suggests that cobalt ions in the glass sample are in a structural arrangement similar to that of the Li_2CoNiO_4 structure.

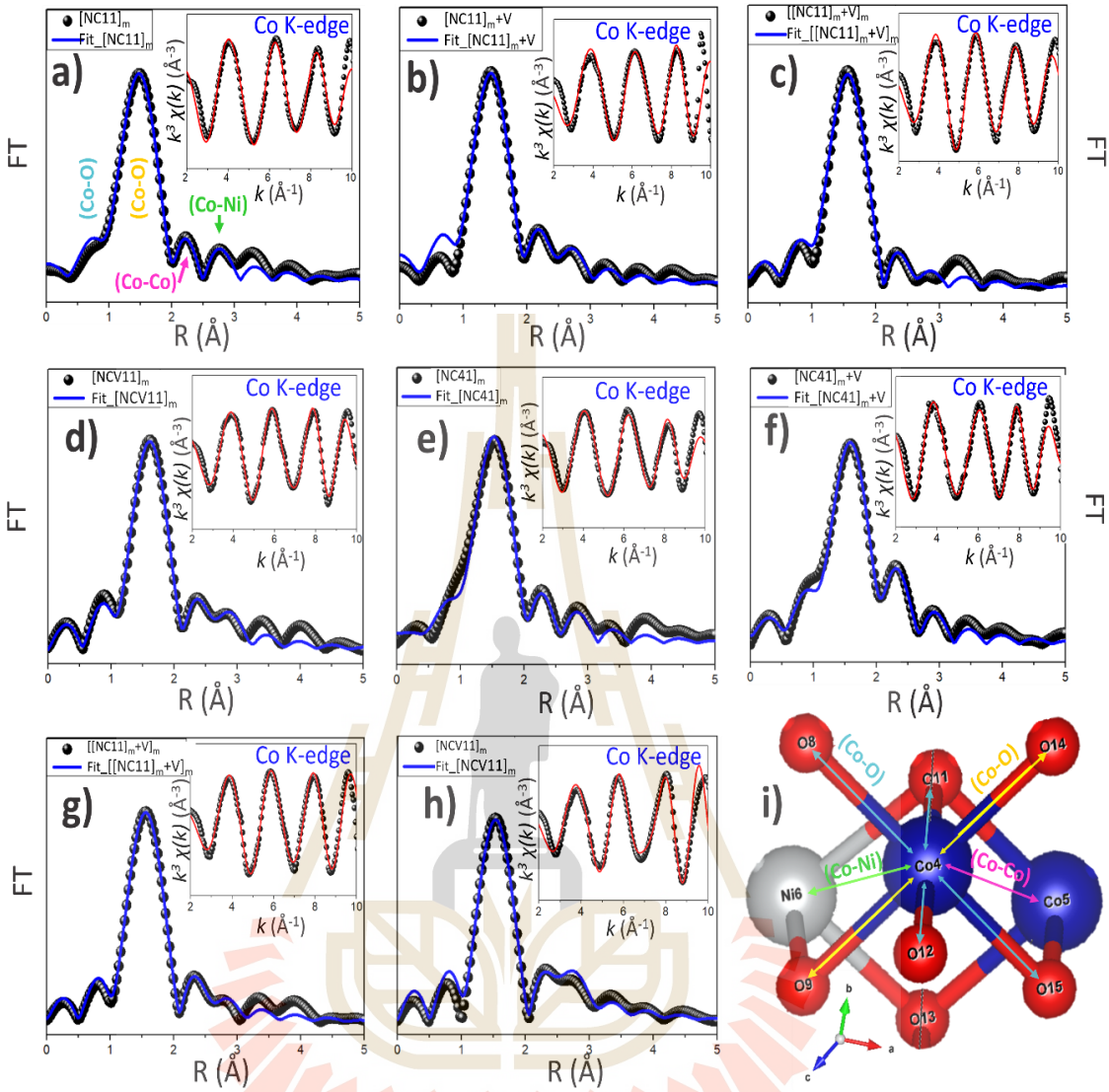

Figure 4.26 a-h) EXAFS spectra and fitting at Co K-edge of sample. i) The model used to observe the atomic distances.

The analysis suggests that Co ions in the glass matrix adopt a coordination environment similar to that of Li_2CoNiO_4, enhancing the glass's structural stability. Observed bond lengths, especially the Co–O, Co–Co, and Co–Ni distances, suggest slight distortion compared to the ideal crystal structure, likely due to the glass's amorphous nature. This bond length variation can influence the glass's electronic and magnetic properties.

Table 4.10 Presents the optimal fitting parameters for the Co_3O_4-doped glass sample compared with data from Li_2CoNiO_4.

Sample	Paths	N	S_0^2	σ^2	R (A°)	ΔE_0 (eV)	R-factor
$[NC11]_m$	Co-O	6	0.710	0.00926	1.99420	-2.605	0.008685
	Co-Co	2	0.710	0.01320	2.37512		
	Co-Ni	4	0.710	0.02278	2.60142		
$[NC11]_m$+V	Co-O	6	0.750	0.00690	1.98222	-9.263	0.0067937
	Co-Co	2	0.750	0.01088	2.36073		
	Co-Ni	4	0.750	0.02007	2.61954		
$[NC11]_m$+V]$_m$	Co-O	6	0.780	0.00502	2.05960	-3.936	0.0074191
	Co-Co	2	0.780	0.03347	2.65349		
	Co-Ni	4	0.780	0.03231	2.81446		
$[NC11+V]_m$	Co-O	6	0.842	0.00562	2.08843	0.356	0.0025018
	Co-Co	2	0.842	0.00939	2.53352		
	Co-Ni	4	0.842	0.01454	2.78645		
$[NC41]_m$	Co-O	6	0.700	0.01038	2.01583	-0.885	0.0037887
	Co-Co	2	0.700	0.01189	2.43531		
	Co-Ni	4	0.700	0.02227	2.67789		
$[NC41]_m$+V	Co-O	6	1.000	0.01223	2.08652	-0.208	0.0014706
	Co-Co	2	1.000	0.01066	2.49280		
	Co-Ni	4	1.000	0.02691	2.73803		
$[NC41]_m$+V]$_m$	Co-O	6	0.703	0.00141	2.05227	-2.921	0.0025829
	Co-Co	2	0.703	0.03397	2.45121		
	Co-Ni	4	0.703	0.02340	2.77207		
$[NC41+V]_m$	Co-O	6	0.830	0.00352	2.07041	-4.387	0.0104582
	Co-Co	2	0.830	0.00869	2.45899		
	Co-Ni	4	0.830	0.01141	2.71864		

**Note: Acceptable parameter ranges are as follows: S_0^2 (0.7–1.2), ΔE_0 (-10 to 10 eV), R-factor (<0.05), and σ^2 (>0.003).

Deviations in fitting parameters (σ^2, S_0^2, and ΔE_0) from the acceptable range reflect differences between the model and the glass's local Co environment. These discrepancies likely stem from the glass's inherent structural disorder, affecting Co coordination and bonding. Overall, the glass's similarity to Li_2CoNiO_4, combined with its unique structural properties, highlights its potential for further investigation in advanced materials research.

4.8.3 X-ray Absorption Fine Structure (EXAFS) Analysis of Vanadium-Mixed Glass Samples

The sample plate was measured for its X-ray absorption spectrum in the Extended X-ray Absorption Fine Structure (EXAFS) region at the K-absorption edge of vanadium, using photons with an energy of 5465.0 ± 0.2 eV in transmission mode. The collected data was then analyzed using the Athena software, followed by further analysis with Artemis. Additionally, the crystal data for V_2O_5 was downloaded using Model: mp-25279, which is expected to form in this glass sample group. The V_2O_5 structure is displayed in Figure 4.27.

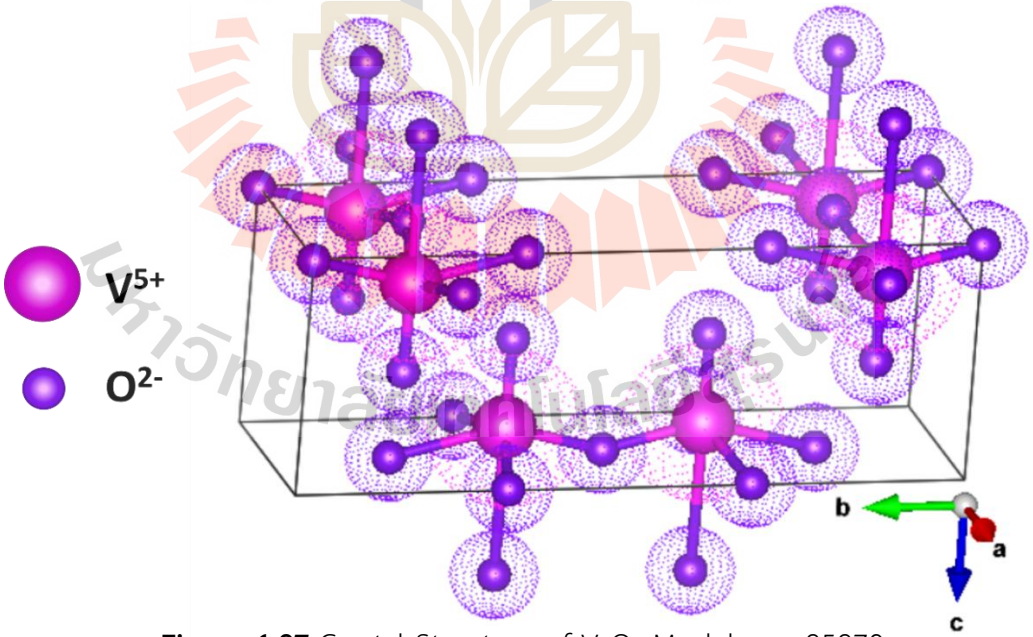

Figure 4.27 Crystal Structure of V_2O_5 Model: mp-25279.

V_2O_5 (vanadium pentoxide) with material ID mp-25279 crystallizes in an orthorhombic structure and belongs to the Pmmn space group. The structure consists

of layered sheets of vanadium (V) and oxygen (O), where vanadium atoms are coordinated in distorted octahedra formed by six oxygen atoms. These VO_6 octahedra are edge- and corner-sharing, creating a layered structure with strong in-plane V-O bonds and weaker van der Waals interactions between layers.

Table 4.11 The optimal fitting parameters for the glass sample doped with V_2O_5 were determined by comparison with reference data from V_2O_5.

Sample	Paths	N	S_0^2	σ^2	R (A°)	ΔE_0 (eV)	R-factor
$[NC11]_m$+V	V-O	1	0.700	0.00004	1.87410	-3.159	0.0241498
	V-O	4	0.700	0.02320	1.68093		
	V-O	1	0.700	0.22544	2.55790		
	V-V	1	0.700	0.01089	2.97310		
$[NC11]_m$+$V]_m$	V-O	1	0.700	0.00268	1.57724	8.313	0.0485365
	V-O	4	0.700	0.01307	1.86090		
	V-O	1	0.700	0.30218	2.65581		
	V-V	1	0.700	0.00001	3.06033		
$[NC11+V]_m$	V-O	1	1.000	0.00273	1.53027	-5.027	0.0325568
	V-O	4	1.000	0.01954	1.78401		
	V-O	1	1.000	0.00006	2.66472		
	V-V	1	1.000	0.00976	2.98644		
$[NC41]_m$+V	V-O	1	1.000	0.00056	1.52996	-6.131	0.0785836
	V-O	4	1.000	0.01852	1.77016		
	V-O	1	1.000	0.00263	2.66446		
	V-V	1	1.000	0.01369	2.99292		
$[NC41]_m$+$V]_m$	V-O	1	0.700	-0.00136	1.57430	0.417	0.0216169
	V-O	4	0.700	0.01113	1.85134		
	V-O	1	0.700	0.27030	2.67892		
	V-V	1	0.700	0.00821	3.06099		

**Note: Acceptable parameter ranges are as follows: S_0^2 (0.7–1.2), ΔE_0 (-10 to 10 eV), R-factor (<0.05), and σ^2 (>0.003).

Based on the crystal structure data, the program generates the scattering paths of atoms surrounding iron and fits them to the experimental data from the glass sample. After fitting the glass sample to the V_2O_5 model paths, the Fourier-transformed EXAFS spectrum of the V-doped glass is obtained and compared with the best-fit line, as shown in Figure 4.28, with the fitting parameters listed in Table 4.11. It was observed that the parameters σ^2, S_0^2, and ΔE_0 For all V-doped glass samples, the results fall outside the acceptable range; however, the spectrum of each glass sample shows limited similarity to the best-fit line. Further fitting attempts with models such as $Li_2V_6O_{15}$ and others were conducted, but no model provided a close match between the sample and the best-fit spectrum. This indicates that the vanadium ions in the glass sample are embedded in a highly complex structural arrangement. This suggests that the structural environment of vanadium in the glass matrix is significantly disordered. The lack of a suitable model fit implies that vanadium ions may exist in multiple coordination states or local environments. Further investigations using advanced structural analysis techniques are necessary to better understand the atomic arrangement of vanadium in the glass sample.

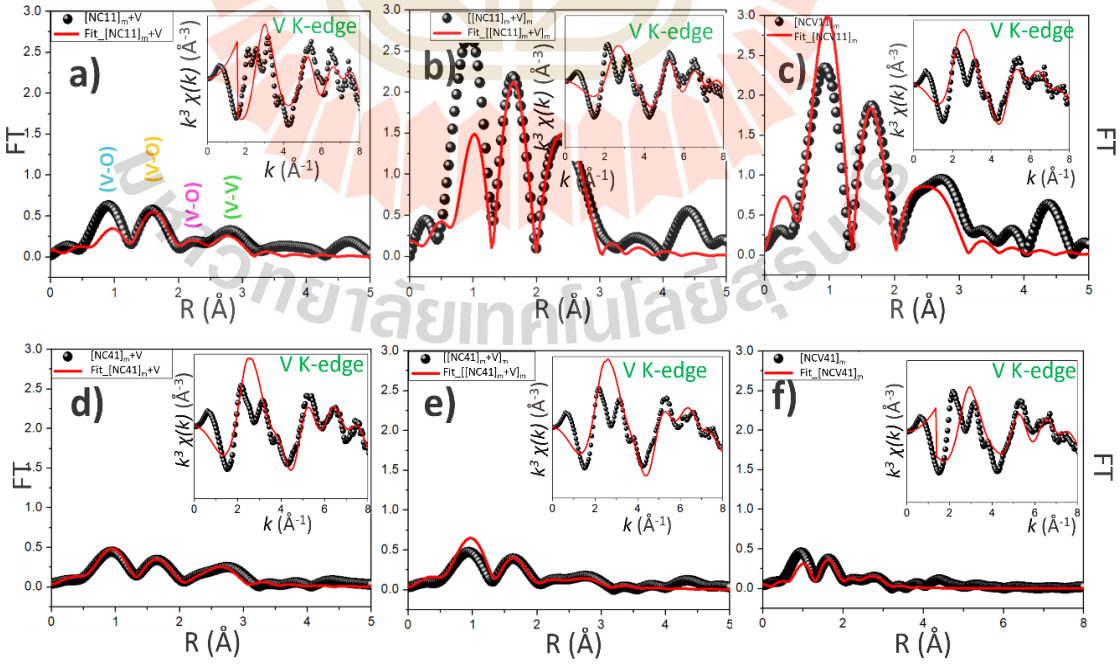

Figure 4.28 EXAFS spectra and fitting at V_2O_5 K-edge of sample.

4.9 In situ XANES analyses of V_2O_5 upon Li^+ intercalation/de-intercalation.

In situ XANES analysis of V_2O_5 during Li^+ intercalation and de-intercalation provides insights into the changes in the oxidation state and local structure of vanadium atoms in V_2O_5 while the material is actively undergoing these processes. This X-ray Absorption Near Edge Structure (XANES) spectroscopy reveals how the electronic structure and local environment around the vanadium atoms are altered during lithium insertion and removal. Understanding these changes is crucial for improving the performance and longevity of lithium-ion batteries, as it helps in optimizing the material's behavior and efficiency during battery operation.

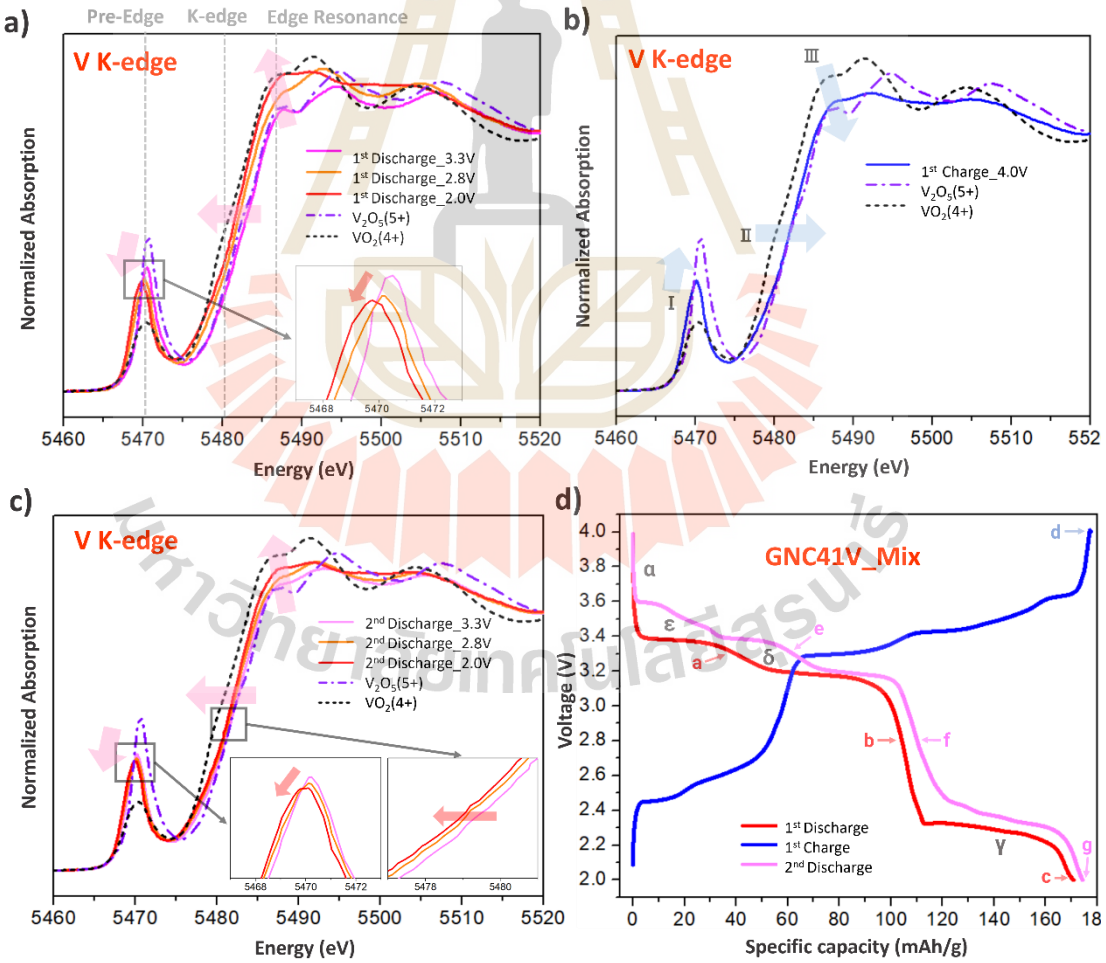

Figure 4.29 Normalized XANES Spectrum: a,c) Discharge and b) Charge; d) Voltage-Capacity Curves for Charge and Discharge Cycles.

In this study, the $[NC41]_m$+V sample was used to clearly observe the phase transitions of the V_2O_5 crystal structure. Phase changes were examined across voltage ranges of 3.3, 2.8, and 2.0 V, with a graph displaying the charge and discharge behavior of the cathode as a function of cycling shown in Figure 2.29d. For this experiment, a hole was drilled in the coin cell on the cathode side to measure X-ray Absorption Spectroscopy (XAS) in Transmission Mode (TM-XAS), with epoxy applied to prevent electrolyte leakage from the cell.

To confirm the oxidation state changes and the chemical environment around vanadium atoms within the V_2O_5 crystal, XANES analysis was conducted during the first discharge and charge cycle at 0.1 C. The Vanadium K-edge XANES spectrum can be divided into three primary components: the pre-edge, K-edge, and edge resonance (white line), labeled as Ⅰ, Ⅱ, and Ⅲ, respectively, in Figure 4.29b. The first discharge, marked as "1st Discharge," is illustrated in Figure 4.29a.

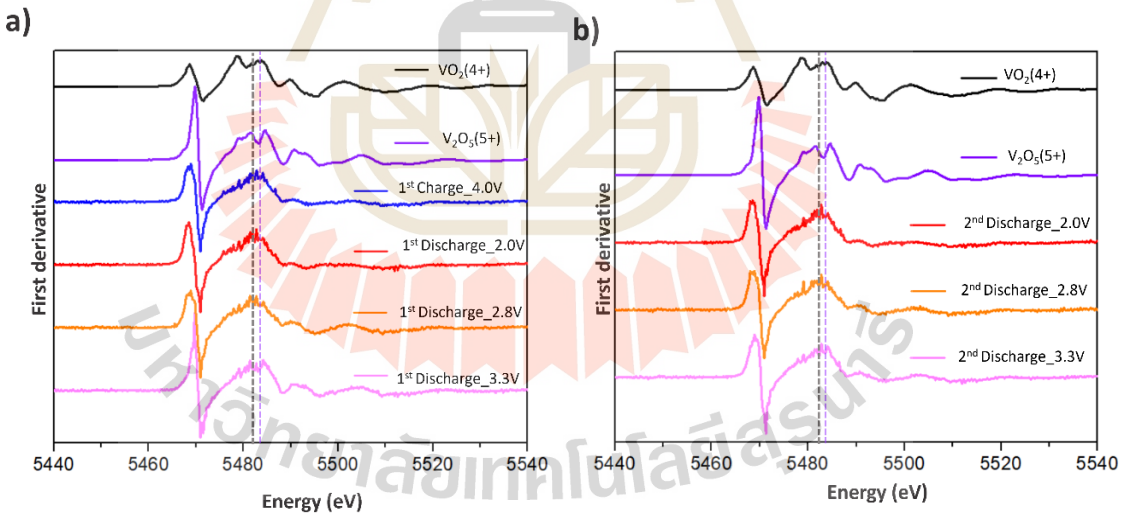

Figure 4.30 First Derivative Spectrum of the XANES Spectrum.

Changes in the pre-edge peak (Ⅰ) indicate a reduction in intensity and a shift towards lower energy levels (1s ⟶ 3d), following the red arrow on the graph. This shift signifies that Li^+ ions intercalate into the V_2O_5 structure, enhancing local symmetry around the vanadium atoms. The intensity of this pre-edge peak is sensitive to

geometric symmetry alterations, directly relating to the distortion in the VO_5 square pyramidal structure (Palanisamy, Um, Jeong, and Yoon, 2016). During the initial discharge, the K-edge (Ⅱ) progressively shifts to lower energies as more Li^+ is incorporated into the Lix V_2O_5 structure, indicating a reduction in the average oxidation state of vanadium. This corresponds with the increased amount of Li^+ intercalated into V_2O_5, where vanadium receives electrons from lithium, lowering its oxidation state.

Lastly, changes in the edge resonance (Ⅲ) reflect a decrease in intensity and a shift towards lower energy levels (1s ⟶ 4p), as shown by the red arrow in the graph. This shift is noticeable upon Li^+ insertion, resulting from the reduction in vanadium's oxidation state and indicating an increase in valence and enhanced local symmetry around the vanadium atoms in the structure.

The initial charging process, known as the 1st Charge, is shown in Figure 2.29b. The observed XANES spectrum during this charge process contrasts with the discharge process, as indicated by the blue arrows. The shift of the pre-edge peak (Ⅰ) toward higher energy (1s ⟶ 3d) with an increase in intensity indicates a shortening of the vanadyl (V=O) bond length. This shortening increases the distortion within the local structure and reduces the symmetry in the VO_5 square pyramid. Meanwhile, the shift of the K-edge (Ⅱ) to higher energy during charging signifies an increase in the oxidation state of vanadium atoms, consistent with the calculated oxidation states shown in Table 4.12. Additionally, the increase in intensity and the shift in edge resonance (Ⅲ) toward higher energy (1s ⟶ 4p) correspond with the extraction of Li+ ions and the associated increase in vanadium oxidation state, reflecting a reduction in valence and an improvement in local structural symmetry around vanadium. After the first cycle, the vanadium oxidation state returns close to its original state. In the subsequent 2nd Discharge cycle, depicted in Figure 4.29c, similar spectral changes are observed, indicating a consistent structural behavior. Following the first cycle, the distortion level of the VO_5 square pyramid decreases, and the symmetry of oxygen around vanadium increases slightly compared to the initial state. The XANES results, comparing between the pristine and fully charged states, show a partial restoration of electronic and local

structure in the composite as Li^+ ions are inserted and extracted (Palanisamy et al., 2016). This suggests that in the second charge cycle, Li ions are not completely removed from the intermediate layers, likely due to the formation of a solid-electrolyte interphase (SEI) film, leading to irreversible capacity loss (H. Wang et al., 2017).

Table 4.12 The calculated valence state of V_2O_5 ions according to the edge energy shift positions.

Steps in the Volt Range	V_2O_3: 4+ (%)	V_2O_5: 5+ (%)	V oxidation state
a) 1st Discharge at 3.3V	33.33	66.67	**4.67**
b) 1st Discharge at 2.8V	42.98	57.02	**4.57**
c) 1st Discharge at 2.0V	81.58	18.42	**4.18**
d) 1st Charge at 4.0V	73.68	26.32	**4.26**
e) 2nd Discharge at 3.3V	31.58	68.42	**4.68**
f) 2nd Discharge at 2.8V	29.82	70.18	**4.70**
g) 2nd Discharge at 2.0V	14.91	85.09	**4.85**

The energy shifts of V K-edge XANES spectra have been used to determine the valence state of the absorbing vanadium atom. According to Table 4.12, the calculated valence state from Equation X shows that the average oxidation state of V_2O_5 decreases during the initial discharge (a)–(c), as measured at 3.3, 2.8, and 2.0 V. This reduction during discharge indicates that V^{5+} ions in V_2O_5 are reduced to V^{4+}, with an overall decrease of approximately 10.49% in V^{5+} between 3.3 V and 2.0 V, consistent with previous K-edge XANES analysis. In contrast, upon charging to 4.0 V (d), the calculated valence state of 4.26, derived from XANES, suggests the presence of excess oxygen within the crystal structure, as there is a higher proportion of V^{4+} relative to V^{5+}. This means that during charging, V^{4+} ions are oxidized back to V^{5+}, then transition to V^{4+} when Li is removed (Mansour, Smith et al., 2002). During the second discharge (e)–(g),

the calculated oxidation state increases by approximately 3.63% at measurements of 3.3, 2.8, and 2.0 V, indicating that nearly all V^{4+} ions are re-oxidized to V^{5+}.

In crystalline materials, multiple coordination shells are readily identifiable, while in amorphous materials, only the first coordination shell is distinctly observed. Despite this, the overlapping first-shell distances between the two samples indicate that the amorphous material retains a tetrahedral coordination environment, albeit with significant disorder in the orientations of the Ge tetrahedra, which share corners or edges. This structural disorder plays a crucial role in determining the overall properties of the glass material (Sayers, Stern, and Lytle, 1971).

CHAPTER V
CONCLUSIONS

This thesis demonstrates that the electrochemical properties of lithium borate glass can be enhanced through the incorporation of transition metals. The amounts and ratios of these transition metals, along with different melting processes, have varying effects on the properties of the glass. In this research, the influence of transition metal ratios and melting procedures has been investigated using a diverse array of methodologies.

The production of transition metal-doped lithium borate glass samples was successfully achieved using a melt-quenching approach. Initially, the samples exhibited a shiny and brittle appearance, characterized by a distinct black hue, indicative of transition metals, specifically nickel and cobalt oxides. The fundamental objective of this investigation was to assess the properties of the lithium borate glass, which was accomplished through X-ray diffraction (XRD) analysis. The XRD results demonstrated that both the pure LBO glass base and the NiO/Co_2O_3-doped glass base maintained an amorphous structure ($[NC11]_m$ and $[NC41]_m$). However, the addition of V_2O_5 resulted in it resulted in a higher capacitance value due to the formation of a glass-ceramic structure of $Li_6B_4O_9$. In this system, the incorporation of V_2O_5 facilitates the reaction between boron and vanadium, leading to their fusion into a glass matrix, while the amount of Li_2O remains constant. In contrast, B_2O_3 content decreases as it reacts with vanadium, affecting the ratio of Li_2O to B_2O_3. Moreover, the substantial addition of vanadium (75%) slows down the cooling process, resulting in the formation of $Li_6B_4O_9$ with a hexaborate structure in samples such as $[NC11]_m+V]_m$, $[NC41]_m+V]_m$, $[NC11+V]_m$, and $[NC41+V]_m$. The study of the $Li_6B_4O_9$ peak revealed that the $[[NC]_m+V]_m$ sample exhibited a higher peak intensity compared to the $[NCV]_m$ sample, indicating that the latter possesses a more amorphous nature. The improved crystallinity observed in the

$[[NC]_m + V]_m$ sample can be attributed to the three melting cycles it underwent, which facilitated more thorough crystallization compared to samples subjected to only two cycles. Consequently, the crystalline structure in the $[[NC]_m + V]_m$ sample became more defined and complete following the additional melting process.

Performance tests on batteries prepared via the melt quenching process reveal that the $[NC41+V]_m$ sample displays excellent energy storage capabilities, with an average capacity of 111.42 mAh/g and an energy density of 306.26 mWh/g—values significantly higher than other samples. Notably, the capacity retention of $[NC41+V]_m$ reaches an impressive 80.69% after 100 cycles, highlighting its stability and resistance to degradation. Additionally, samples $[NC11]_m+V$ and $[NC41]_m+V$, incorporating 75% V_2O_5, achieve high capacity and energy density values, with $[NC41]_m+V$ recording a peak capacity of 140.13 mAh/g and an energy density of 410.93 mWh/g. This indicates exceptional energy storage and release efficiency; however, V_2O_5-based batteries often experience capacity retention declines due to structural vulnerability and potential degradation during prolonged usage. Still, combining V_2O_5 with GNC significantly enhances the battery's capacity.

This study also investigates the chemical properties of the samples, beginning with EIS measurements, followed by three CV cycles, and concluding with a final EIS measurement. Analyses from Cyclic Voltammetry (CV) and Electrochemical Impedance Spectroscopy (EIS) reveal that incorporating LBO in the sample materials greatly reduces internal resistance, indicating improved charge transfer and structural reinforcement. Specifically, $[NC11]_m+V$ and $[NC41]_m+V$ initially exhibit high internal resistance that decreases markedly after three CV cycles, signifying improved ionic conductivity. For materials such as $[NC11]_m+V]_m$, $[NC41]_m+V]_m$, $[NC11+V]_m$, and $[NC41+V]_m$, internal resistance remains largely unchanged throughout EIS testing. CV measurements further highlight V_2O_5 crystal phase transitions during the redox process, signifying efficient Li^+ acceptance and transfer. $[NC11]_m+V$ and $[NC41]_m+V$ samples demonstrate distinct redox peaks consistent with V_2O_5 phase changes. However, melting V_2O_5 into the glass matrix lowers current density, effectively prolonging battery life. CV graphs from cycles 1 to 3 for $[NC11]_m+V]_m$, $[NC41]_m+V]_m$, $[NC11+V]_m$, and

$[NC41+V]_m$ maintain steady resistance, indicating material durability, electrode stability, and consistent reversibility, aligning with long-term capacity retention.

Electron transfer in the context of oxidation-reduction (redox) reactions is a fundamental component of electrochemical phenomena. Understanding the charge transfer effects associated with incorporating transition metals into glass requires detailed knowledge of their oxidation states. To investigate these oxidation states, X-ray Absorption Near Edge Structure (XANES) analysis was employed. Nickel within the glass exhibits both Ni^{2+} and Ni^{3+} oxidation states, with a higher concentration of Ni^{2+}. For cobalt, oxidation states Co^{2+} and $Co^{2+,3+}$ are present, with Co^{3+} being more dominant. Vanadium exists in both V^{4+} and V^{5+} states, with a higher presence of V^{5+}. Adjustments in the Ni and Co ratios lead to slight shifts in the oxidation states of these transition metals within the glass samples, potentially impacting their electrochemical properties.

The interplay of Li^+ and Ni^{2+} is notable, as higher Ni^{2+} levels can limit the specific capacity in nickel-rich NC materials. For instance, if Ni^{2+} substitutes Li^+ ions, lower-valence nickel ions can migrate from the transition metal layer into the lithium layer, filling lithium vacancies and impeding Li^+ diffusion, which constrains battery charging capacity. However, restricting Ni^{2+} transport into the Li layer, even with minimal cobalt (Co^{3+}), helps maintain structural integrity. Additionally, the presence of Co enhances conductivity and enables the material to perform effectively work at high rates.

The study of X-ray absorption spectra in the EXAFS region of glass samples doped with NiO, Co_3O_4, and V_2O_5 aimed to observe local atomic changes of these elements. Glass samples analyzed using Athena and Artemis software effectively identified the scattering paths of atoms surrounding the absorber atom, allowing efficient fitting with experimental data. Key parameters such as R (interatomic distance), $\boldsymbol{\sigma}^2$ (Debye-Waller factor), s_0^2 (scattering amplitude), ΔE_0 (edge energy shift), and R-factor (model-experiment fit difference) for NiO- and Co_3O_4-doped glass samples were within acceptable ranges across all cases. However, in V_2O_5-doped glass samples, while some parameters fell without acceptable limits, the fit with both the V_2O_5 model and alternative models did not align closely with the best-fit line. This suggests that

vanadium in the glass samples may exhibit a complex structure or unique bonding with other components not accurately represented by the existing models.

This study employed XANES to analyze the changes in oxidation states and the local structure of vanadium atoms in V_2O_5 during the intercalation and deintercalation of lithium ions during discharge and charge cycles. During the first discharge at 0.1 C, the intensity of the pre-edge peak decreased and shifted to lower energy, indicating a reduction in distortion within the VO_5 square pyramid structure. The K-edge shift to lower energy is aligned with reducing the vanadium oxidation state. During the charging process, the energy and intensity of the pre-edge peak increased, signaling greater distortion and an increase in the oxidation state. Following the first cycle, the VO_5 structure showed slightly reduced distortion and increased oxygen symmetry around vanadium compared to its initial state. XANES results revealed structural reversibility during Li^+ intercalation and deintercalation. However, the observed irreversible capacity loss was attributed to forming the of solid electrolyte interphase (SEI) film.

In this study, XANES analysis was conducted on V_2O_5 to observe changes in the oxidation state of vanadium atoms during Li^+ insertion and extraction, with particular attention to the $[NC41]_m$+V sample, which exhibited significant phase changes in V_2O_5. The first discharge cycle revealed alterations in the XANES spectrum, including a decrease in the pre-edge peak intensity and energy, indicating an increase in local symmetry around vanadium atoms as Li^+ infiltrated V_2O_5. Additionally, a shift of the K-edge to lower energy suggested the reduction of vanadium from V^{5+} to V^{4+}. Conversely, during the initial charge cycle, the spectrum reversed, reflecting an increase in oxidation state as Li^+ ions were removed, thus restoring local structural symmetry. In the second discharge, the XANES data showed similar trends but with reduced distortion in the VO_5 square pyramid and greater symmetry in the local vanadium environment compared to the first cycle. This indicates partial irreversibility due to incomplete SEI layer formation, as residual Li^+ affects later performance. Calculated oxidation states further support these findings, showing a 10.49% reduction during the first discharge and partial re-oxidation during charging. EXAFS analysis of the disordered glass materials underscores the importance of appropriate sample preparation and

analysis techniques to accurately understand the structural and electronic properties of these materials.

The conclusions from the establishment of two research objectives are as follows:

5.1 The ratio of Ni:Co (4:1) resulted in better specific capacity and improved stability.

5.2 Samples with $Li_6B_4O_9$ crystals showed high stability after multiple cycles. Particularly, $[NCV41]_m$ demonstrated outstanding performance with an average capacity of 111.42 mAh/g, energy density of 306.26 mWh/g, and 80.69% capacity retention after 100 cycles, indicating excellent battery durability.

REFERENCES

REFERENCES

Abdelkareem, M. A., Elsaid, K., Wilberforce, T., Kamil, M., Sayed, E. T., and Olabi, A. (2021). Environmental aspects of fuel cells: A review. *Science of The Total Environment, 752*, 141803.

Afyon, S., Krumeich, F., Mensing, C., Borgschulte, A., and Nesper, R. (2014). New high capacity cathode materials for rechargeable Li-ion batteries: vanadate-borate glasses. *Scientific reports, 4*(1), 7113.

Armer, C. F., Lübke, M., Johnson, I., McColl, K., Cora, F., Yeoh, J. S., . . . Lowe, A. (2018). Enhanced electrochemical performance of electrospun V_2O_5 fibres doped with redox-inactive metals. *Journal of Solid State Electrochemistry, 22*, 3703-3716.

Borisov, S. V., and Podberezskaya, N. (2012). X-ray diffraction analysis: A brief history and achievements of the first century. *Journal of Structural Chemistry, 53*, 1-3.

Bragg, W., and Thomson, J. (1914). *Mr Bragg, Diffraction of Short Electromagnetic Waves, etc.* 43. Paper presented at the Proceedings of the Cambridge Philosophical Society: Mathematical and physical sciences.

Cahill, J. T., and Graeve, O. A. (2019). Hexaborides: a review of structure, synthesis and processing. *Journal of Materials Research and Technology, 8*(6), 6321-6335.

Cheah, Y. L., Aravindan, V., and Madhavi, S. (2013). Synthesis and enhanced lithium storage properties of electrospun V_2O_5 nanofibers in full-cell assembly with a spinel $Li_4Ti_5O_{12}$ anode. *ACS Applied Materials and Interfaces, 5*(8), 3475-3480.

Choudhary, Y. S., Jothi, L., and Nageswaran, G. (2017). Electrochemical characterization. In *Spectroscopic Methods for Nanomaterials Characterization* (pp. 19-54): Elsevier.

Christen, T., and Carlen, M. W. (2000). Theory of Ragone plots. *Journal of power sources, 91*(2), 210-216.

Daengsakul, S., Kidkhunthod, P., Soisang, O., Kuenoon, T., Bootchanont, A., and Maensiri, S. (2015). The effect of Gd doping in La1− x− yGdxSryMnO$_3$ compound

on nanocrystalline structure by X-ray Absorption Spectroscopy (XAS) technique. *Microelectronic Engineering, 146*, 38-42.

Epp, J. (2016). X-ray diffraction (XRD) techniques for materials characterization. In *Materials characterization using nondestructive evaluation (NDE) methods* (pp. 81-124): Elsevier.

Fracchia, M., Ghigna, P., Vertova, A., Rondinini, S., and Minguzzi, A. (2018). Time-resolved X-ray absorption spectroscopy in (photo) electrochemistry. *Surfaces, 1*(1), 138-150.

González, A., Goikolea, E., Barrena, J. A., and Mysyk, R. (2016). Review on supercapacitors: Technologies and materials. *Renewable and Sustainable Energy Reviews, 58*, 1189-1206.

Hannan, M., Hoque, M. M., Mohamed, A., and Ayob, A. (2017). Review of energy storage systems for electric vehicle applications: Issues and challenges. *Renewable and Sustainable Energy Reviews, 69*, 771-789.

He, H., Sun, D., Tang, Y., Wang, H., and Shao, M. (2019). Understanding and improving the initial Coulombic efficiency of high-capacity anode materials for practical sodium ion batteries. *Energy Storage Materials, 23*, 233-251.

Kajihara, K. (2013). Recent advances in sol–gel synthesis of monolithic silica and silica-based glasses. *Journal of Asian Ceramic Societies, 1*(2), 121-133. doi:10.1016/j.jascer.2013.04.002

Karmakar, B. (2017). *Functional glasses and glass-ceramics: processing, properties and applications*: Butterworth-Heinemann.

Kayyar, A., Huang, J., Samiee, M., and Luo, J. (2012). Construction and testing of coin cells of lithium ion batteries. *JoVE (Journal of Visualized Experiments)*(66), e4104.

Khajonrit, J., Montreeuppathum, A., Kidkhunthod, P., Chanlek, N., Poo-arporn, Y., Pinitsoontorn, S., and Maensiri, S. (2018). New transparent materials for applications as supercapacitors: manganese-lithium-borate glasses. *Journal of Alloys and Compounds, 763*, 199-208.

Kim, T., Choi, W., Shin, H.-C., Choi, J.-Y., Kim, J. M., Park, M.-S., and Yoon, W.-S. (2020). Applications of voltammetry in lithium ion battery research. *Journal of Electrochemical Science and Technology, 11*(1), 14-25.

Kitaigorodsky, A. (2012). *Molecular crystals and molecules* (Vol. *29*): Elsevier.

Kubota, K., Dahbi, M., Hosaka, T., Kumakura, S., and Komaba, S. (2018). Towards K-ion and Na-ion batteries as "beyond Li-ion". *The chemical record, 18*(4), 459-479.

Li, C., Yuan, W., Li, C., Wang, H., Wang, L., Liu, Y., and Zhang, N. (2021). Boosting $Li_3V_2(PO_4)_3$ cathode stability using a concentrated aqueous electrolyte for high-voltage zinc batteries. *Chemical Communications, 57*(35), 4319-4322.

Liu, S., Tong, Z., Zhao, J., Liu, X., Ma, X., Chi, C., . . . Li, Y. (2016). Rational selection of amorphous or crystalline V_2O_5 cathode for sodium-ion batteries. *Physical Chemistry Chemical Physics, 18*(36), 25645-25654.

Mansour, A., Smith, P., Baker, W., Balasubramanian, M., and McBreen, J. (2002). In situ XAS investigation of the oxidation state and local structure of vanadium in discharged and charged V_2O_5 aerogel cathodes. *Electrochimica Acta, 47*(19), 3151-3161.

McCurdy, R. J. (1999). Successful implementation methods of atmospheric CVD on a glass manufacturing line. *Thin Solid Films, 351*(1-2), 66-72.

Nunes, C., Mahendrasingam, A., and Suryanarayanan, R. (2005). Quantification of crystallinity in substantially amorphous materials by synchrotron X-ray powder diffractometry. *Pharmaceutical research, 22*, 1942-1953.

Palanisamy, K., Um, J. H., Jeong, M., and Yoon, W.-S. (2016). Porous V_2O_5/RGO/CNT hierarchical architecture as a cathode material: Emphasis on the contribution of surface lithium storage. *Scientific reports, 6*(1), 31275.

Potyrailo, R. A., and Maier, W. F. (2006). *Combinatorial and high-throughput discovery and optimization of catalysts and materials*: CRC Press.

Ravel, B., and Newville, M. (2005). ATHENA, ARTEMIS, HEPHAESTUS: data analysis for X-ray absorption spectroscopy using IFEFFIT. *Journal of synchrotron radiation, 12*(4), 537-541.

Rousse, G., Baptiste, B., and Lelong, G. (2014). Crystal structures of $Li_6B_4O_9$ and $Li_3B_{11}O_{18}$ and application of the dimensional reduction formalism to lithium borates. *Inorganic Chemistry, 53*(12), 6034-6041.

Saetova, N., Raskovalov, A., Antonov, B., Denisova, T., and Zhuravlev, N. (2020). Structural features of $Li_2O–V_2O_5–B_2O_3$ glasses: Experiment and molecular dynamics simulation. *Journal of Non-Crystalline Solids, 545*, 120253.

Saetova, N., Raskovalov, A., Antonov, B., Yaroslavtseva, T., Reznitskikh, O., Zabolotskaya, E., . . . Telyatnikova, A. (2018). Conductivity and spectroscopic studies of $Li_2OV_2O_5$-B_2O_3 glasses. *Ionics, 24*, 1929-1938.

Sagadevan, S., Marlinda, A., Chowdhury, Z. Z., Wahab, Y. B. A., Hamizi, N. A., Shahid, M., . . . Johan, M. R. (2021). Fundamental electrochemical energy storage systems. In *Advances in Supercapacitor and Supercapattery* (pp. 27-43): Elsevier.

Sayers, D. E., Stern, E. A., and Lytle, F. W. (1971). New technique for investigating noncrystalline structures: Fourier analysis of the extended x-ray—absorption fine structure. *Physical review letters, 27*(18), 1204.

Schwartz, L. H., and Cohen, J. B. (2013). *Diffraction from materials*: Springer Science and Business Media.

Sharma, P., and Bhatti, T. (2010). A review on electrochemical double-layer capacitors. *Energy conversion and management, 51*(12), 2901-2912.

Sheldrick, G. (1998). SHELX-97, Release 97-2. In: Univ. Göttingen, Germany.

Siriroj, S., Padchasri, J., Montreeuppathum, A., Lomon, J., Chanlek, N., Poo-arporn, Y., . . . Kidkhunthod, P. (2023). New glass cathode materials for Li-ion battery: Ni-Co doping in Li-BO based glass. *Materials Science for Energy Technologies*.

Siriroj, S., Padchasri, J., Montreeuppathum, A., Lomon, J., Chanlek, N., Poo-Arporn, Y., . . . Kidkhunthod, P. (2022). Enhancement of V_2O_5 Li-ion cathode stability by Ni/Co doped Li-borate-based glass. *RSC advances, 12*(40), 26111-26115.

Siriroj, S., Padchasri, J., Montreeuppathum, A., Sonsupap, S., Maensiri, S., Kheawhom, S., and Kidkhunthod, P. (2024). Glass-Sulfur Composite Cathodes: A New Strategy for Improving the Performance of Lithium-Sulfur Batteries. *Materials Research Bulletin*, 112919.

Spieß, L., Behnken, H., Genzel, C., Schwarzer, R., and Teichert, G. (2009). *Moderne röntgenbeugung* (Vol. *2*): Springer.

Stan, G. E., Montazerian, M., Shearer, A., Stuart, B. W., Baino, F., Mauro, J. C., and Ferreira, J. M. (2023). Critical advances in the field of magnetron sputtered bioactive glass thin-films: An analytical review. *Applied Surface Science*, 158760.

Swiderska-Mocek, A., and Naparstek, D. (2016). Physical and electrochemical properties of lithium bis (oxalate) borate—organic mixed electrolytes in Li-ion batteries. *Electrochimica Acta, 204*, 69-77.

Varshneya, A. K. (2013). *Fundamentals of inorganic glasses*: Elsevier.

Wang, H., Isobe, J., Matsumura, D., and Yoshikawa, H. (2018). In situ X-ray absorption fine structure studies of amorphous and crystalline polyoxovanadate cluster cathodes for lithium batteries. *Journal of Solid State Electrochemistry, 22*, 2067-2071.

Wang, H., Isobe, J., Shimizu, T., Matsumura, D., Ina, T., and Yoshikawa, H. (2017). Preparation of γ-LiV_2O_5 from polyoxovanadate cluster $Li_7[V_{15}O_{36}(CO_3)]$ as a high-performance cathode material and its reaction mechanism revealed by operando XAFS. *Journal of power sources, 360*, 150-156.

Wang, P.-P., Chen, J., Xu, C.-Y., Wang, Y.-Q., and Zhen, L. (2017). Vertical aligned V_2O_5 nanoneedle arrays grown on Ti substrate as binder-free cathode for lithium-ion batteries. *Ionics, 23*, 2961-2967.

Weber, A. Z., Mench, M. M., Meyers, J. P., Ross, P. N., Gostick, J. T., and Liu, Q. (2011). Redox flow batteries: a review. *Journal of applied electrochemistry, 41*, 1137-1164.

Wei, Z., Wang, D., Yang, X., Wang, C., Chen, G., and Du, F. (2018). From crystalline to amorphous: an effective avenue to engineer high-performance electrode materials for sodium-ion batteries. *Advanced Materials Interfaces, 5*(19), 1800639.

Xiao, Y., Miara, L. J., Wang, Y., and Ceder, G. (2019). Computational screening of cathode coatings for solid-state batteries. *Joule, 3*(5), 1252-1275.

Yamada, A., Iwane, N., Harada, Y., Nishimura, S. i., Koyama, Y., and Tanaka, I. (2010). Lithium iron borates as high-capacity battery electrodes. *Advanced Materials, 22*(32), 3583-3587.

Yang, S.-H., Xue, H., and Guo, S.-P. (2021). Borates as promising electrode materials for rechargeable batteries. *Coordination Chemistry Reviews, 427*, 213551.

Yano, J., and Yachandra, V. K. (2009). X-ray absorption spectroscopy. *Photosynthesis research, 102*, 241-254.

Zeng, X., Kuang, Q., Fan, Q., Dong, Y., Zhao, Y., Chen, S., and Liu, S. (2020). Synthesis, structure, and electrochemical performance of V_3BO_6 nanocomposite: A new vanadium borate as high-rate anode for Li-ion batteries. *Electrochimica Acta, 335*, 135661.

Zhao, E.-L., Zhao, S.-X., Wu, X., Li, J.-W., Yu, L.-Q., Nan, C.-W., and Cao, G. (2019). Electrochemical performance of Li_2O-V_2O_5-SiO_2-B_2O_3 glass as cathode material for lithium ion batteries. *Journal of Materiomics, 5*(4), 663-669.

Zhou, D., Pang, L.-X., Wang, D.-W., Qi, Z.-M., and Reaney, I. M. (2018). High quality factor, ultralow sintering temperature $Li_6B_4O_9$ microwave dielectric ceramics with ultralow density for antenna substrates. *ACS sustainable chemistry and engineering, 6*(8), 11138-11143.

CURRICULUM VITAE

Name Puttamawan Juntree

Place of Birth Si Sa Ket

Education

2022 B.Sc. in Physics (First Class Honors), Suranaree University of Technology, Institute of Science, Thailand

Publication Juntree, P., Siriroj, S., Padchasri, J., Songsiriritthigul, P., & Kidkhunthod, P. (2025). Development of Li-ion Batteries Cathode Materials by Using Nickel and Cobalt mixed Li-Borate Base Glass composite with V_2O_5 via Melt Quenching Method. *Journal of Alloys and Compounds*, 178961.

Grants and Fellowships

2022 – 2024 Kittibundit Scholarship of Suranaree University of Technology (SUT)

Position and Place of Work

2013 – 2024 The research assistantship at Beamline 1.3W: Small/Wide Angle X-ray Scattering at the Synchrotron Light Research Institute, From October 2, 2023, to October 2, 2024, under the supervision of Nuntaporn Kamonsutthipaijit